19TH INTERNATIONAL CONFERENCE on Communications, Electromagnetics and Medical Applications (CEMA'25)

Athens, Greece
20th - 21st October, 2025

Organized by:
Faculty of Telecommunications of TU-Sofia, Bulgaria

NATIONAL TECHNICAL UNIVERSITY OF ATHENS, GREECE

SCHOOL OF ELECTRICAL AND COMPUTER ENGINEERING

PROCEEDINGS

OF 19TH INTERNATIONAL CONFERENCE ON COMMUNICATIONS, ELECTROMAGNETICS AND MEDICAL APPLICATIONS (CEMA'25)

Organized by:

NATIONAL TECHNICAL UNIVERSITY OF ATHENS, GREECE,
SCHOOL OF ELECTRICAL AND COMPUTER ENGINEERING

FACULTY OF TELECOMMUNICATIONS
TECHNICAL UNIVERSITY OF SOFIA, BULGARIA

NATIONAL TECHNICAL
UNIVERSITY OF ATHENS,
GREECE

SCHOOL OF ELECTRICAL
AND COMPUTER
ENGINEERING

Athens, Greece
20th – 21st October, 2025

KING 2001, Sofia

Edited by Prof. Dr. Eng. **Dimiter Tz. Dimitrov**

All rights reserved. This book, or parts there of, may not be reproduced in any form or by any means, electronic or mechanical, including photocoying or any information starage and the retrieval system now known or to be invented without written permission from the Publisher.

ISSN: 1314-2100

SCOPUS Indexing
http://suggestor.step.scopus.com/progressTracker, ID: 6B4F77263D276412.

Printed in Bulgaria
KING 2001, Sofia

P. Frangos

D. Dimitrov

K. Dimitrov

Dear Colleagues,

It is our privilege to thank all of you for your contributions submitted at 18th regular International Conference on 'Communication, Electromagnetic and Medical Applications' CEMA'25. This is a conference which should help future collaboration in the area of engineering, especially in the area of communication technologies and medical applications. This is an important scientific event not only in Balkan region, but in Europe, also. The International Conference on Communication, Electromagnetism and Medical Applications CEMA'25 is dedicated to all essential aspects of the development of global information and communication technologies, and their impact in medicine, as well. The objective of Conference is to bring together lecturers, researchers and practitioners from different countries, working on the field of communication, electromagnetism, medical applications and computer simulation of electromagnetic field, in order to exchange information and bring new contribution to this important field of engineering design and application in medicine. The Conference will bring you the latest ideas and development of the tools for the above mentioned scientific areas directly from their inventors. The objective of the Conference is also to bring together the academic community, researchers and practitioners working in the field of Communication, Electromagnetic and Medical Applications, not only from all over Europe, but also from America and Asia, in order to exchange information and present new scientific and technical contributions.

Many well known scientists took part in conference preparation as members of International Scientific Committee or/and as reviewers of submitted papers. We would like to thank all of them for their efforts, for their suggestions and advices.

On behalf of the International Scientific Committee, we would like to wish you successful presentations of your papers, successful discussions and new collaborations for your future scientific investigations.

Engineering and medicine should provide high level of living for all people.

P. Frangos
Conference Chairman

D. Dimitrov
Conference Vice Chairman

K. Dimitrov
Conference Vice Chairman

INTERNATIONAL SCIENTIFIC COMMITTEE

Chairman:

P. FRANGOS, National Technical University of Athens, Greece

Vice Chairmen:

D. TZ. DIMITROV, Technical University of Sofia, Bulgaria
K. L. DIMITROV, Technical University of Sofia, Bulgaria

Members

N. AMPILOVA,	University of Petersburg, Russia
T. AVOYAGI,	Tokyo Institute of Technology, Japan
A. BEKJARSKY,	Technical University of Sofia, Bulgaria
E. BOEMO,	University Authonoma, Barcelona, Spain
R. BRUZGIENE,	Kaunas University of Technology, Lithuania
N. DIB,	Jordan University of Science and Technology, Aman, Jordan
V. DUMBRAVA,	Kaunas University of Technology, Litvania
N. ESCUDEIRO,	ISEP, Porto, Portugal
E. GAGO-RIBAS,	University of Oviedo, Spain
V. GEORGIEVA,	Technical University of Sofia, Bulgaria
G. GOUSSETIS,	Heriot - Watt University, United Kingdom
S. V.HOEYE,	University of Oviedo, Spain
I. ILIEV,	Technical University of Sofia, Bulgaria
F. KLETT,	Franhofer Institute, Ilmenau, Germany
G. KLIROS,	Hellenic Air-Force Academy, Athens, Greece
V. KUKENSKA,	Technical University of Gabrovo, Bulgaria
L. LUBIH,	Technical University of Sofia, Bulgaria
G. MALLET,	University "Sophia Antipolis", Nice, France
G. MATSOPOULOS,	National Technical University of Athens, Greece
M. MARTINS,	Academia Militar da Amadora, DCEE, Portugal
M.– J. MORALES-GONZALES,	University of Valladolid, Spain
L. NARBUTAITE,	Kaunas University of Technology, Lithuania
K. NIKITA,	National Technical University of Athens, Greece
M. NIKOLOVA,	Nikola Vaptsarov Naval Academy, Bulgaria
A. PANAGOPOULOS,	National Technical University of Athens, Greece
J. PETROVSKA,	Medical University of Sofia, Bulgaria
H. ROTH,	University of Siegen, Germany
S. SAUTBEKOV,	Euroasian University, Astana, Kazakhstan
A. SAVOV,	Medical University of Sofia, Bulgaria
S. SAVOV,	Technical University of Varna, Bulgaria
H.-P. SCHADE,	Technical University of Ilmenau, Germany
I. SOLOVIEV,	University of St. Petersburg, Russia
L. SONG,	Technical University of Harbin, China
G. STAMATAKOS,	National Technical University of Athens, Greece
A. USHEVA,	University of Boston, USA
R. VERDONE,	University of Bologna, Italy

REVIEWERS

BALZANO, Q.	University of Maryland, USA
BEHARI, J.	Jawaharlal Nehru University ,New Delhi, India
BOEMO, E.	Technical University of Madrid, Spain
DIMITROV, D.	Technical University of Sofia, Bulgaria
DONTSCHEWA, M.	University of Applied Sciences, Dorbirn, Austria
GOUSSETIS, G.	Heriot - Watt University, United Kingdom
MALLET, G.	University “Sophia Antipolis”, Nice, France
PETROVSKA, J.	Medical University of Sofia, Bulgaria
PRATO, F.	University of Western Ontario, Canada
ROTH, H.	University of Siegen, Germany
SAVOV, A.	Medical University of Sofia, Bulgaria
SCHADE, H-P.	Technical University of Ilmenau, Germany
SONG, L.	Technical University of Harbin, China
USHEVA, A.	University of Boston, USA

REGISTRATION

October, 20th, 2025, 10h – 16h

The conference registration desk will be in the
National Technical University of Athens

CONFERENCE PROGRAM

October, 20th, 2025, Monday

OPENING CEREMONY

11h – 11h 30min
The Opening Ceremony will be on-line

SCIENTIFIC PROGRAM

FIRST SESSION

11h 30min – 13h

CHAIRMAN: ***Prof. P. Frangos,*** *School of Electrical and Computing Engineering, National Technical University of Athens, Greece*

---

1. **THE INFLUENCE OF DIAGNOSIS AND ETHNIC BACKGROUND ON THE CHOICE OF CARE ENVIRONMENT FOR CHILDREN WITH NEURODEVELOPMENTAL DISORDERS**

   Kalina Georgieva – Bozhkova*, Department of Material Science and Prosthetic Dental Medicine, Faculty of Dental Medicine, Medical University – Varna, Bulgaria*

   Anna Nenova – Nogalcheva*, Department of Oral Surgery, Faculty of Dental Medicine, Medical University – Varna, Bulgaria*

   Mariya Nikolova*, Department of Information Technology, Faculty of Engineering, Nikola Vaptsarov Naval Academy, Bulgaria*

   Emiliya Koleva*, Department of Electronics, Faculty of Engineering, Nikola Vaptsarov Naval Academy, Bulgaria*

   Desislava Konstantinova*, Department of Material Science and Prosthetic Dental Medicine, Faculty of Dental Medicine, Medical University – Varna, Bulgaria*

2. **THE INFLUENCE OF NEURODEVELOPMENTAL DISORDERS ON CRANIOFACIAL SYMMETRY IN PEDIATRIC POPULATIONS**

   Kalina Georgieva – Bozhkova*, Department of Material Science and Prosthetic Dental Medicine, Faculty of Dental Medicine, Medical University – Varna, Bulgaria*

   Emiliya Koleva*, Department of Electronics, Faculty of Engineering, Nikola Vaptsarov Naval Academy, Bulgaria*

   Mariya Nikolova*, Department of Information Technology, Faculty of Engineering, Nikola Vaptsarov Naval Academy, Bulgaria*

   Anna Nenova – Nogalcheva*, Department of Oral Surgery, Faculty of Dental Medicine, Medical University – Varna, Bulgaria*

   Desislava Konstantinova*, Department of Material Science and Prosthetic Dental Medicine, Faculty of Dental Medicine, Medical University – Varna, Bulgaria*

3. **ON THE ANALYSIS OF THYROID GLAND ULTRASONIC IMAGES BY THE METHODS OF HARALIC AND LOCAL DENSITY FUNCTION**

   ***V. Lyamin**, **I. Soloviev, N. Ampilova** Saint-Petersburg State University, Petersburg, Russia*

4. **SIMULATION OF A LORA-BASED WEARABLE SYSTEM FOR MARITIME EMERGENCY TRACKING USING MATLAB**

   ***Nadezhda Vladimirova**, Department of Information Technologies,*
   Nikola Vaptsarov Naval Academy, Varna, Bulgaria

   ***Dilyana Dimitrova**, Department of Information Technologies,*
   Nikola Vaptsarov Naval Academy, Varna, Bulgaria

5. **DESIGN OF LORA-INTEGRATED WEARABLE SYSTEM FOR SAILOR TRACKING IN MARITIME EMERGENCIES**

   ***Dilyana Dimitrova**, Department of Information Technologies,*
   Nikola Vaptsarov Naval Academy, Varna, Bulgaria

   ***Nadezhda Vladimirova**, Department of Information Technologies,*
   Nikola Vaptsarov Naval Academy, Varna, Bulgaria

BREAK

13h – 13h 30min

SECOND SESSION

13h 30min – 15h 30min

CHAIRMAN: ***Prof. Mariya Nikolova,** Department of Information Technology,*
Faculty of Engineering, Nikola Vaptsarov Naval Academy, Bulgaria

---

1. **MEASUREMENTS AND PATH LOSS MODELS AT 30 AND 300 MHZ OVER FLAT TERRAIN SCENARIOS**

   ***Nektarios Moraitis**, School of Electrical and Computing Engineering,*
   National Technical University of Athens, Greece,

   ***Panayiotis Frangos**, School of Electrical and Computing Engineering,*
   National Technical University of Athens, Greece

   ***Ileana Popescu**, School of Electrical and Computing Engineering,*
   National Technical University of Athens, Greece

   ***Alexandros Rogaris**, School of Electrical and Computing Engineering,*
   National Technical University of Athens, Greece

   ***Seil Sautbekov**, Department of Physics and Technology,*
   Al-Farabi Kazakh National University Almaty, Kazakshtan

2. **TERRAIN CLASSIFICATION BY USING A LARGE SET OF SYNTHETIC APERTURE RADAR IMAGES AND MODIFIED FRACTAL SIGNATURE METHOD**

   Petros Doukas, *School of Electrical and Computing Engineering,*
   National Technical University of Athens, Greece

   Basil Massinas*, School of Electrical and Computing Engineering,*
   National Technical University of Athens, Greece

   Faethon Karagiannopoulos*, School of Electrical and Computing Engineering,*
   National Technical University of Athens, Greece

   Panayiotis Frangos*, School of Electrical and Computing Engineering,*
   National Technical University of Athens, Greece

   Seil Sautbekov*, Department of Physics and Technology, Al-Farabi Kazakh National*
   University Almaty, Kazakshtan

3. **DIGITAL VISUALIZATION OF SPACE CONFIGURATION OF LOW-FREQUENCY MAGNETIC FIELD USING EXPERIMENTAL DATA GENERATED FROM SYSTEMS FOR MAGNETOTHERAPY**

   Vladimir Nikolov*, Faculty of Telecommunication,*
   Technical University of Sofia, Bulgaria

4. **ALGORITHM FOR PROCESS CONTROL WHEN MEASURING MAGNETIC INDUCTION GENERATED BY A MAGNETIC PHYSIOTHERAPY BED**

   Vladimir Nikolov*, Faculty of Telecommunication,*
   Technical University of Sofia, Bulgaria

5. **ESTIMATIONS OF REAL-WORLD ACOUSTIC DATA VIA COMPRESSED SENSING**

   I. Simeonov, N. Yordanov*, Vasil Levski National Military University,*
   Veliko Tarnovo, Bulgaria

6. **PROCESSING OF ACOUSTIC INFORMATION, CAPTURED IN A CLOSED ROOM VIA WIRELESS ACOUSTIC SENSOR NETWORK**

   Kostadin Panchev, Snezhana Georgieva Pleshkova*, Faculty of Telecommunication,*
   Technical University of Sofia, Bulgaria

October, 21st, 2025, Tuesday

THIRD SESSION

11h – 13h

CHAIRMAN: ***Prof. Veska Georgieva,*** *Faculty of Telecommunication,*
Technical University of Sofia, Bulgaria

---

1. **ELABORATING 3D BLUEPRINT OF A CONVEYOR AND ITS APPLICATION IN INDUSTRIAL COMMUNICATION NETWORKS**

   Daniel Denev, Silvia Nikolova, Tsvetoslav Tsankov,
   Faculty of Technical Sciences, Konstantin Preslavsky University of Shumen, Bulgaria

2. **COMPARATIVE ANALYSIS OF THE PERFORMANCE OF DEEP LEARNING-BASED AI FOR VIDEO CAMERAS WORKING WITH DIFFERENT DATABASES**

   Silvia Nikolova, Daniel Denev, Tsvetoslav Tsankov,
   Faculty of Technical Sciences, Konstantin Preslavsky University of Shumen, Bulgaria

3. **ANALYSIS OF THE IMPACT OF ARTIFICIAL INTELLIGENCE ON THE COURSE OF DEVELOPMENT IN ENGINEERING EDUCATION**

   Maria Pavlova, *Technical University of Sofia, Bulgaria*

4. **LABORATORY SESSION ON SPECTRUM SENSING**

   Ludwig Lubich*, Faculty of Telecommunications, Technical University of Sofia, Bulgaria*

5. **AN AI-POWERED FRAMEWORK FOR REAL-TIME WILDFIRE DETECTION USING THERMAL IMAGING (THERMOVISION)**

   Svetlin Antonov*, Faculty of Telecommunications,*
   Technical University of Sofia, Bulgaria

6. **A CONCEPTUAL FRAMEWORK AND PYTHON SIMULATION OF AN INTELLIGENT FIRE SUPPRESSION SYSTEM TRIGGERED BY THERMOVISION ANALYSIS**

   Svetlin Antonov*, Faculty of Telecommunications,*
   Technical University of Sofia, Bulgaria

BREAK

13h – 13h 30min

FOURTH SESSION

13h 30min – 15h 30 min

CHAIRMAN: ***Assoc. Prof. Ivan Ivanov,*** *Vasil Levski National Military University,*
Veliko Tarnovo, Bulgaria

---

1. **OPERATOR METHODS FOR MODELING LINEAR OPTICAL SYSTEMS**

   Kostadin Sheiretsky, Svetlin Antonov*, Faculty of Telecommunications,*
   Technical University of Sofia, Bulgaria

2. **ASYMPTOTIC DECOMPOSITION OF A SCALAR FUNCTION OF MANY VARIABLES AND APPLIED IN THERMOVISUAL SYSTEMS**

   Kostadin Sheiretsky, Svetlin Antonov*, Faculty of Telecommunications,*
   Technical University of Sofia, Bulgaria

3. **METHOD FOR ANALYSIS OF THE IMPACT OF THE FIELDS FIRES ON THE TRAFFIC SITUATION**

   Ivan Antonov, Kamen Grozdanov*, Faculty of Telecommunications,*
   Technical University of Sofia, Bulgaria

4. **THERMO-PHYSICAL CHARACTERIZATION OF CONIFEROUS LITTER FOR TECHNICAL-ASSISTED WILDFIRE EARLY WARNING**

   Hrisimir Dochev, Anelia Tzanova*, Faculty of Telecommunications,*
   Technical University of Sofia, Bulgaria

   Detelin Spasov*, Academy of the Ministry of the Interior, Sofia, Bulgaria*

5. **COMPARATIVE COMBUSTION ANALYSIS OF DECIDUOUS FOREST LITTER WITH RADAR BACKSCATTER CORRELATION**

   Hrisimir Dochev, Anelia Tzanova*, Faculty of Telecommunications,*
   Technical University of Sofia, Bulgaria

   Detelin Spasov*, Academy of the Ministry of the Interior, Sofia, Bulgaria*

6. **INTEGRATED COMMUNICATION ARCHITECTURE FOR FOREST-FIRE RESPONSE IN BULGARIA: GAP ANALYSIS AND DESIGN BLUEPRINT**

   Hrisimir Dochev, *Faculty of Telecommunications,*
   Technical University of Sofia, Bulgaria

CLOSING CONFERENCE

15h 30min – 16h

CONTACT US:

http://rcvt.tu-sofia.bg/CEMA/eth.html

Prof. Dr. Dimiter Dimitrov

Faculty of Telecommunication
Technical University of Sofia
8, Kliment Ohridsky str.
1756 Sofia, Bulgaria
Phone:++359 2 9652278
Fax: ++359 2 9652278
E-mail: dcd@tu-sofia.bg

Prof. P. Frangos

National Technical University of Athens
School of Electrical and Computer Engineering
9, Iroon Polytechniou Str. ,
157 73 Zografou, Athens, Greece
Phone : 00 30 210 772 3694
Fax : 00 30 210 772 2281
E-mail : pfrangos@central.ntua.gr

TABLE OF CONTENTS

THE INFLUENCE OF DIAGNOSIS AND ETHNIC BACKGROUND ON THE CHOICE OF CARE ENVIRONMENT FOR CHILDREN WITH NEURODEVELOPMENTAL DISORDERS

Kalina Georgieva – Bozhkova

Department of Material Science and Prosthetic Dental Medicine
Faculty of Dental Medicine, Medical University – Varna, Bulgaria
E-mail: dr.kalina.georgieva.dm@gmail.com

Anna Nenova – Nogalcheva

Department of Oral Surgery
Faculty of Dental Medicine, Medical University – Varna, Bulgaria
E-mail: anenova@yahoo.com

Mariya Nikolova

Department of Information Technology, Faculty of Engineering
Nikola Vaptsarov Naval Academy, Bulgaria
Varna 9026, 73 V. Drumev str.
E-mail: mpn@abv.bg

Emiliya Koleva

Department of Electronics, Faculty of Engineering
Nikola Vaptsarov Naval Academy, Bulgaria
Varna 9026, 73 V. Drumev str.
E-mail: e.koleva@nvna.eu

Desislava Konstantinova

Department of Material Science and Prosthetic Dental Medicine
Faculty of Dental Medicine, Medical University – Varna, Bulgaria
E-mail: dr.konstantinova@gmail.com

Abstract

This study presents findings aimed at examining the relationship between a children's diagnosis and the characteristics of their caregiving environment. The analysis focuses on the impact of ethnic background on the type and quality of care provided to children with neurodevelopmental conditions. The results indicate significant differences in the ways ethnic groups in Bulgaria care for their children. The study enrolled 120 children diagnosed with various neuropsychiatric conditions from Northeastern Bulgaria.

1. INTRODUCTION

According to data from the most recent national census conducted in Bulgaria in 2021, the country's ethnic composition is predominantly Bulgarian (84.6%), followed by Turkish (8.4%) and Roma (4.4%) populations, while other ethnic minority groups—including Russians, Armenians, Tatars, Vlachs, Greeks, and others—collectively account for less than 0.5% of the total population. The region of Northeastern Bulgaria is characterized by notable ethnocultural diversity, which provides an important context for research on neurodevelopmental disorders in children.

Ethnic background of children and their families remains an underexplored factor in relation to the risk and manifestation of autism spectrum disorder (ASD) and other neurodevelopmental conditions. International studies suggest that both ethnic origin and parental migration status may influence not only the likelihood of developing such disorders but also the timeliness of their recognition and diagnosis. Research conducted in Finland, Australia, and the United States has demonstrated that children born to immigrant mothers or belonging to specific ethnic groups have a higher risk of developing ASD [1, 2].

Cultural attitudes, language barriers, and differential access to healthcare services are considered potential mechanisms underlying these observed disparities among ethnic groups. A review of the scientific literature revealed no evidence of similar studies conducted in Bulgaria.

Purpose: The aim of this study is to examine the influence of ethnic background and diagnosis on the type of care provided to children with autism spectrum disorder and other neurodevelopmental impairments in Northeastern Bulgaria.

2. MATERIAL AND METHODS

2.1. Study Setting and Participants

This research was carried out in Varna, Bulgaria over a seven-month period, from April to October 2017. Ethical approval was granted by the Ethics Committee of Research at the Medical University of Varna (Protocol No. 60/23.2.2017). The study enrolled 120 children diagnosed with various neuropsychiatric conditions from the cities of Varna and Ruse. Of these participants, 64 resided in residential care facilities, while 56 lived with their families. The diagnostic distribution included 46 children with cerebral palsy (CP), 11 with hydrocephalus, 13 with mild intellectual disability (ID-Mild), 4 with moderate intellectual disability (ID-Moderate), 8 with severe intellectual disability (ID-Severe), 14 with autism, 12 with Down syndrome or other genetic syndromes, and 12 with autism spectrum disorder (ASD).

2.2. Examination Procedure

A demographic profile form was developed to collect essential participant information, including name, ethnicity, age, primary diagnosis, place of residence, and related sociodemographic variables. For children raised in a family environment, this information was provided by a parent, whereas for those residing in institutional care facilities, it was completed by the facility's administrator.

2.3. Sample Size

A total of 120 children participated in the study, ranging in age from 4 months to 16 years and 8 months, with a mean age of 5 years and 9 months. The general characteristics of the patients are described in table 1.

TABLE 1.
Baseline Characteristics of Patients

Characteristics	Girls (n=51)	Boys (n=69)
Age (years)	5.48	5.77
Diagnosis:		
- Cerebral palsy	20	26
- Hydrocephalus	7	4
- ID-Mild	4	9
- ID-Moderate	3	1
- ID-Severe	3	5
- Autism	4	10
- Dawn and other syndromes	9	3
- ASD	1	11
Ethnicity:		
Bulgarian	27	43
Turkish	6	9
Romani	18	12

The cohort encompassed multiple ethnic backgrounds and a variety of medical conditions, with a subset of participants placed under state institutional care. Most of the children were of Bulgarian ethnicity (58%). To our knowledge, this is the first study to specifically examine the role of ethnicity in shaping care practices for children diagnosed with ASD and other neurodevelopmental impairments. Due to unknown parental information, data on ethnic background were unavailable for two boys—one diagnosed with cerebral palsy and the other with ID-Mild.

The largest subgroup—46 children or 38.33% of the total sample—were diagnosed with cerebral palsy. A total of 25 children (20.83%) were diagnosed with intellectual disability. For the remaining diagnostic categories, the number of children was relatively evenly distributed, each - approximately 10% of the sample. Furthermore, the number of male participants (69 boys) exceeded that of female (51 girls) by approximately 15%.

2.4. Statistical Analysis

To summarize, describe, organize and visualize the data are used descriptive statistical methods. Spearman's rank correlation coefficient was applied to assess associations between variables where dependencies were observed. Statistical analyses were conducted using MATLAB and Jamovi software.

3. RESULTS

3.1. Child's Primary Diagnosis and its Relationship to the Care Environment

Table 2 summarizes the characteristics of the children enrolled in the study, stratified by their primary diagnosis and living arrangements, either in familial care or institutional settings.

TABLE 2.
Children Raised in Residential Care/Family Care

Diagnosis	Count	
	Residential care	Family care
ID-Mild	5	8
Autism	2	12
Cerebral palsy	33	13
hydrocephalus	7	4
ID-Severe	8	0
ID-Moderate	1	3
PDD	0	12
Dawn and other syndromes	8	4

As delineated in Table 2, 64 children are residing in institutional care facilities, whereas 56 children receive care within a familial environment. It is noteworthy that children diagnosed with speech and language disorders are exclusively reared in home settings. Furthermore, it is striking that all children diagnosed with severe intellectual disability are placed in residential care institutions.

3.2. Analysis of the Distribution of the Study Cohort by Age and Care Environment

The influence of the children's age on parental decisions regarding the place of care for the affected child cannot be definitively established. In fact, the current sample itself reflects age-related variability, as the study includes children with diverse age characteristics. Moreover, we lack data on the timing of diagnosis and/or institutionalization, precluding a conclusive analysis of this factor.

Figure 1 illustrates the distribution of children raised in institutional care and family environments according to their age. A noticeable trend is the decline in the number of children over 10 years of age in both residential settings.

This observation raises the question of whether there is a relationship between increasing age and type of care placement. Given that the data for both groups—children living in institutions and those in family settings—do not follow a normal distribution, Spearman's rank correlation coefficient was employed to assess the association between age and care environment. The results indicate a moderate negative correlation in both groups between age and the number of children in institutional care (Spearman's $\rho = -0.6039$, $p = 0.0103 < 0.05$) and family care (Spearman's $\rho = -0.6151$, $p = 0.0086 < 0.05$), suggesting that as age increases, the number of children in both types of care decreases.

Figure 1. The Relation Between Children's Ages and the Place of Residence

Caring for children with neurodevelopmental disorders within a family environment may present significant challenges for families, often requiring substantial compromises in their quality of life [3]. In cases involving children with more severe disabilities, professional care provided in residential institutions for long-term support offers an opportunity for more appropriate and specialized management [4].

3.3. Influence of Parental Ethnicity on the Decision to Raise Children in a Family Environment vs Residential Care Facilities

Figure 2 illustrates the number of children referred to their ethnic background.

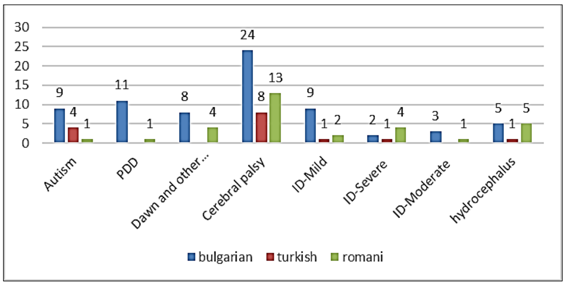

Figure 2. Children's Distribution by Diagnosis and Ethnicity

Bulgarian children constitute the majority of the study population, whereas children of Turkish origin represent the smallest group.

Table 3 provides detailed information on children raised in a family environment, stratified by diagnosis and ethnicity. For instance, examining the first row of Table 3 shows that 46% of Bulgarian children diagnosed with cerebral palsy are cared for in a family environment. Notably, only 13% of Turkish-origin children and 8% of Romani children with cerebral palsy are raised within a family setting. Overall, most Bulgarian children (68.6%) are reared in family environments, whereas Romani children are predominantly placed in residential care institutions.

TABLE 3.
Children Reared in Home Environment (in %) with Respect of Ethnicity and Diagnosis

	Bulgarian	Turkish	Romani	no data
Cerebral palsy	46%	13%	8%	0%
Hydrocephalus	80%	0%	0%	-
ID-Mild	78%	100%	0%	0%
ID-Moderate	100%	-	0%	-
ID-Severe	0%	0%	0%	
Autism	89%	100%	0%	
Dawn and other syndromes	50%	-	0%	
ASD	100%	-	100%	

The results of this study indicate significant differences in the ways various ethnic groups in Bulgaria care for their children with neurodevelopmental difficulties. Bulgarian families are more likely to provide care at home, even in cases involving severe conditions such as autism or cerebral palsy. In contrast, Roma families more frequently rely on institutional care, which appears to be linked to certain social and systemic challenges, such as limited access to healthcare services and support [5,6].

Some studies suggest that Roma children in Bulgaria are at higher risk of mental health difficulties, such as anxiety, depression, and behavioural problems, compared to children from other ethnic backgrounds [7,8].

Common issues such as poverty, language barriers, lack of documentation, and discrimination further hinder access to timely support and contribute to poorer long-term outcomes [6].

Global researches also indicate that ethnic and cultural differences influence the timing and process of autism diagnosis. In countries such as the United Kingdom and the United States, children from ethnic minority backgrounds are less likely to receive diagnosis on time. This is often attributed to a lack of trust in institutions and social exclusion [9,10].

Despite the challenges, research shows that Roma families tend to have strong family relationships, and children often demonstrate positive social behaviour [8, 11]. This suggests that the Roma community is not homogeneous and that, with appropriate support, it can provide a stable and nurturing family environment.

Our study also observed strong family support among Turkish families, who similarly prefer to care for their children with autism at home. This aligns with findings from Turkey, where families also assume primary caregiving responsibilities, even in the presence of behavioural challenges and comorbid medical conditions [12]. This suggests that ethnicity is not the only determining factor—social support, cultural values, and access to services also play a crucial role.

Other vulnerable groups also exist, such as Black children and girls with autism, whose symptoms often are not recognized on time [13]. This highlights the importance of tailoring diagnostic approaches to the cultural and social contexts of each child and their family.

4. CONCLUSION

In conclusion, the findings indicate that Bulgarian families tend to care for children at home, even in severe cases such as autism or cerebral palsy, whereas Roma families more often resort to institutional care. This disparity appears to stem from underlying social and systemic barriers, including restricted access to healthcare services and support mechanisms.

As a pilot investigation into the potential statistical associations between parental ethnicity and the upbringing environment of children with neurodevelopmental disorders, this study provides fundamental insights and reference points for future research. It could elucidate the timing at which these children are placed in institutional care—immediately after birth or at a later stage—or whether an initial attempt is made to care for them at home. Additionally, such studies might address the question of whether the lifespan of these children tends to be limited.

It would be pertinent to conduct future research aimed at elucidating whether this phenomenon is attributable to the increased care demands associated with the specific characteristics of these disorders.

References

[1] V. Lehti, S. Hinkka-Yli-Salomäki, K. Cheslack-Postava et al., "The risk of childhood autism among second-generation migrants in Finland: A case–control study", *BMC Pediatrics, 13*, 171, 2013. https://doi.org/10.1186/1471-2431-13-171

[2] D. Keen, F. Reid, D. Arnone, "Autism, ethnicity and maternal immigration", *British Journal of Psychiatry, 196*(4), 2010, pp. 274–281, https://doi.org/10.1192/bjp.bp.109.065490

[3] S. Faden, N. Merdad, Y. Faden. "Parents of Children With Neurodevelopmental Disorders: A Mixed Methods Approach to Understanding Quality of Life, Stress, and Perceived Social Support". *Cureus. 10;* 15(4):e37356, 2023, doi: 10.7759/cureus.37356.

[4] V. Gall, J. Buchhalter, R. Antonelli et al. "Improving Care for Families and Children with Neurodevelopmental Disorders and Co-occurring Chronic Health Conditions Using a Care Coordination Intervention". J Dev Behav Pediatr. 01;43(8):444-453, 2022. doi: 10.1097/DBP.0000000000001102.

[5] S. Atkinson, L. Ayre, G. Mitreva et al. "Access to health care for Roma children in Central and Eastern Europe: A qualitative study from Bulgaria", International Journal for Equity in Health, 8, 24, 2008, https://doi.org/10.1186/1475-9276-8-24

[6] B. Rechel, C. Blackburn, N. Spencer et al. "Access to health care for Roma children in Central and Eastern Europe: Findings from a qualitative study in Bulgaria", International Journal for Equity in Health, 8, 24, 2009, https://doi.org/10.1186/1475-9276-8-24

[7] M. Beresnevaite, D. Purper-Ouakil et al., "Mental health disparities between Roma and non-Roma children in Bulgaria and Romania", BMC Psychiatry, 14, 297, 2014, https://doi.org/10.1186/s12888-014-0297-5

[8] E. Lee, K. Keyes, A. Bitfoi, Z. Mihova, O. Pez, E. Yoon, V. Masfety, "Mental health disparities between Roma and non-Roma children in Romania and Bulgaria", BMC Psychiatry, 14, 297, 2014, https://doi.org/10.1186/s12888-014-0297-5

[9] C. Nevison, W. Parker, "California autism prevalence by county and race/ethnicity: Declining trends among wealthy Whites", Journal of Autism and Developmental Disorders, 50(11), 2020, pp. 4011–4021, https://doi.org/10.1007/s10803-020-04460-0

[10] A. Roman-Urrestarazu, R. van Kessel, C. Allison, F. Matthews, C. Brayne, S. Baron-Cohen, "Association of race/ethnicity and social disadvantage with autism prevalence in 7 million school children in England", JAMA Pediatrics, 175(6), 2021, e210054. doi:10.1001/jamapediatrics.2021.0054

[11] R. Dimitrova, V. Jordanov, "Do family ethnic pressure and national identity enhance psychological well-being among Roma youth in Bulgaria?", Special Issue on Roma youth, The Journal of the International Network for Prevention in Child Maltreatment, 40–41, 23–35, 2015.

[12] C. Doenyas, B. Ekici, Ö Unay, İ. Gönen, B. Tatlı, "Autism in Turkey: Demographics, behavior problems, and accompanying medical conditions in a sample of Turkish youth with autism spectrum disorder", International Journal of Developmental Disabilities, 69(2), 2021, pp.179–189, doi:10.1080/20473869.2021.1937001

[13] M. Diemer, E. Gerstein, A. Regester, "Autism presentation in female and Black populations: Examining the roles of identity, theory, and systemic inequalities" Autism, 26(8), 2022, pp. 1931–1946, https://doi.org/10.1177/13623613221113501

THE INFLUENCE OF DIAGNOSIS AND ETHNIC BACKGROUND ON THE CHOICE OF CARE ENVIRONMENT FOR CHILDREN WITH NEURODEVELOPMENTAL DISORDERS

Kalina Georgieva – Bozhkova

Department of Material Science and Prostethic Dental Medicine
Faculty of Dental Medicine, Medical University – Varna, Bulgaria
E-mail: dr.kalina.georgieva.dm@gmail.com

Emiliya Koleva

Department of Electronics, Faculty of Engineering
Nikola Vaptsarov Naval Academy, Bulgaria
Varna 9026, 73 V. Drumev str.
E-mail: e.koleva@nvna.eu

Mariya Nikolova

Department of Information Technology, Faculty of Engineering
Nikola Vaptsarov Naval Academy, Bulgaria
Varna 9026, 73 V. Drumev str.
E-mail: mpn@abv.bg

Anna Nenova – Nogalcheva

Department of Oral Surgery
Faculty of Dental Medicine, Medical University – Varna, Bulgaria
E-mail: anenova@yahoo.com

Desislava Konstantinova

Department of Material Science and Prostethic Dental Medicine
Faculty of Dental Medicine, Medical University – Varna, Bulgaria
E-mail: dr.konstantinova@gmail.com

Abstract

The paper presents a study on facial symmetry on 120 children with neurodevelopmental disorders, following the completion of informed consent forms by their parents.

The research examined the prevalence of facial symmetry deviations in relation to diagnosis, parental age, and living environment (family vs. institutional care), and explored potential associations with the presence of facial scars.

The results indicate that children with facial deformities among raised in family environment are less common, compared to those in institutional care. The highest percentage of facial asymmetry was observed in children with moderate intellectual disabilities. Notably, an absence of at least two facial symmetries was found only among children with cerebral palsy, generalized developmental disorders, and moderate intellectual disabilities—all of whom were raised in residential care facilities.

1. INTRODUCTION

Facial symmetry plays a crucial role in human aesthetics and is often associated with normal craniofacial development. Neurological and genetic disorders such as cerebral palsy, hydrocephalus, intellectual disabilities (ID), Down syndrome, autism spectrum disorder (ASD), and other syndromes can influence craniofacial morphology, potentially leading to visible facial asymmetries [1]. These asymmetries may affect both the functional and psychosocial well-being of affected children [2].

Previous studies have demonstrated a higher prevalence of craniofacial deviations among children with neurodevelopmental disorders compared to the general population [3]. Morphological alterations may arise due to factors such as abnormal muscle tone, asymmetric growth patterns, or underlying genetic mutations [4]. However, comprehensive clinical and statistical evaluations of facial symmetry across multiple pediatric diagnoses remain limited, particularly in Eastern European populations [5, 6].

Analysis of facial abnormalities could be a potential diagnostic biomarker that could aid in the early detection of autism spectrum disorders [6].

Purpose: The aim of the study is to assess the prevalence of facial symmetry deviations in relation to diagnostic category, parental age, and type of living environment (family-based versus institutional care), and to investigate potential associations with the presence of facial scars.

2. MATERIAL AND METHODS

2.1. Sample Size

Study Design: This was a non-invasive observational study conducted between April and October 2017.

Participants: The study population comprised 120 children. Participation was granted following the submission of written informed consent forms signed by parents or legal guardians.

Data Collection: Clinical evaluation was performed to assess facial symmetry and the presence of facial scars. Information regarding diagnosis, parental age, and living environment (family-based or institutional care) was also collected. Data were recorded in standardized forms to ensure consistency and comparability across participants.

Ethical Considerations: Ethical approval for the study was obtained from the Ethics Committee of Research at the Medical University of Varna (Protocol No. 60/23.2.2017).

2.2. Statistical Analysis

The collected data were summarized using descriptive statistics. Comparisons between groups according to diagnosis, parental age, and living environment (family-based versus institutional care) were performed. Associations between the presence of facial scars and facial asymmetry were also evaluated. The data were analysed using Matlab and Jamovi software.

3. RESULTS

3.1. Parental Age by Ethnicity

Table 1 presents the mean parental age at the time of birth of the studied children. The highest values were observed among parents of Turkish origin. Overall, the mean age of mothers exceeded the national averages for Bulgaria reported for 2024 (27.6 years at the birth of the first child and 29.1 years at the birth of a child) [7]. For more than half of the parents, the child included in this study was their only offspring.

TABLE 1.

Mean Age of Parents and Number of Children According to Ethnicity

	Mean age at birth		Number of families	
	Mother	Father	One child	More children
Bulgarian	34,7	39,14	44	27
Turkish	42,9	47,24	5	10
Romani	41,57	44,7	16	15

3.2. Influence of Diagnosis on the Presence of Facial Asymmetries

The data in tables 2 and 3 indicate that the number of children raised in a family environment who are with facial deformities is low (8 out of a total of 35). Among the 46 children diagnosed with cerebral palsy, only 29 exhibited facial symmetry, while the remaining 17 demonstrated the absence of at least one of the four types of symmetry assessed. Of these children, only one was raised in a family setting. The findings suggest that facial asymmetry is relatively common among children with cerebral palsy and is more frequently observed in those raised in institutional care. This may reflect the multifactorial challenges faced by families in providing home care for children with both neurological impairment and craniofacial deviations. The results highlight the need for early interdisciplinary support—medical, rehabilitative, and psychosocial—aimed at improving both functional outcomes and quality of life for affected children and their families.

Cases of children lacking two types of facial symmetry were observed exclusively among those diagnosed with cerebral palsy, generalized developmental disorders, and moderate intellectual disability. All such cases (a total of seven children) were found in institutional care

TABLE 2.

Distribution of Children by Diagnosis and by Symmetry Relative to the Sagittal Plane Across the Cerebral and Respiratory Facial Regions

Diagnosis	Symmetry relative to the sagittal plane -count		Symmetry relative to cerebral/ respiratory facial regions -count	
	yes	no/family care	yes	no/family care
Cerebral palsy	40	6/1	40	6/0
Hydrocephalus	11	0/0	10	1/1
ID-Mild	11	2/1	12	1/0
ID-Moderate	3	1/0	4	0/0
ID-Severe	8	0/0	8	0/0
Autism	13	1/1	14	0/0
Dawn and other syndromes	12	0/0	10	2/0
ASD	10	2/2	11	1/1

TABLE 3.

Distribution of Children by Diagnosis and by Symmetry Relative to the Cerebral, Respiratory, and Masticatory Facial Regions

Diagnosis	Symmetry relative to respiratory/ masticatory facial regions -count		Symmetry relative to cerebral/ masticatory facial regions -count	
	yes	no/family care	yes	no/family care
Cerebral palsy	40	6/0	43	3/0
Hydro-cephalus	11	0/0	10	1/0
ID-Mild	12	1/1	12	1/1
ID-Moderate	3	1/1	3	1/1
ID-Severe	7	1/0	7	1/0
Autism	14	0/0	14	0/0
Dawn and other syndromes	11	1/0	10	2/0
ASD	12	0/0	11	1/1

Figure 1 illustrates the percentage distribution of children with at least one type of facial asymmetry according to diagnosis.

Among children with autism spectrum disorder, only one case of facial asymmetry was identified, suggesting a very low prevalence in this group. This finding may indicate that facial asymmetry is not a characteristic feature of autism spectrum disorder, in contrast to other neurodevelopmental and genetic conditions where such deviations are more frequently observed.

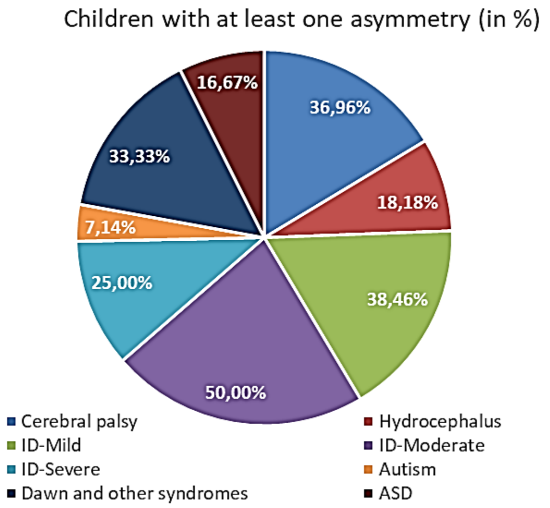

Figure 1. Distribution of Children with Facial Asymmetry (%) by Diagnosis

From the children diagnosed with cerebral palsy, Down syndrome, other genetic syndromes, and mild intellectual disability, approximately one-third exhibited some form of facial asymmetry. The highest prevalence was observed in the group with moderate intellectual disability, where 50% of the children presented with asymmetry. It is possible that the observed asymmetry reflects disease-specific features. Nevertheless, given the very limited number of children in this diagnostic group, these findings should be interpreted with caution and cannot be regarded as statistically significant.

The results shown in figure 1 indicate that more severe neurological impairments are associated with a higher likelihood of facial asymmetry. Similar results have been reported in other studies. For example, Aldridge et al. [8, 9] reported that in children with autism and other spectrum disorders, subtle but significant differences in facial morphology were observed, reflecting fundamental deviations in brain development already during the embryonic period.

In children diagnosed with hydrocephalus, although the number of cases was small, cranial and facial alterations were observed. This corresponds to the results published by Hale et al. [10] which demonstrate that disturbances in cerebrospinal fluid circulation can lead to structural deformities of the skull and face. These findings suggest that disturbances in cerebrospinal fluid circulation may contribute to structural cranial and facial deformities

3.3. Analysis of Disease-Related Factors in Scar Formation

A cicatrix represents the fibrous connective tissue that replaces normal skin or mucosa following injury, surgery, or disease. It develops as the final stage of the wound healing process, during which fibroblasts produce collagen fibers that gradually remodel the affected area. Clinically, cicatrices may vary in thickness, color, and elasticity, ranging from thin, flat, and inconspicuous scars to hypertrophic or keloid formations. Depending on their localization and extent, cicatrices can cause functional limitations, contractures, or esthetic concerns.

Figure 2 presents the distribution of children with cicatrices by diagnosis.

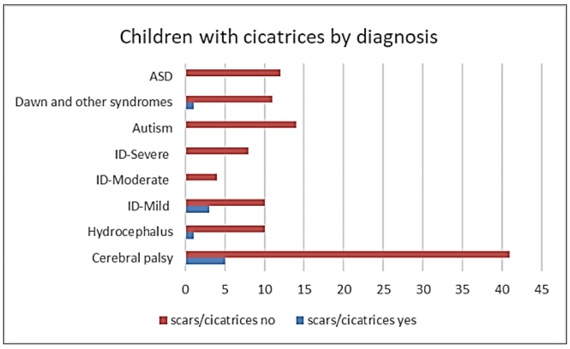

Figure 2. Distribution of cicatrices across diagnostic groups

The total number of children with cicatrices was 10, of whom only 3 presented with facial asymmetry. Therefore, no association can be established between the presence of scars and facial asymmetry. Cicatrices were not specific to children diagnosed with generalized developmental disorders, autism, Down syndrome and other genetic syndromes, moderate or severe intellectual disability, or hydrocephalus. Among a total of 61 children with these conditions, scars were observed in only two cases.

The total number of children with facial asymmetries is 35. Of these, 17 are of Bulgarian origin, 5 of Turkish origin, and 12 of Roma origin; ethnicity data is missing for one child. Notably, all Roma children are raised in institutional care, whereas 50% of the Bulgarian children (9 out of 17) are raised in a family environment. The percentage distribution of children with facial deformities according to ethnicity is presented in Table 4.

TABLE 4.

Children with Asymmetry Distributed by Ethnicity

Ethnicity	Total count	Children with facial asymmetry	
		Count	% from all
Bulgarian	70	17	24,29%
Turkish	15	5	33,33%
Romani	30	12	40,00%

4. CONCLUSION

This study demonstrated that facial asymmetry is relatively common among children with neurological and genetic disorders, particularly cerebral palsy, Down syndrome, and moderate intellectual disability, whereas it was rarely observed in autism spectrum disorder.

No association was identified between the presence of cicatrices and facial asymmetry, and scar formation was not specific to any diagnostic group. Ethnic differences were observed, with Roma children more often raised in institutional care, while half of the Bulgarian children with asymmetry were raised in a family environment.

References

[1] P. Hammond, C. Forster-Gibson, A. Chudley, J. Allanson, T. Hutton, S. Farrell, J. McKenzie, J. Holden, M. Lewis, "Face-brain asymmetry in autism spectrum disorders" Molecular Psychiatry, 13(6), pp.614–623, 2008, https://doi.org/10.1038/mp.2008.18

[2] C. Kau, S. Richmond, C. Savio, C. Mallorie "Measuring adult facial morphology in three dimensions", The Angle Orthodontist, 76(5), pp.773–778, 2006, https://doi.org/10.1043/0003-3219(2006)076[0773:MAFMIT]2.0.CO;2

[3] D. Tan, S. Gilani, M. Boutrus, G. Alvares, A. Whitehouse, A. Mian, D. Suter, M. Maybery, "Facial asymmetry in parents of children on the autism spectrum", Autism Research, 14(11), 2021, pp. 2260–2269. https://doi.org/10.1002/aur.2612

[4] A. Jamilian, K. Ferati, A. Palermo, A. Mancini, R. Rotolo, "Craniofacial development of the child", European Journal of Musculoskeletal Diseases, 11(3), 2022, pp. 89–95.

[5] L. Maniscalco, B. Frédérique, M. Roccella, D. Matranga, G. Tripi, "A preliminary study on cranio-facial characteristics associated with minor neurological dysfunctions (MNDs) in children with autism spectrum disorders (ASD)", Brain Sciences, 10(8), 566. https://doi.org/10.3390/brainsci10080566

[6] G. Quatrosi, D. Genovese, G. Galliano, H. Zoppé, E. Amodio, F. Bonnet-Brilhault, G. Tripi, "Cranio-facial characteristics in autism spectrum disorder: A scoping review",

Journal of Clinical Medicine, 13(3), 2024, 729. https://doi.org/10.3390/jcm13030729

[7] National Statistical Institute of Bulgaria, Average age of the mother at birth by place of residence, statistical regions and districts, 2024, https://www.nsi.bg/statistical-data/217/692

[8] K. Aldridge, I. George, K. Cole, J. Austin, T. Takahashi, Y. Duan, J. Miles, “Facial phenotypes in subgroups of prepubertal boys with autism spectrum disorders are correlated with clinical phenotypes”, Molecular Autism, 2(1), 2011, 15. https://doi.org/10.1186/2040-2392-2-15

[9] G. Tripi, S. Roux, D. Matranga, L. Maniscalco, P. Glorioso, F. Bonnet-Brilhault, M. Roccella, “Cranio-facial characteristics in children with autism spectrum disorders (ASD)”, Journal of Clinical Medicine, 8(5), 2019, 641. https://doi.org/10.3390/jcm8050641

[10] A. Hale, H. Boudreau, R. Devulapalli, P. Duy, T. Atchley, M. Dewan, M. Goolam, G. Fieggen, H. Spader, A. Smith, J. Blount, J. Johnston, B. Rocque, C. Rozzelle, Z. Chong, J. Strahle, S. Schiff, K. Kahle, “The genetic basis of hydrocephalus: Genes, pathways, mechanisms, and global impact”, Fluids and Barriers of the CNS, 21(1), 2024, 24. https://doi.org/10.1186/s12987-024-00513-z

ON THE ANALYSIS OF THYROID GLAND ULTRASONIC IMAGES BY THE METHODS OF HARALIC AND LOCAL DENSITY FUNCTION

V. Lyamin

St.Petersburg State University
st067898@student.spbu.ru

I. Soloviev

St.Petersburg State University
i.soloviev@spbu.ru

N. Ampilova

St.Petersburg State University
n.ampilova@spbu.ru

Abstract

Ultrasonic diagnostic is the simple and effective method for detection of anomalies of thyroid gland, and in particular nodules — new growths which are different from health tissue by echogenity.There are 3 types of nodules iso-,hyper- and non-echogenic. Isoehogenic nodules have the same density as the health tissue, and may be poorly distinguishable in the image. Two other types differ from health tissue by the brightness.

To reveal nodules we apply the machine learning method based on using Haralick texture features and multifractal spectrum. The image is represented by a set of non-overlapping blocks containing both normal tissue and nodules. The blocks are determined after preliminary markup performed by a medical specialist. Texture features are caculated for each block.

For machine learning SVM method was taken as a model, Thanks to the block-based approach, the application implements the capability to localize a nodule within the image.

The abstract is to be in 12-point, single-spaced type, and may be up to 100-150 words long. Skip two lines after the abstract before main text.

1. INTRODUCTION

The detection of anomalies in thyroid gland is important problem in medical research. Ultrasound diagnostic as one of effective methods allows fast revealing of nodules, which may be a sign of cancer. There are 3 types of nodules:

isoechogenic — have the density as normal tissue;

hyperechogenic — their density more than the density of normal tissue; on ultrasound images such nodules are more light than normal tissue;

non-*echogenic* — their density is less than for normal tissue; on images look more dark than normal tissue.

In medical clinic when studying a large number of images, it is important to have a program for fast revealing of nodules. In this paper we use Haralick texture features [1] and local density function values [2] and compare the results.

2. MATERIAL AND METHODS

For research we used ultrasonic images of thyroid gland obtained in Saint Petersburg State University Hospital. The images were preliminary marked up by medical specialists, after that the training set was formed. When studying we considered hyperechoic and non-echogenic nodules, because they contrast with base tissue and are easier to analyse. Isoechogenic nodules are not considered as they have brightness similar to base tissue and require more complex methods.

Images have size 1024x768 pixels. An image is partitioned on blocks of a given size. In what follows we use blocksize 32x32 pixels.

For correct network training we have to ensure a balance between the number of blocks containing normal tissue (class 1) and blocks with nodules (class 2). It gives a possibility to avoid the displacement of the model. Final set contains the maximum possible number of disjoint blocks.

For experiments we used 12 ultrasonic images of thyroid gland. After preliminary markup we evaluate the number of class 1 and class 2 blocks. To provide the same number of elements in these classes we choose the minimal value as the common one. When using block size 32×32 pixels we may obtain 114 blocks maximum.

The example of localization of the blocks is illustrated on Fig.1.

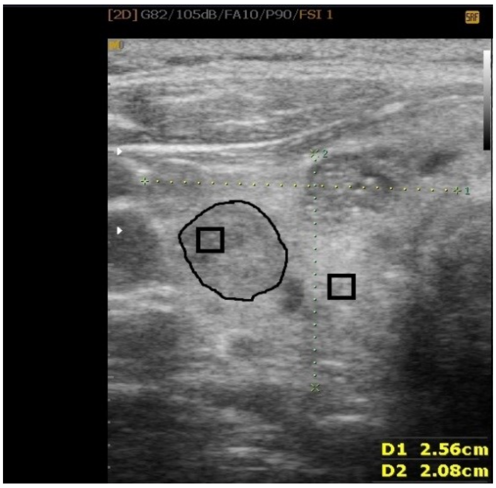

Figure 1. The nodule is enclosed by a curve. One square block is taken from nodule tissue, another block is taken from normal tissue

2.1. Haralick texture features

In the Haralick method [3] images are represented in grey scale palette. Information about the image structure is determined by space interrelations between pixels, calculated from their intensities and represented by 4 matrices. In these matrices intensities are indices, and value of an element P(i,j) is the number of neighbouring pixels with intensities i and j, such that the pixels are considered on a given distance and direction. In this method 4 directions are used: horizontal, vertical and diagonal. In denotations of [3] the directions are denoted by angles — 0, 90, 45 and 135 correspondingly.

Let in an image N_x be the number of pixels through horizontal, N_y — through vertical, and N_g — the number of grey levels. Consider areas $L_x = \{1, \dots, N_x\}$ and $L_y = \{1, \dots, N_y\}$, and the set of grey levels $G = \{1, \dots, N_g\}$. The function of the image is defined as $I: L_y \times L_x \to G$.

Define matrices P, where d is the size of the neighbor, angles define directions, and # denotes the number of elements in a set.

- $P_{d,0^\circ}(i,j) = \#\{((k,l),(m,n)) \in (L_y \times L_x) \times (L_y \times L_x) \big| k-m = 0, |l-n| = d, I(k,l) = i, I(m,n) = j\}$
- $P_{d,45^\circ}(i,j) = \#\{((k,l),(m,n)) \in (L_y \times L_x) \times (L_y \times L_x) \big| (k-m = d, l-n = -d) \vee (k-m = -d, l-n = d), I(k,l) = i, I(m,n) = j\}$
- $P_{d,90^\circ}(i,j) = \#\{((k,l),(m,n)) \in (L_y \times L_x) \times (L_y \times L_x) \big| |k-m| = d, l-n = 0, I(k,l) = i, I(m,n) = j\}$
- $P_{d,135^\circ}(i,j) = \#\{((k,l),(m,n)) \in (L_y \times L_x) \times (L_y \times L_x) \big| (k-m = d, l-n = d) \vee (k-m = -d, l-n = -d), I(k,l) = i, I(m,n) = j\}$

The example of calculations all these matrices for the image 4x4

I = 0 0 1 1
0 0 1 1
0 2 2 2
2 2 3 3

is given in detail in [3]. For example, the matrix $P_{1,0^\circ}$ has the form

4 2 1 0
2 4 0 0
1 0 6 1
0 0 1 2

It is easy to see that the number of neighbors with intensities 0, i.e. P(0,0) is 4 — in the first and the second row we have 2 neighbours. The element P(0,1) equals 2 as in the first row we have one pair and in the second row one as well, etc.

The obtained matrices P are normalized such that the sum of all elements equals 1. For each obtained matrix p we calculate mathematical expectations by row and columns (μ_x, μ_y), and variances (σ_x, σ_y) [4]. In the following formulas for brevity we omit indices of distance and angle:

- $\mu_x = \sum_{i=1} i \sum_{j=1} p\,(i,j)$
- $\mu_y = \sum_{i=j} j \sum_{i=1} p\,(i,j)$
- $\sigma_x = \sum_{i=1} (1 - \mu_x)^2 \sum_{j=1} p\,(i,j)$
- $\sigma_y = \sum_{j=1} (1 - \mu_y)^2 \sum_{i=1} p\,(i,j)$

Using matrices p(i,j) we can calculate 15 various features. We used the following ones:

- $f_1 = \sum_i \sum_j p\,(i,j)^2$ – uniformity. It describes smoothness of the image texture: if this value close to 1, pixel intensities have small variability.
- $f_2 = \sum_{n=0}^{N_g-1} n^2 \left(\sum_{|i-j|=n}^{N_g} p\,(i,j)\right)$ – conrast. It shows how many intensities of neighboring pixels differ.
- $f_3 = \frac{\sum_i \sum_j (ij)p(ij) - \mu_x \mu_y}{\sigma_x \sigma_y}$ – correlation. It measures the extent of linear dependence between intensities of neighboring pixels. Low correlation shows the existence of sharp borders in the image texture.
- $f_4 = -\sum_i \sum_j p\,(i,j) log\big(p(i,j)\big)$ — Shannon entropy. Shows the complexity of a given image.
- $f_5 = -\sum_i \sum_j \frac{1}{1+(i-j)^2} p(i,j)$ — homogeneity. This feature shows the closeness of intensities.

2.2. Local density function

This method uses assumptions and technics of fractal analysis. For a measure of a set, square as a rule, and its side the power law is supposed to be true. For each pixel a square neighbor is considered and some characteristic (local density function), which is an analogue of singularity exponent, is calculated. Pixels with close values of local density function form a level set. So, whole image may be represented as the union of nonintersecting level sets, which are binary images. Capacity dimensions of level sets give multifractal spectrum for the image. The method was described in [2] , and its application to various images is considered in [5,6].

For a point x from a set R consider a square B(x, r), where x is the center and r is radius (i.e. one half of the side). Denote by μ the measure of this neighbor and assume that the power law is true, i.e. $\mu\big(B(x,r)\big) = kr^{d(x)}$, where d(x) is so called local density function. This assumption is the main for fractal methods. Taking logarithms from the both sides of the equality and going to limit by r we obtain: $(x) = lim_{r\to 0} \frac{ln\mu\big(B(x,r)\big)}{lnr}$.

This function shows a power of non-uniformity of the distribution of intensities in a neighbor of a given point x. The measure of the neighbor may be calculated by different ways, the simplest one is the sum of pixel intensities. The points x having a given value of local density function α form the level set $E_\alpha = \{x \in I: d(x) = \alpha\}$. The number of points of an image is finite, so we may calculate $\alpha_{min}, \alpha_{max}$. In practice, to decrease the number of level sets one consider level sets of the form $E_\alpha = \{x \in I: d(x) \in [\alpha, \alpha + \varepsilon)\}$, where ε is defined experimentally. Thus, the image is partitioned on nonintersecting level sets, which may be easily interpreted as binary images and parameter ε determines their number. By calculating capacity dimensions for level sets we obtain multifractal spectrum of the image.

3. NEURAL NETWORK TRAINING

To apply machine learning we constructed feature vectors, containing texture characteristics calculated for each block of an image. The method of support vectors (SVM) from the library scikit-learn [7], was chosen as the model of machine learning. since this model has a simple API and is effective on small and medium-sized datasets.

Before training, the features were scaled to a common range to avoid the dominance of some features over others This is especially important for SVM, as the algorithm is sensitive to the data scale: distances between objects and the computation of separating boundaries directly depend on feature values. Without normalization, dominant features may unjustifiably shift the separating hyperplane, thereby reducing classification quality.

The scaling is the bringing each feature into the range [0,1]. The transformation was performed by the formula: $x_{scaled} = \frac{x - x_{min}}{x_{max} - x_{min}}$, where x_{min} and x_{max} are the minimum and maximum values of the given feature, respectively. The dataset was also divided into two groups: 80% for training and 20% for testing.

4. RESULTS OF EXPERIMENTS

4.1. Haralick method

To form the feature vector, we calculated selected texture features for each of 4 matrices p(i,j) . Then the arithmetic mean of each feature was computed. The experiments showed that the corresponding feature values in all four matrices are close, so this transformation has little effect on the model’s accuracy.

An example of a feature vector for one block is shown in Table 1. Very high values of contrast and entropy, along with low values of homogeneity and uniformity, indicate that the image contains many sharp transitions and a heterogeneous structure.

Table 1. Feature vector obtained by Haralick method

uniformity	0.0013
contrast	5857852.949
correlation	4.9924
entropy	6.8343
homogeneity	0.1213

In our experiments the combination of homogeneity, contrast, correlation and variance gave best results. The parameter d was taken by 1, and for simplification of the training we used mean values of features from 4 matrices.

At the first stage of the experiments, the optimal blocksize was determined. Square regions of sizes 20×20, 25×25, 32×32, and 35×35 pixels were considered. The model achieves the highest accuracy (the proportion of correct predictions among all predictions) with block size 32×32 pixels.

At the second stage, the dependence of the model’s accuracy on the color palette was investigated. The RGB, LAB, and HSV palettes were used. Since the original images are represented in grayscale, only the informative components — namely, their luminance characteristics — were used in each palette: in RGB space — the R (red) channel, as one of the identical channels; in LAB space — the L (lightness) component, with the a and b components, responsible for color tones, set to zero; in HSV space — the V (value) component, with saturation (S) and hue (H) set to zero. The highest accuracy was achieved with the RGB (0.91) and HSV (0.9) palettes.

4.2. Local density function

The values of the local density function were calculated for each point of an image by the least squares method. The experiments show that the model’s accuracy depends on the number of level sets E_α, that is, on the choice of ε.

For simplicity we take the number of level sets the same for all blocks. It should be noted that since the ranges of local density function values differ across blocks, fixing the number of level sets results in changing ε from block to block.

The following features were used for training the SVM model:

- the mean value of the interval of the local density function values for each level set;
- capacity dimensions of level sets.

The highest model accuracy (0.95) was achieved for 7 level sets. For example in Fig.2 the area of a nodule and 7 level sets are shown. The most informative are sets 2-5.

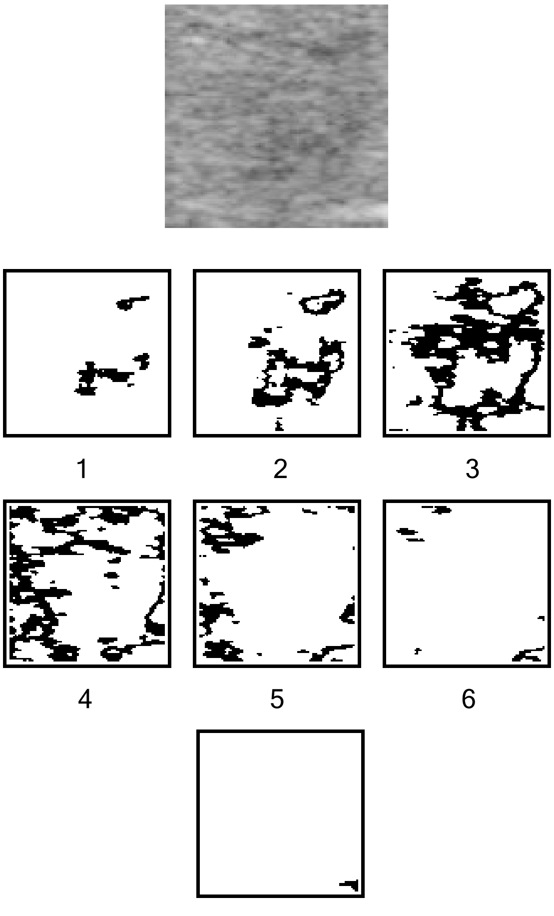

Figure 2. The example of a block and its level sets

Table 2.
Capacity dimensions for constructed level sets

level set number	interval d(x)	capacity dimension
1	[5.2,5.6)	1.28
2	[5.6,6)	1.58
3	[6,6.4)	1.79
4	[6.4,6.9)	1.78
5	[6.9,7.3)	1.59
6	[7.3,7.7)	1.16
7	[7.7,8.1)	0.62

5. SOFTWARE IMPLEMENTATION

For the practical implementation of the methods described above, a software application was developed in C#. The code for training the model was implemented in Python, since it provides a wide range of specialized libraries for machine learning. The application includes all the necessary functions for image processing, feature extraction, and a human–computer interface to assist medical specialists in identifying patients most likely to have pathology. In addition, thanks to the block-based approach, the application also implements the capability to localize a nodule within the image.

6. CONCLUSION

This paper presents an approach to the analysis and classification of thyroid images aimed at assisting medical specialists in identifying patients who require priority medical care. To obtain data for Machine Learning we applied Haralick texture method and the local density function.

The research conducted demonstrated that for small and average samples the both methods give adequate features for network training and may be applied in medical decision-making systems.

7. ACKNOWLEDGMENTS

The authors would like to thank the N. I. Pirogov Clinic of High Medical Technologies for providing the image samples.

References

[1] R. M. Haralick, K. Shanmugam, I. Dinstein Textural features for image classification // IEEE Transactions on systems, man and cybernetics. 1973. Vol. SMCoC 3. № 6. P. 610-621.

[2] Y. Xu, Viewpoint Invariant Texture Description Using Fractal Analysis // International Journal of Computer Vision. — 2009. — T. 83, № 1. — C. 85-100.

[3] R. M. Haralick, Statistical and structural approaches to texture // Proceedings of the IEEE. 1979. Vol. 67, №.5. P. 786 – 804.

[4] N. I. Belov, M. A. Ermak, E. A. Dubinich, Yu. A. Kuznetsov Image recognition based on Haralick texture features and artificial neural networks. Scientific and Technical Journal of Information Technologies, Mechanics and Optics, 2022, Vol. 22, No. 2, pp. 279–286.

[5] N. B. Ampilova, I. P. Soloviev and V. A. Lyamin "Application of fractal methods to the analysis of biocrystal images," *Journal of Applied Electromagnetism*, vol. 25, no. 2, pp. 11–20, Dec. 2023.

[6] I. Soloviev Application of multifractal methods for the analysis of crystal structures // Journal of applied electromagnetism. -- 2022. -- T. 24. -- C. 21-26.

[7] F. Pedregosa, G. Varoquaux, A. Gramfort, (2011). Scikit-learn: Machine learning in Python. Journal of Machine Learning Research, 12, 2825–2830.

SIMULATION OF A LORA-BASED WEARABLE SYSTEM FOR MARITIME EMERGENCY TRACKING USING MATLAB

Nadezhda Vladimirova

Nikola Vaptsarov Naval Academy
73 Vasil Drumev Str., Varna, Bulgaria
Email: n.vladimirova@naval-acad.bg

Dilyana Dimitrova

Nikola Vaptsarov Naval Academy
73 Vasil Drumev Str., Varna, Bulgaria
Email: di.dimitrova@naval-acad.bg

Abstract

Maritime safety continues to face challenges, particularly during emergency situations involving crew members. This study presents a MATLAB-based simulation of a LoRa-enabled wearable emergency monitoring system designed for real-time tracking of sailors' vital signs and location. The system integrates health sensors, GPS modules, and SOS signaling into a compact wearable device, with data transmitted to a shipboard dashboard for live monitoring. The simulation results demonstrate reliable data transmission under realistic constraints, effective detection of physiological anomalies, and emergency alert generation. The findings confirm the feasibility and effectiveness of using low-power, long-range communication to enhance crew safety in maritime operations.

Keywords: LoRa, LoRa mesh, maritime safety, wearable monitoring system, MATLAB simulation, real-time tracking, emergency alert system, vital sign monitoring

1. INTRODUCTION

In maritime operations, ensuring the safety of crew members in emergency situations such as man-overboard (MOB) incidents remains a critical challenge. The main aim of this paper is to present a simulation of a LoRa-based wearable emergency tracking system designed for real-time sailor monitoring and SOS alert transmission. Using MATLAB, the paper presents a comprehensive system that includes wearable units equipped with GPS (Global Positioning System), heart rate (HR) monitoring, panic signalling capabilities, and communication with a shipboard transceiver. The system features real-time mapping, automated anomaly detection, and emergency logging. The simulation results demonstrate reliable performance in terms of range, transmission latency, and emergency response efficiency.

2. RELATED WORK

For the literature review, scientific papers indexed in the electronic database Scopus between 2020 and 2025 were analysed. A structured methodology was followed, including keyword-based search, filtering of relevant publications, extraction of essential content, and summarization of the findings. The following keywords were used: wearable system, MATLAB, sensor network, and simulation, resulting in a set of 10 closely related studies. An overview of the papers is presented in Table 1.

The literature review highlights the increasing interest in wearable systems and their applications across various domains, including healthcare and biomechanics. The use of MATLAB simulations and sensor networks in these studies underscores the importance of modelling and analysing complex systems to optimize performance and functionality. However, the integration of Long Range (LoRa) technology in wearable systems remains limited in maritime applications, indicating a potential area for further research and development. There is a notable absence of simulations specifically targeting maritime environments, highlighting a critical gap in the current research landscape. This underscores the importance of developing MATLAB-based simulations for wearable LoRa systems. Therefore, additional sources were examined to cover a broader scope of the topic.

Empirical studies have validated the applicability of LoRa technology in marine contexts. One experiment demonstrates a communication range of over 22 km across open sea with low-cost antennas, and distances up to 28 km in obstructed conditions using high-gain antennas [11]. Other trials have reported connectivity exceeding 110 km between sea-based nodes and shore-based gateways [12]. These findings highlight the potential of LoRa as a cost-effective and long-range communication technology for emergency maritime applications. The paper [13] introduces a real-world, LoRa-based tracking system specifically designed for lightweight boats operating in coastal ports. The system integrates GPS and environmental sensors on vessels, transmitting data via LoRa to a shore-side gateway. Simulating the LoRa-based emergency tracking system in MATLAB allows the exploration and evaluation of key deployment parameters. Such simulations offer a low-risk and cost-effective environment to assess performance metrics, providing information to practical design decisions before field deployment [14].

The proposed research topic is highly relevant. It aligns with contemporary needs for scalable, real-time, and energy-efficient solutions for marine safety. By utilizing simulation tools to explore design trade-offs, the study contributes to optimizing system parameters and guiding future real-world implementations.

TABLE 1. Summary of reviewed studies (2020–2025)

Source	Year	Application area	Tool/Algorithm	LoRa	Wearable
[1]	2025	WBAN routing	Hybrid IPSO + ACSO	No	Yes
[2]	2024	Medical antenna design	Ant Colony Optimization (ACO)	No	Yes
[3]	2024	Biomechanics (knee force prediction)	ML on IMU data	No	Yes
[4]	2024	Wearable energy harvesting	Hybrid MATLAB/Simulink + LTSpice with MPPT	No	Yes
[5]	2023	IoT data compression	Low-rank sparse deep compressed sensing via MATLAB simulations	No	No
[6]	2023	Textile-based wearable antennas	Microstrip patch with textile dielectric	No	Yes
[7]	2023	Vehicular wearable health systems	IoT + VANET, MATLAB/NetSim	No	Yes
[8]	2021	Exoskeleton control	RNN-optimized adaptive admittance control	No	Yes
[9]	2021	IoT healthcare routing	Dual-prediction model (EERP-DPM)	No	Yes
[10]	2020	Parkinson's detection	Heuristic tubu optimized SMNN (HTSMNN)	No	Yes

3. SYSTEM ARCHITECTURE

The system architecture builds upon the design in [15], enhanced with health sensors and a MATLAB-based dashboard for real-time monitoring (Fig. 1). It includes:

- Wearable device (bracelet) equipped with GPS for location tracking; HR, blood oxygen saturation (SpO_2), and temperature sensors for health monitoring; SOS button for emergencies, and a LoRa transceiver for low-power, long-range communication.
- Shipboard base station which receives LoRa packets, processes data, manages alerts, logs information, and updates the display in real time.
- MATLAB dashboard which displays live sailor locations on a satellite map, updates vital signs with color-coded status, triggers SOS alerts with sound, and visualizes historical health trends.

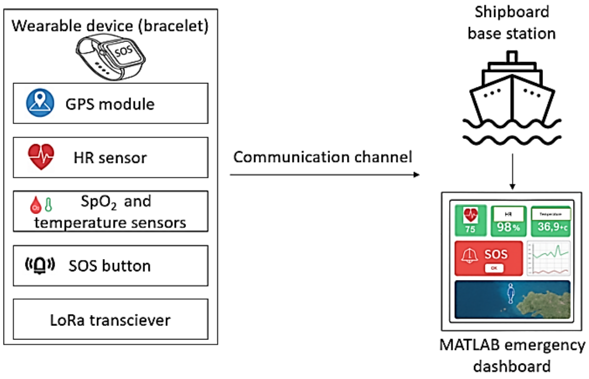

Figure 1. System architecture

4. SIMULATION ENVIRONMENT AND DATA GENERATION

The system simulates 10 sailors equipped with wearable bracelets. Each bracelet periodically generates synthetic data that includes heart rate, GPS coordinates, and an SOS alert flag. The simulation is implemented in MATLAB, selected for its powerful data processing and visualization capabilities.

At each simulation step, a new data packet is generated for each sailor. The packet may be dropped based on the configured loss probability. Received packets are processed and used to update the graphical dashboard. This allows for controlled testing of emergency response scenarios.

The system automatically classifies each reading into categories and raises alerts based on:

- HR > 140 bpm – high heart rate alert;
- HR < 55 bpm – low heart rate alert;
- $SpO_2 < 92\%$ – oxygen desaturation alert;
- Temp > 38.5°C or < 35°C – fever or hypothermia risk;
- SOS = TRUE – manual emergency flag.

Triggered alerts update the dashboard with visual indicators and popup windows, providing immediate situational awareness for on-board personnel. Each received data packet is classified as NORMAL or assigned an alert type. When an abnormal condition is detected, a visual alert is generated in the GUI (Graphical User Interface) using MATLAB's uialert function.

Table 2 presents the transmitted packets structure.

TABLE 2.

Format of transmitted packets from wearable devices in MATLAB

Field	Type	Description
ID	String	Sailor's name or unique ID
timestamp	DateTime	Time of reading
GPS	Float[2]	Latitude and longitude
heart_rate	Integer	Heart rate in beats per minute (bpm)
temperature	Float	Body temperature in °C
spo2	Float	Oxygen saturation level (%)
SOS	Boolean	1 if SOS is activated

The communication model is inspired by the LoRa physical layer, incorporating core features such as low-power periodic data transmission, GPS-based updates, and probabilistic packet loss modelling. The MATLAB simulation includes delayed transmission, packet dropout probability, and limited data rate per node, mimicking real-world LoRa constraints

5. MATLAB SIMULATION

To evaluate the functionality and performance of the proposed LoRa-based emergency monitoring system, a MATLAB simulation was developed. It models wearable devices for sailors, replicates real-time LoRa data transmission, tracks heart rate, GPS location, and SOS signals, generates health alerts, and visualizes data on a dashboard.

The MATLAB GUI consists of four dynamic sections:

- Heart Rate chart – displays real-time HR values for each sailor;
- Temperature chart – tracks core body temperature;
- SpO_2 chart – monitors oxygen saturation;
- GPS map – plots sailor positions with markers and labels.

Each sailor is color-coded consistently across all visualizations.

The MATLAB-based GUI dashboard was developed using:

- geoaxes() – for real-time map tracking;
- uicontrol() – for real-time text status updates;
- containers. Map – for dynamic variable tracking per sailor;
- msgbox() and beep for visual and audible SOS alerts.

The GUI processes packets as they are received, updates the live map with markers, and shows popup warnings for SOS or abnormal HR.

6. RESULTS FROM THE SIMULATION

A live satellite-based geospatial map (Fig. 2) displayed the real-time positions of all sailors within the Black Sea region. GPS coordinates were continuously updated and plotted, allowing monitoring of movement and location drift. The system maintained visual accuracy throughout the 30-cycle simulation. The map interface clearly indicated the location and status of each sailor.

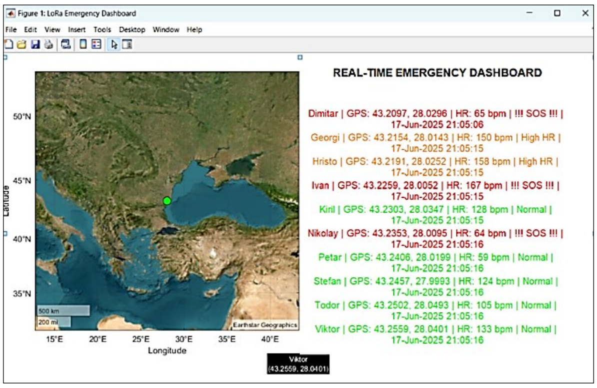

REAL-TIME EMERGENCY DASHBOARD

```
Dimitar | GPS: 43.2097, 28.0296 | HR: 65 bpm | !!! SOS !!! |
17-Jun-2025 21:05:06
Georgi | GPS: 43.2154, 28.0143 | HR: 150 bpm | High HR |
17-Jun-2025 21:05:15
Hristo | GPS: 43.2191, 28.0252 | HR: 158 bpm | High HR |
17-Jun-2025 21:05:15
Ivan | GPS: 43.2259, 28.0052 | HR: 167 bpm | !!! SOS !!! |
17-Jun-2025 21:05:15
Kiril | GPS: 43.2303, 28.0347 | HR: 128 bpm | Normal |
17-Jun-2025 21:05:15
Nikolay | GPS: 43.2353, 28.0095 | HR: 64 bpm | !!! SOS !!! |
17-Jun-2025 21:05:16
Petar | GPS: 43.2406, 28.0199 | HR: 59 bpm | Normal |
17-Jun-2025 21:05:16
Stefan | GPS: 43.2457, 27.9993 | HR: 124 bpm | Normal |
17-Jun-2025 21:05:16
Todor | GPS: 43.2502, 28.0493 | HR: 105 bpm | Normal |
17-Jun-2025 21:05:16
Viktor | GPS: 43.2559, 28.0401 | HR: 133 bpm | Normal |
17-Jun-2025 21:05:16
```

Figure 2. Live map display of sailor position with status indicators on the system dashboard

The dashboard visualized vital signs with a color-coded scheme: green for normal ranges, orange for elevated but non-critical, and red for critical readings or SOS activation. This intuitive representation enabled rapid assessment of crew health. Several high heart rate events (e.g., >150 bpm) were detected and flagged (Fig. 2, right panel).

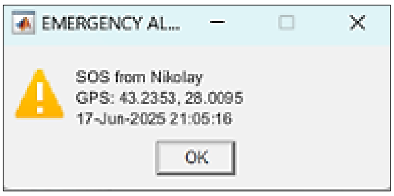

SOS from Nikolay
GPS: 43.2353, 28.0095
17-Jun-2025 21:05:16

Figure 3. SOS alert window

The system’s emergency response logic was validated through multiple simulated SOS events. For example, sailors Ivan, Dimitar, and Nikolay triggered SOS signals, resulting in instantaneous pop-up alert windows (Fig. 3) combined with audible warning cues. Each alert included the sailor's ID, timestamp, and exact GPS coordinates, facilitating rapid decision-making and location-specific response.

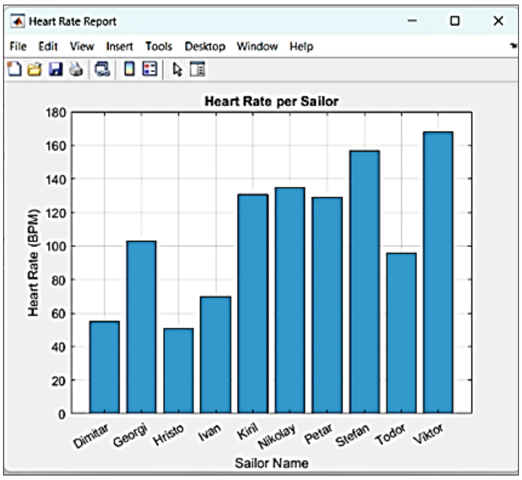

Figure 4. Heart rate trends per sailor

A dedicated panel displayed historical trends and comparative statistics. As shown in Fig. 4, individual heart rate values were plotted separately for each sailor, highlighting both normal and outlier physiological responses. These plots enabled retrospective health trend analysis and data-driven performance evaluation of the wearable monitoring system’s performance.

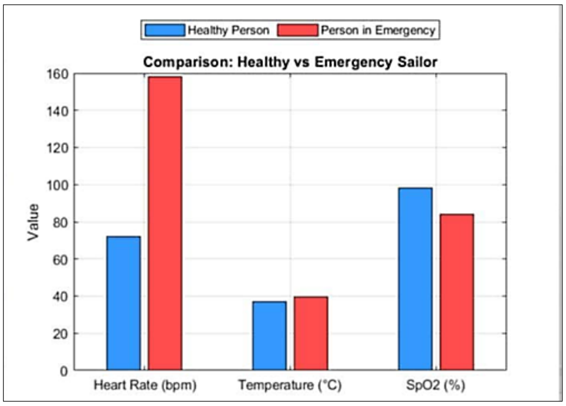

Figure 5. Healthy vs emergency vital signs

To further evaluate the system responsiveness and data differentiation, a comparative diagram was used to contrast the healthy and emergency-status sailors (Fig. 5), presenting key physiological parameters including heart rate, SpO_2 levels, and body temperature.

Sailors in the emergency category presented significantly elevated heart rates (often exceeding 150 bpm), reduced SpO_2 values below the typical 95% threshold, and activated SOS flags, while healthy sailors maintained stable, medically acceptable readings. The visual distinction demonstrates the system’s ability to categorize and display health status in real time.

This side-by-side comparison validates sensor inputs and system logic and supports future developments in predictive health assessment and early detection of physiological or location anomalies in maritime environments. The simulation confirmed the feasibility of real-time monitoring of health and location data over a LoRa channel. Integrating geospatial visualization, physiological signal analysis, emergency handling, and historical data review into a single MATLAB dashboard illustrates the system’s potential for enhancing maritime safety protocols.

7. CONCLUSION

This study presented a MATLAB-based simulation of a LoRa-enabled wearable emergency monitoring system developed for maritime safety applications. The proposed architecture integrates GPS tracking, real-time vital sign monitoring, SOS signaling, and a shipboard GUI dashboard. The simulation results demonstrated the system's ability to reliably transmit physiological and location data under realistic LoRa constraints, while supporting anomaly detection and emergency alerts. Real-time geospatial mapping, health trend visualization, and audible/visual alert mechanisms were validated across 10 virtual sailor units over multiple simulation cycles. The comparative analysis of healthy versus emergency cases confirmed the system's diagnostic potential. These findings support the feasibility of deploying low-power, long-range wearable solutions for crew safety in maritime environments and provide valuable insights for future real-world implementation and optimization.

ACKNOWLEDGEMENT

This research is supported by the Bulgarian Ministry of Education and Science under the National Program "Young Scientists and Postdoctoral Students - 2".

References

[1] N. Dhamaraj, G. Jeevananth, K. N. Kumar, N. S. Kannan, C. S. R. Keerthi, and B. S. Ramanan, "Optimized Cluster Head Selection and Routing in WBANS Using Hybrid Improved Particle Swarm and Adaptive Cuckoo Search Algorithm," in 2025 IEEE 1st International Conference on Smart and Sustainable Developments in Electrical Engineering, SSDEE 2025, Dhanbad: Institute of Electrical and Electronics Engineers Inc., 2025. doi: 10.1109/SSDEE64538.2025.10968216.

[2] D. S. Mahesh and K. B. Naveen, "Metaheuristic (Ant Colony Optimization) Algorithm-Based Optimization of a Circular Shaped Patch Antenna for Medical Purposes," SN Comput Sci, vol. 5, no. 7, Oct. 2024, doi: 10.1007/s42979-024-03273-7.

[3] M. Ajdaroski, S. Y. Baek, J. A. Ashton-Miller, and A. O. Esquivel, "Predicting Leg Forces and Knee Moments Using Inertial Measurement Units: An In Vitro Study," J Biomech Eng, vol. 146, no. 2, Feb. 2024, doi: 10.1115/1.4064145.

[4] N. Bangari, V. K. Singh, and V. K. Sharma, "Experimental investigation of thin-film solar cells as a wearable power source," Energy Sources, Part A: Recovery, Utilization and Environmental Effects, vol. 46, no. 1, pp. 9341–9361, Jan. 2024, doi: 10.1080/15567036.2020.1776794.

[5] H. Rajoriya and R. Sadiwala, "Deep compressive sensing and reconstruction algorithm in wireless Internet of Things," Journal of Integrated Science and Technology, vol. 11, no. 2, p. 487, Jan. 2023, Accessed: Jun. 21, 2025.

[6] C. V. Mahamuni, "Design and Simulation of Microstrip Patch Antennas with Textile Dielectrics for Body Sensor Networks (BSNs) and Wearable IoT Applications," Lecture Notes in Electrical Engineering, vol. 1056, pp. 511–522, Jan. 2023, doi: 10.1007/978-981-99-3656-4_52.

[7] K. Kaur and H. K. Verma, "IoV-Health: an intelligent integrated emergency health monitoring and alert generation system," Soft comput, 2023, doi: 10.1007/s00500-023-08251-4.

[8] P. Lian, Y. He, Y. Ma, J. Liu, and X. Wu, "Adaptive admittance control of human-exoskeleton system using RNN optimization," 2021 IEEE International Conference on Real-Time Computing and Robotics, RCAR 2021, pp. 584–589, Jul. 2021, doi: 10.1109/RCAR52367.2021.9517398.

[9] F. A. Almalki, S. Ben Othman, F. A. Almalki, and H. Sakli, "EERP-DPM: Energy Efficient Routing Protocol Using Dual Prediction Model for Healthcare Using IoT," J Healthc Eng, vol. 2021, p. 9988038, Jan. 2021, doi: 10.1155/2021/9988038.

[10] A. A. AlZubi, A. Alarifi, and M. Al-Maitah, "Deep brain simulation wearable IoT sensor device based Parkinson brain disorder detection using heuristic tubu optimized sequence modular neural network," Measurement (Lond), vol. 161, p. 107887, Sep. 2020, doi: 10.1016/j.measurement.2020.107887.

[11] N. Jovalekic, V. Drndarevic, E. Pietrosemoli, I. Darby, and M. Zennaro, "Experimental Study of LoRa Transmission over Seawater," Sensors, vol. 18, no. 9, p. 2853, Aug. 2018, doi: 10.3390/S18092853.

[12] S. Pensieri et al., "Evaluating LoRaWAN Connectivity in a Marine Scenario," Journal of Marine Science and Engineering 2021, Vol. 9, Page 1218, vol. 9, no. 11, p. 1218, Nov. 2021, doi: 10.3390/JMSE9111218.

[13] R. Sanchez-Iborra, I. G. Liaño, C. Simoes, E. Couñago, and A. F. Skarmeta, "Tracking and Monitoring System Based on LoRa Technology for Lightweight Boats," Electronics 2019, Vol. 8, Page 15, vol. 8, no. 1, Dec. 2018, doi: 10.3390/ELECTRONICS8010015.

[14] A. Pozzebon, I. Cappelli, F. Campagnaro, R. Francescon, and M. Zorzi, "LoRaWAN Transmissions in Salt Water for Superficial Marine Sensor Networking: Laboratory and Field Tests," Sensors 2023, vol. 23, no. 10, May 2023, doi: 10.3390/s23104726

[15] D. Dimitrova and N. Vladimirova, "Design of LoRa-integrated wearable system for sailor tracking in maritime emergencies," in Proc. 19th Int. Eng. Conf. on Communications, Electromagnetics and Medical Applications (CEMA '25), to be published.

DESIGN OF LoRa-INTEGRATED WEARABLE SYSTEM FOR SAILOR TRACKING IN MARITIME EMERGENCIES

Dilyana Dimitrova

Nikola Vaptsarov Naval Academy
73 Vasil Drumev Str., Varna, Bulgaria
Email: di.dimitrova@naval-acad.bg

Nadezhda Vladimirova

Nikola Vaptsarov Naval Academy
73 Vasil Drumev Str., Varna, Bulgaria
Email: n.vladimirova@naval-acad.bg

Abstract

This paper addresses the critical issue of crew safety during maritime emergencies by presenting a wearable system for real-time sailor tracking and emergency signaling. The proposed solution integrates a wearable unit with a shipboard transceiver using a mesh-based LoRa communication network, ensuring long-range, low-power data transmission without reliance on existing infrastructure. The system design includes automated distress activation via water immersion sensors and manual panic buttons, as well as continuous location tracking. Through a systematic review of current literature and the development of a system architecture, the study demonstrates the novelty and practicality of the proposed approach. The results indicate a significant potential to improve situational awareness, reduce response times, and enhance overall marine safety.

Keywords: LoRa mesh topology, mesh networks, wearable devices, sailor tracking, bracelet-based monitoring, system design

1. INTRODUCTION

Maritime operations inherently involve high-risk environments, where emergency situations, such as man-overboard incidents, can quickly escalate into life-threatening events. Ensuring the safety of people at sea remains a critical concern for naval forces, commercial fleets, and research vessels. Traditional emergency response systems often rely on manual detection and centralized infrastructure, which may delay response times or fail entirely in harsh or infrastructure-less environments.

In recent years, the integration of Internet of Things (IoT) technologies and low-power communication protocols has opened new possibilities for real-time monitoring and emergency response at sea. Among these, LoRa (Long Range) wireless technology has emerged as a promising solution due to its long-range coverage, low energy consumption, and robustness in remote or obstructed environments. When combined with mesh networking topologies, LoRa can enable decentralized, resilient communication networks capable of operating without fixed infrastructure.

The main aim of this study is to propose the design and architecture of a LoRa-integrated wearable system for real-time tracking and emergency alerting of sailors in maritime environments. The system utilizes the low-power, long-range communication capabilities of LoRa technology, combined with GPS positioning, water immersion detection, and manual SOS signalling, to enhance crew safety, situational awareness, and response efficiency during overboard or high-risk incidents. The design emphasizes mesh network communication for improved reliability and autonomy, particularly in infrastructure-less maritime zones.

2. RELATED WORK

For the literature review, scientific papers and reports published between 2020 and 2025 were examined, indexed in the electronic database Scopus. The review followed a systematic process, including literature search, selection of relevant publications, extraction of key information, and summarization of findings.

The search criteria in Scopus included the keywords: “LoRa” and “bracelet”. Only 3 publications matching them were found. In paper [1], the authors analyse the impact of a replay attack on LoRaWAN wearable devices by demonstrating how insecure configurations can compromise message reliability and examining changes observed at the

LoRaWAN gateway during the attack. The study [2] presents the design and evaluation of the HELPi system - a LoRa-based digital bracelet for supporting indigents - by identifying user needs, proposing a dynamic communication protocol, and assessing user perceptions, signal propagation, and energy consumption to inform system deployment. In [3] authors explore a hybrid approach combining IoT, wireless healthcare networks, and cloud computing to enable early identification, monitoring, and exposure alerts for COVID-19, emphasizing intelligent diagnosis and social distancing through federated medical data systems.

Due to the limited availability of sources on the selected topic in Scopus, with only three relevant publications identified, additional literature was retrieved from other databases to support the study comprehensively. Paper [4] presents a system designed for automatic man-overboard detection and location tracking using LoRa communication. The system includes a wearable terminal that activates upon water immersion, transmitting GPS data to a ship-mounted base station. It demonstrates the application of LoRa in maritime emergency scenarios with a focus on wearable devices. In [5] authors introduce a wearable IoT system combining LoRa and BLE (Bluetooth Low Energy) technologies for emergency communication in infrastructure-less scenarios, highlighting the integration of LoRa in wearable emergency systems, emphasizing communication protocols and user localization. The paper [6] presents an ad-hoc communication system utilizing LoRa for maritime applications, enabling peer-to-peer communication without relying on traditional network infrastructure.

TABLE 1.
Comparison of relevant literature sources

Source	Year	Description	Relevance to the topic
22	2024	LoRa-based ad hoc maritime network.	Focuses on maritime LoRa communication.
[4]	2023	LoRa-based maritime emergency beacon with GPS for overboard alerts.	Wearable, GPS, marine environment.
[7]	2021	Affordable LoRa GPS beacon for maritime emergencies.	Shows LoRa + GPS for maritime distress, low-cost angle.
[5]	2020	LoRa + BLE system for emergency communication and user localization.	Multi-hop wearable emergency system.

The literature review and the comparison in Table 1 show that several studies and projects are relevant to the topic. However, none specifically describes a LoRa-enabled emergency bracelet for sailors with real-time tracking and distress signaling. This highlights a clear gap in current research and establishes the novelty of the proposed system.

The development of such a system can significantly contribute to improving situational awareness, rescue efficiency, and crew safety during maritime disasters, representing a critical advancement in the domain of wearable maritime safety technologies.

3. LoRa-BASED COMMUNICATION TECHNOLOGIES

LoRa is a low-power, wide-area network (LPWAN) communication technology designed for long-range data transmission with minimal energy consumption. It operates in unlicensed ISM (Industrial, Scientific, and Medical) bands (such as 433 MHz, 868 MHz, and 915 MHz) and utilizes a modulation technique known as Chirp Spread Spectrum (CSS), which enables devices to communicate over distances of several kilometers while maintaining robustness against interference and noise. These characteristics make LoRa suitable for use in challenging environments, such as maritime operations, where reliable communication is essential [8].

LoRa mesh refers to a network architecture built on top of the LoRa physical layer, where devices (or nodes) communicate with one another and forward messages across the network. This enables information to travel through multiple “hops” rather than requiring a direct link to the destination. LoRa Mesh features self-organizing and adaptable structure, multi-hop communication, flexible device placement in the field, and provides redundancy that improves reliability in case of node failures [9]. Because of these advantages, it is suitable for scenarios where traditional infrastructure is unavailable or damaged, such as during natural disasters or at sea. In maritime safety applications, LoRa mesh enables the deployment of wearable tracking and emergency signaling devices that can operate reliably without frequent maintenance or charging.

LoRaWAN (Long Range Wide Area Network) is a standardized communication protocol designed to work over the LoRa physical layer. It uses a star-of-stars network layout where devices send data to a central gateway, which then forwards it to a cloud-based server. LoRaWAN is designed to be secure, energy-efficient, and capable of supporting large networks of devices. It has centralized architecture for broad and scalable coverage. It is commonly used in smart city infrastructure, industrial IoT, and utility monitoring, where reliable connectivity and central data collection are important [10].

When designing LoRa-based wearable systems the choice of communication method has a major impact on system performance. Point-to-point LoRa works well for simple, short-range links where only a few devices need to communicate. LoRa mesh offers better range and reliability without needing fixed infrastructure, making it more suitable for emergency scenarios or remote areas. LoRaWAN is ideal for centralized systems that connect to the internet, but may not be practical in isolated environments with no access to gateway infrastructure [11].

The use of open-source protocols such as Meshtastic extends the capabilities of standard LoRa networks by introducing mesh networking functionality. This allows data to be forwarded across multiple devices in a decentralized manner, enhancing coverage, resilience, and reliability in environments where line-of-sight transmission cannot always be guaranteed. As a result, LoRa-based communication technologies represent a powerful solution for enabling low-cost, long-range, and energy-efficient communication in emergency and tracking systems adapted to the maritime domain.

Based on the presented technologies, a suitable solution for sailor tracking in maritime emergencies is LoRa mesh. This is the topology used for the proposed system.

4. DESIGN AND ARCHITECTURE OF LoRa-INTEGRATED WEARABLE SYSTEM

4.1. System design

The proposed system is designed to enhance the safety of sailors during maritime emergencies by integrating a wearable LoRa-based communication unit (bracelet) with onboard transceiver system and maritime communication systems. The primary design objectives are real-time location tracking, immediate distress signaling, and reliable communication coverage, even in infrastructure-less or signal-deprived areas. The design of the LoRa mesh network is shown on Fig. 1.

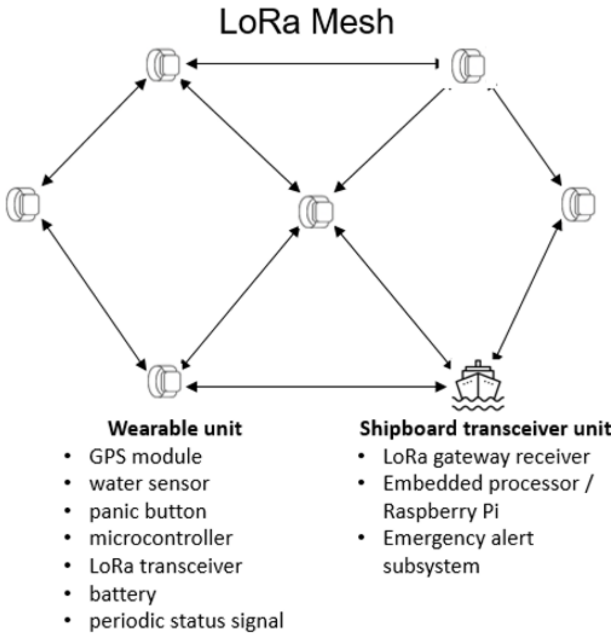

Figure 1. Design of the LoRa mesh network

4.1.1. Wearable unit

The wearable device is compact, waterproof, and designed to be comfortably worn by sailors. It includes the following core components:

- **GPS module** - continuously determines and updates the sailor's location with high precision.
- **Water sensor** - automatically detects water immersion. When triggered, it initiates a man-overboard (MOB) emergency alert without requiring user intervention.
- **Panic button** - allows the sailor to manually trigger an emergency alert.
- **Microcontroller** - acts as the central processing unit to manage data collection and communication logic.
- **LoRa transceiver -** ensures low-power, long-range wireless communication. It supports both peer-to-peer and mesh topologies, ensuring reliable message delivery in dynamic and infrastructure-less environments.

- **Battery** - provides sufficient power for long-duration operation; includes power-saving strategies for extended battery life.
- **Periodic status signal** ("I'm OK") - the authors propose that device is programmed to transmit a periodic signal (e.g., every 5 minutes) confirming the sailor's safety and system functionality. If it's not received within the set timeframe, the system treats it as a possible emergency and can initiate a secondary check or alert.

4.1.2. LoRa communication network

The system utilizes LoRa (Long Range) wireless technology for its low-power, long-range communication capabilities. A mesh network topology - enabled by platforms like Meshtastic - is proposed to ensure resilience and extended coverage, allowing devices to relay data between one another until it reaches the shipboard transceiver. This model reduces dependence on centralized infrastructure and enhances system's reliability during disasters.

4.1.3. Shipboard transceiver unit

The authors propose that the shipboard-based system acts as the primary receiver and emergency management hub. It includes:

- **LoRa gateway module -** constantly listens for incoming transmissions from all wearable devices in the area, including normal status updates and emergency signals.
- **Embedded processor** - interprets data, logs sailor locations, monitors periodic check-ins, and processes SOS or MOB events in real time.
- **Emergency alert subsystem** - when an SOS or missed "OK" signal is detected, the system should generate visual/audible alerts on the dashboard and displays the last known coordinates of the affected sailor. It could also forward data to integrated systems like AIS, GMDSS, or mobile apps for further action.

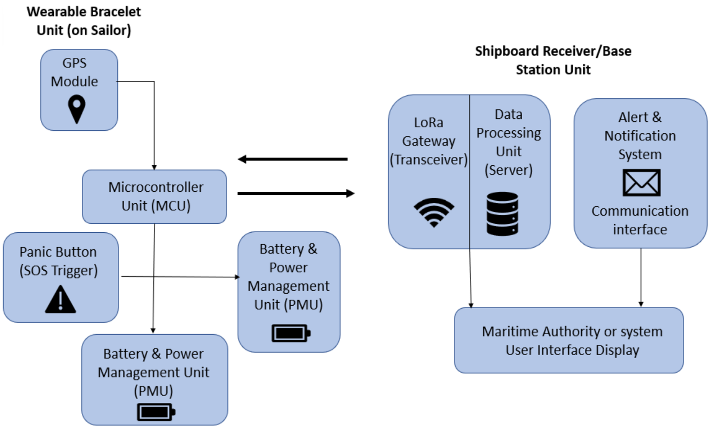

Figure 2. Design of the proposed system

4.2. Operational workflow

The design of the proposed system is shown on Fig. 2. The bracelet continuously transmits position data via LoRa mesh. The operational workflow is as follows:

1. In an emergency (water immersion or panic button), the system sends a high-priority distress packet.
2. The onboard transceiver decodes the packet and identifies the location and identity of the affected sailor.
3. The alert is forwarded to relevant maritime authorities or systems via integrated communication channels.

5. CONCLUSION

This study presents a novel LoRa-based wearable emergency system designed specifically for maritime applications, addressing a critical gap in existing research and technologies. The literature review highlights the limited number of studies directly focused on LoRa-enabled bracelets for sailor safety, underscoring the originality and potential impact of the proposed system.

The designed solution addresses the critical need for real-time monitoring and emergency signaling for sailors during overboard or high-risk situations. By utilizing LoRa communication technology, the system ensures long-range, low-power data transmission, enabling resilient communication even in infrastructure-less or remote maritime zones.

Through careful selection of components and architecture, the system is designed to improve situational awareness and response times during overboard incidents. The incorporation of periodic "I'm OK" signals adds an additional safety layer, helping to proactively identify unresponsive or compromised devices.

The proposed design represents a significant contribution to the field of maritime safety, with potential for deployment in various operational contexts to enhance crew protection, optimize rescue operations, and reduce fatalities in marine emergencies.

Future work includes hardware realization of the proposed design, field testing under varying marine conditions, optimization of power consumption strategies, and integration with international maritime distress systems.

ACKNOWLEDGMENTS

This research is supported by the Bulgarian Ministry of Education and Science under the National Program "Young Scientists and Postdoctoral Students – 2".

References

[1] T. Perkovic, J. Sabic, K. Zovko, and P. Solic, "An Investigation of a Replay Attack on LoRaWAN Wearable Devices," 2023 IEEE International Mediterranean Conference on Communications and Networking, MeditCom 2023, pp. 45–49, Jan. 2023, doi: 10.1109/MeditCom58224.2023.10266648.

[2] Á. G. Andrade, J. M. Ramírez, and M. D. Rodríguez, "Informing the design of a LoRa™-based digital bracelet for the timely assistance of indigents," J Ambient Intell Humaniz Comput, vol. 13, no. 11, pp. 5335–5350, Nov. 2022, doi: 10.1007/s12652-020-01732-6.

[3] K. Zouari, O. Houmanat, I. Cherti, and M. Bahaj, "Design of an Intelligent Bracelet Based on IOT and LORA Protocol to Identify New COVID-19 Contact Cases," Proceedings – 2021 International Conference on Digital Age and Technological Advances for Sustainable Development, ICDATA 2021, pp. 201–207, Jun. 2021, doi: 10.1109/ICDATA52997.2021.00047.

[4] Z. Li, J. Dai, Y. Luan, N. Sun, and L. Du, "LR-MPIBS: A LoRa-Based Maritime Position-Indicating Beacon System," Applied Sciences 2024, Vol. 14, Page 1231, vol. 14, no. 3, p. 1231, Feb. 2024, doi: 10.3390/APP14031231.

[5] L. Sciullo, A. Trotta, and M. Di Felice, "Design and performance evaluation of a LoRa-based mobile emergency management system (LOCATE)," Ad Hoc Networks, vol. 96, p. 101993, Jan. 2020, doi: 10.1016/J.ADHOC.2019.101993.

[6] J. Zhang, H. Liu, Y. He, W. Gao, N. Xu, and C. Liu, "MCLORA: Maritime ad-hoc communication system based on LORA," High-Confidence Computing, p. 100275, Oct. 2024, doi: 10.1016/J.HCC.2024.100275.

[7] The James Dyson Award, "SafeSEA the affordable emergency GPS | James Dyson Award." Accessed: May 29, 2025. [Online]. Available: https://web.archive.org/web/20250529073404/https://www.jamesdysonaward.org/en-US/2021/project/safesea-the-affordable-emergency-gps.

[8] Semtech, "Semtech LoRa Technology Overview." Accessed: Jun. 10, 2025. [Online]. Available: https://web.archive.org/web/20250602160031/https://www.semtech.com/lora.

[9] H. Huh and J. Y. Kim, "LoRa-based Mesh Network for IoT Applications," IEEE 5th World Forum on Internet of Things, WF-IoT 2019 – Conference Proceedings, pp. 524–527, Apr. 2019, doi: 10.1109/WF-IOT.2019.8767242.

[10] LoRa Alliance, "About LoRaWAN." Accessed: Jun. 13, 2025. [Online]. Available: https://web.archive.org/web/20250606012356/https://lora-alliance.org/about-lorawan/.

[11] L. Xia et al., "Comparative study of LoRa-based communication protocols," Journal of Wireless Networks, vol. 28, no. 3, pp. 1123–1137, 2022.

MEASUREMENTS AND PATH LOSS MODELS AT 30 AND 300 MHZ OVER FLAT TERRAIN SCENARIOS

Nektarios Moraitis(1), Panayiotis Frangos(1), Ileana Popescu(1), Alexandros Rogaris(1)
and Seil Sautbekov(2)

(1) School of Electrical and Computing Engineering, National Technical University of Athens (NTUA),
9, Iroon Polytechniou Str., 157 73 Zografou, Athens, Greece
Tel. : +30 210 772 3694; e-mail : pfrangos@central.ntua.gr

(2) Department of Physics and Technology, Al-Farabi Kazakh National University
Almaty, Kazakshtan
e-mail : sautbek@mail.ru

Abstract

In this paper an outdoor measurement campaign for almost flat terrain environment is undertaken for wireless mobile applications at the frequencies of 30 MHz and 300 MHz. The measured results are compared here both with the well – known in the literature "Two–Ray" (TR) model of wave propagation, as well as with the also well – known "Extended Hata" (EH) and "Egli" empirical models. The results showed that TR model forecasts path loss with better accuracy, delivering low error metrics. It outperforms Extended Hata and Egli models, which proved to be unsuitable for predicting path loss in the specific examined scenario.

It is intended that further research by our research group will be conducted in the direction of comparison of our measured results with alternative analytical results, which have been produced by us in previous publications of ours, in this "low frequency" regime.

1. INTRODUCTION

The problem of electromagnetic (EM) wave propagation over a flat terrain (or over a lossy medium with flat interface) is well – known in the literature as the *"Sommerfeld antenna radiation problem"*, where the interest here is for observation points over the flat interface [1-23]. However, in this paper we concentrate in comparing our outdoor experimental measurements in "low frequency" regime (here for frequencies 30 MHz and 300 MHz), which are obtained here by our research group, with approximate or empirical models of electromagnetic (EM) wave propagation [24-30]. In near future proposed research by our group, we intend to compare our outdoor experimental results measured by us here with alternative analytical results which have been produced by our research group in previous publications of ours (also in the "low frequency" regime, at which *surface waves* are expected to be present).

The rest of this paper is organized as follows: Section 2 describes the measurement environment, the equipment, as well as the procedure followed during our outdoor experimental campaign. In Section 3, different models are introduced and assessed for their suitability to forecast the measured path loss. Finally, interesting conclusions and future research are presented in Section 4.

2. EXPERIMENTAL CAMPAIGN

The measurements were carried out in a flat road inside our University (NTUA) campus, in order to represent a near flat earth scenario. Fig. 1(a) and Fig. 1(b), illustrate the measurement environment, as well as the location of the transmitter (Tx). The <u>*blue line*</u> indicates the trajectory of the receiver (Rx) at 30 MHz, along which, the electric field values were recorded from 2 m up to 100 m in steps of 2 m. In respect, the <u>*red line*</u> stands for the 300 MHz measurements, where the electric field values were recorded from 2 m up to 300 m in steps of 2 m. Both sides of the road were surrounded by tall trees. The <u>*yellow star*</u> denotes the location of the Tx, which transmitted a continuous wave (CW) signal at 30 MHz and 300 MHz, for the first and second low frequency regime scenarios, respectively. In total, 50 and 150 received signal power samples were recorded at 30 and 300 MHz, respectively. At each measurement position the Rx was stationary, having a line-of-sight (LOS) condition with the Tx.

The Tx antenna was mounted at a height of 3 m about the road surface. A signal generator was employed to produce the transmitted signal, which was fed, through a 3-m cable, to a *vertically polarized* omnidirectional antenna (Skycan 25-2000 MHz), with a half power beamwidth (HPBW) of 60° in the elevation plane and a constant gain of about -25 dBi and 0 dBi, in the azimuth plane, at 30 MHz and 300 MHz, respectively. The transmitted effective isotropic radiated power (e.i.r.p.), was 20 dBm at both selected frequencies.

(a)

(b)

Figure 1. Measurement environment

An SRM-3006 frequency selective field meter by Narda GmbH (Pfullingen, Germany) in spectrum analysis mode was employed as the receiving unit. An electric field isotropic probe was used (27 MHz - 3 GHz with a 0 dBi gain), connected to the main control unit through a 1.5-m cable. The Rx sensor was mounted on a wooden tripod at 1.7 m above the field surface. The Rx unit recorded the power samples in dBV/m, using a time average of 2 minutes. The utilized Rx equipment was calibrated according to the ISO/IEC 17025:2017 standard [24]. Table I summarizes the Tx and Rx characteristics adopted in the launched measurement campaign.

TABLE I.
Transmitter and receiver characteristics during the measurement campaign at each selected frequency scenario

	30 MHz	**300 MHz**
Tx power	20 dBm	20 dBm
Tx gain	-25 dBi	0 dBi
EIRP	-5 dBm	20 dBm
Rx gain	0 dBi	
Rx sensitivity	-65 dBm	

Based on the received signal power the measured path loss *PL*, in decibels, at each Rx location can be calculated by:

$$PL = \mathrm{P}_{\mathrm{Tx}} + G_{\mathrm{Tx}} + G_{\mathrm{Rx}} - P_r \qquad (1)$$

where P_{Tx} indicates the Tx power in dBm, G_{Tx}, G_{Rx} denotes the Tx and Rx gains, respectively, in dBi, and P_r stands for the received signal power in dBm. Therefore, from (1), 50 and 150 path loss samples are resolved at each examined frequency scenario at a specific distance d_D, in meters, between Tx and Rx (length of the direct ray) that is given by:

$$d_D = \sqrt{d^2 + (h_t - h_r)^2} \qquad (2)$$

where d designates the direct horizontal (ground) distance, in meters, between Tx and Rx, and h_t, h_r designate the Tx and Rx heights (3 and 1.7 m), respectively.

The raw data for both scenarios are shown in Fig. 2, where the received power versus distance is depicted. It should be pointed out that the distance from Tx, in meters, represents the direct distance (d_D) between Tx and Rx.

In Section 3, below, the measured path loss, from eq. (1) above, will be compared with the flat terrain model ('two – ray model'), as well as with two empirical models for comparison purposes, which are the 'Extended Hata model' and 'Egli model'.

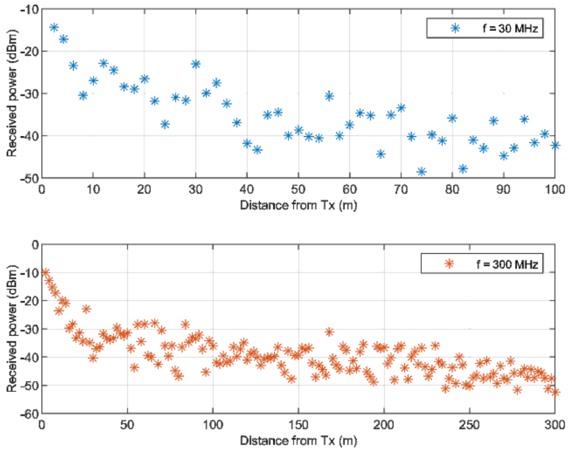

Figure 2. Received signal power at each measured scenario at 30 and 300 MHz

3. PATH LOSS MODELS, RESULTS AND DISCUSSION

The '*two-ray model*' describes the signal propagation using two components. The direct ray between Tx and Rx and a ground reflected path ray. The path loss, in decibels, based on the two-ray model is given by [25]:

$$PL = 20\log_{10}\left(\frac{4\pi d}{\lambda}\right) - 20\log_{10}\left|1 + \Gamma_{\mathrm{V}}\, e^{j\Delta\varphi}\right| \quad (3)$$

where λ is the wavelength, in meters, at each selected frequency, and d is the ground (horizontal) distance between Tx and Rx, as previously mentioned. Furthermore, Γ_{V} denotes the vertical polarization reflection coefficient of the ground reflected path, and $\Delta\varphi$ stands for the phase difference between the direct and the ground paths. The reflection coefficient is described by:

$$\Gamma_{\mathrm{V}} = \frac{-\varepsilon_r \sin\theta_i + \sqrt{\varepsilon_r - (\cos\theta_i)^2}}{\varepsilon_r \sin\theta_i + \sqrt{\varepsilon_r - (\cos\theta_i)^2}} \quad (4)$$

where θ_i, is the *"grazing angle"* of the incident wave (i.e., the angle between the incident EM wave and the flat terrain), and ε_r is the relative permittivity of the ground. Assuming a very dry ground, $\varepsilon_r = 3$ according to [26]. Furthermore, the grazing angle in (4), is related to the geometrical propagation characteristics according to:

$$\sin\theta_i = \left(\frac{h_t + h_r}{d_G}\right), \qquad \cos\theta_i = \left(\frac{d}{d_G}\right) \quad (5)$$

where d_G denotes the length of the ground reflected ray, in meters, which can be calculated by:

$$d_G = \sqrt{d^2 + (h_t + h_r)^2} \quad (6)$$

Finally, the phase difference between of the path lengths between the direct and the ground reflected rays are given by:

$$\Delta\varphi = \frac{2\pi}{\lambda}(d_D - d_G) \quad (7)$$

where d_D and d_G are provided by (2) and (6), respectively.

Apart from the two-ray path loss model, the measured path loss is also compared with the *"Extended Hata"* model [27]. The specific model is widely used and is applicable for frequencies up to 3 GHz, and distances up to 40 km. A rural/open area environment is assumed in this case; therefore, the path loss is given by:

$$\begin{aligned} PL = {} & PL_U - 4.78(\log_{10}[\min\{\max\{150, f\}, 2000\}])^2 \\ & + 18.33\log_{10}[\min\{\max\{150, f\}, 2000\}] - 40.94 \end{aligned} \quad (8)$$

where f is the operating frequency in MHz, and PL_U the path loss considering the urban environment. The latter parameter for frequencies between below 150 MHz can be calculated according to:

$$\begin{aligned} PL_U = {} & 69.6 + 26.2\log_{10}(150) - 20\log_{10}(150/f) \\ & - 13.82\log_{10}(\max\{30, h_t\}) \\ & + (44.9 - 6.55\log_{10}(\max\{30, h_t\}))\log_{10}(d_D) - a(h_r) - b(h_t) \end{aligned} \quad (9)$$

where d_D is the direct ray distance, converted in kilometres, between Tx and Rx, and f the operating frequency in MHz. Further, $a(h_r)$ and $b(h_t)$, are the correction factors for the Rx and Tx, respectively, taking into account their specific heights h_r and h_t in meters. The correction factors are adopted for the rural/open area locations and can be calculated by:

$$b(h_t) = \min\{0, 20\log_{10}(h_t/30)\} \quad (10)$$

and

$$\begin{aligned} a(h_r) = {} & (1.1\log_{10}(f) - 0.7)\min\{10, h_r\} \\ & - (1.56\log_{10}(f) - 0.8) + \max\{0, 20\log_{10}(h_r/10)\} \end{aligned} \quad (11)$$

For frequencies between 150 and 1500 MHz, the path loss is expressed as:

$$\begin{aligned} PL_U = {} & 69.6 + 26.2\log_{10}(f) - 13.82\log_{10}(\max\{30, h_t\}) \\ & + (44.9 - 6.55\log_{10}(\max\{30, h_t\}))\log_{10}(d_D) - a(h_r) - b(h_t) \end{aligned} \quad (12)$$

Therefore, the *"Extended Hata"* model calculates differently the path loss at 30 and 300 MHz, leveraging (9) and (12), espectively. Finally, *"Egli"* model [28], is also popular and utilized in forecasting path loss over terrain scenarios. It is applicable for low frequencies between 40 and 1000 MHz and for distances up to 10 km. The path loss is given, in decibels, according to

$$PL_{Egli} = 91.2 + 40\log_{10}(d_D) - 20\log_{10}(h_t h_r) + 20\log_{10}(f) \quad (13)$$

where d_D stands for the direct distance, converted in kilometres, between Tx and Rx, f designates the operating frequency in MHz, and h_t, h_{tr}, denote the Tx and Rx heights, respectively. The results are presented in Fig. 3 where the path loss versus distance (in logarithmic scale) is provided along with the three different models for comparison.

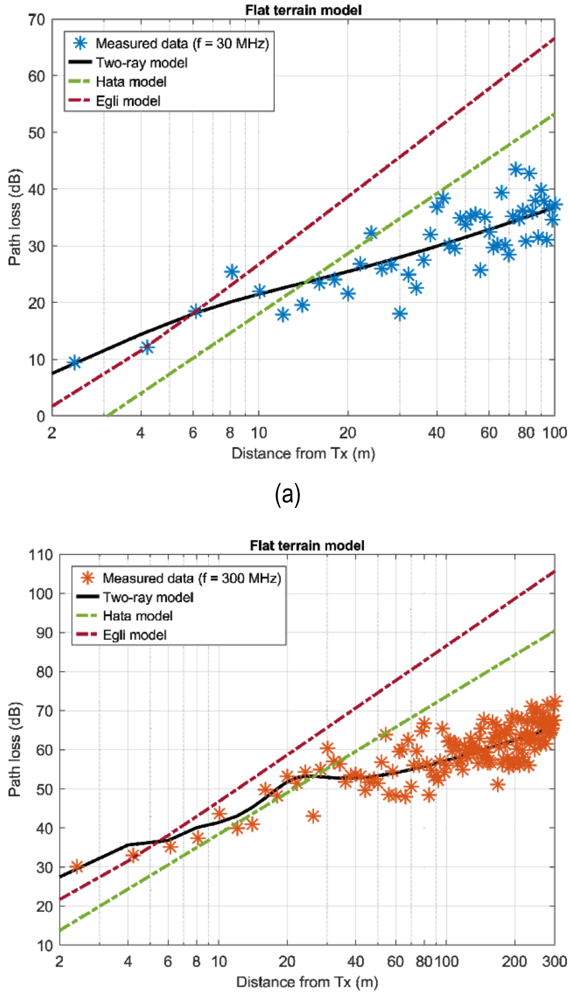

(a)

(b)

Figure 3. Path loss results versus distance. (a) 30 MHz and (b) 300 MHz

The results reveal that the "two-ray model" fits better to the measured samples. This can be credited to the geometrical nature of the applied model that considers the physical characteristics of the propagating signal over the flat terrain environment. This behaviour is apparent in both examined frequencies according to Fig. 3, although at 30 MHz the shadow fading (i.e., the path loss variations with respect to the two-ray model) are greater at 30 MHz, probably due to reflections from surrounding objects. Lower shadow fading is observed at 300 MHz.

Furthermore, both the "Extended Hata" and "Egli" models do not adapt well to the measured data at both 30 and 300 MHz. This is probably due to the low Tx and Rx heights that were used during the measurement campaign, which limits these two models' applicability. It is also worth commenting that both the "Extended Hata" and "Egli" models predict well the path loss in the first few meters at both examined frequencies (about 10 m for 30 MHz and 30 m at 300 MHz). However, after these distances, large discrepancies are encountered, between the measured and the predicted path loss.

In order to validate and compare quantitively the prediction accuracy, specific statistical metrics are applied, thereby determining the error between the measured and the forecasted path loss [29], [30], [31], [32]. The mean absolute error (MAE), in decibels, is given by:

$$\text{MAE} = \frac{1}{N}\sum_{i=1}^{N}\left|PL_i^{meas} - PL_i^{pred}\right| \quad (14)$$

where PL_i^{meas} and PL_i^{pred} stand for the measured and predicted path loss values, respectively, and i is the index of the measured sample. Finally, N is the total number of path loss samples. The mean absolute percentage error (MAPE) is calculated according to:

$$\text{MAPE} = \frac{1}{N}\sum_{i=1}^{N}\left|\frac{PL_i^{meas} - PL_i^{pred}}{PL_i^{meas}}\right| \times 100\% \quad (15)$$

Further, the root mean square error (RMSE), which actually represents the shadow factor is given, in decibels, by:

$$\text{RMSE} = \sqrt{\frac{1}{N}\sum_{i=1}^{N}\left(PL_i^{meas} - PL_i^{pred}\right)^2} \quad (16)$$

Finally, the cross-correlation coefficient reveals the degree of relationship between the measured and predicted samples. It is defined as the Pearson product moment [33], and can be calculated according to:

$$\rho = \frac{\sum_{i=1}^{N}\left(PL_i^{meas} - \overline{PL_i^{meas}}\right)\left(PL_i^{pred} - \overline{PL_i^{pred}}\right)}{\sqrt{\sum_{i=1}^{N}\left(PL_i^{meas} - \overline{PL_i^{meas}}\right)^2 \sum_{i=1}^{N}\left(PL_i^{pred} - \overline{PL_i^{pred}}\right)^2}} \quad (17)$$

Cross-correlation is a nonparametric measure of the statistical dependence among the measured and the forecasted path loss. Based on the absolute value the coefficient, the correlation between the measurements and the prediction can be classified as strong for values 0.6-0.79 and very strong for values 0.8-1.0 [31]. Acceptable correlation values are those greater than 0.8 that validate the appropriateness of an assessed model [34].

The statistical errors are determined in the following, by using (14)-(17), for each examined model. Table II summarizes the numerical results for each evaluated model and frequency scenario.

TABLE II.
Statistical results between measured and predicted path loss for Two-Ray (TR), Extended Hata (EH) and Egli (EG) models at each frequency scenario

Model	Metric	30 MHz	300 MHz
TR	MAE [dB]	**3.3**	**3.2**
	MAPE [%]	**1.9**	**1.5**
	RMSE [dB]	**4.3**	**4.0**
	ρ	**0.84**	**0.85**
EH	MAE [dB]	**10.7**	**9.4**
	MAPE [%]	**9.5**	**8.2**
	RMSE [dB]	**12.0**	**11.1**
	ρ	**0.76**	**0.79**
EG	MAE [dB]	**13.7**	**13.1**
	MAPE [%]	**11.4**	**10.2**
	RMSE [dB]	**15.6**	**14.7**
	ρ	**0.61**	**0.66**

The results in Table II reveal that “Two-Ray” (TR) model is better applicable in a near flat-terrain environment, that is much lower errors are obtained, as compared with the “Extended Hata” (EH) and “Egli” (EG) models. In terms of RMSE, TR model fits better at 300 MHz, although the errors between (for TR model) 30 and 300 MHz can be regarded as comparable.

On the other hand, EH and EG models exhibit much higher errors, with EG model to be inferior between all the examined models. Despite the high errors, EH and EG models seem to adapt better at 300 MHz, which indicates that are more appropriate at higher frequency applications over near flat terrain scenarios. However, disappointing results are encountered at 30 MHz, where very high errors and very low correlations are obtained. Finally, it is proved that empirical models, such as EH and EG are not recommended for near flat-terrain and low frequency scenarios providing inaccurate forecasts.

4. CONCLUSION

In this paper we presented an outdoor experimental measurement campaign of our research group from propagation of EM waves over flat terrain at 30 MHz and 300 MHz (‘low frequencies’ in our ‘language’, where ‘surface waves’ may exist). The measured data were compared with Extended Hata and Egli empirical models, as well as with the two-ray geometrical optic model. According to the statistical analysis it is observed that the latter model exhibits the best performance predicting the path loss with remarkable accuracy in both examined frequency scenarios.

As possible future work, the authors would like to assess additional path loss models of theirs (obtained by them previously through their previous analytical EM propagation methods above flat terrain), and validate their suitability to predict accurately the path loss in near flat-terrain scenarios.

ACKNOWLEDGEMENT

The authors would like to thank the Ministry of Education and Science of the Republic of Kazakhstan (Grant No. AP19676900), which supported this research. In addition, they would like to thank Ph.D. candidate Mr. Basil Massinas (at NTUA) for his valuable help in the preparation of this paper.

References

[1] A. N. Sommerfeld, "Propagation of waves in wireless telegraphy," *Ann. Phys.*, 1909, 28, pp. 665-737.

[2] K. A. Norton, "The propagation of radio waves over the surface of the earth and in the upper atmosphere," *Proc. Inst. Radio Eng.*, vol. 24, no. 10, pp. 1367-1387, Oct. 1935. doi:10.1109/JRPROC.1936.227360.

[3] A. K. Norton, "The propagation of radio waves over the surface of the earth and in the upper atmosphere," *Proc. Inst. Radio Eng.*, vol. 25, no. 9, pp. 1203-1236, Sep. 1937. doi:10.1109/JRPROC.1937.228544.

[4] J. Wait, "Launching a surface wave over the earth," *Electron. Lett.*, vol. 3, no. 9, pp. 396-397, Sep. 1967. doi:10.1049/el:19670307.

[5] R. J. King, "Electromagnetic wave propagation over a constant impedance plane," *Radio Sci.* 1969, 4, pp. 255-268, doi:10.1029/RS004i003p00255.

[6] T. K. Sarkar, W. Dyab, M. N. Abdallah, M. Salazar-Palma, M. V. S. N. Prasad, S. W. Ting, and S. Barbin, "Electromagnetic macromodeling of propagation in mobile wireless communication: Theory and experiment," *IEEE Antennas Propag. Mag.*, 2012, 54, pp. 17-43, doi:10.1109/MAP.2012.6387779.

[7] J.G.V. Bladel, *The Sommerfeld Dipole Problem. In Electromagnetic Fields*, J. Wiley and Sons, Inc.: Hoboken, NJ, USA, 2007; Section 9.3, pp. 448–452.

[8] G. Tyras, *Field of a Dipole in a Stratified Medium. In Radiation and Propagation of Electromagnetic Waves*; Academic Press, Inc., New York, NY, USA, 1969; Section 6, pp. 133–160.

[9] Y. Rahmat-Samii, R. Mittra, P. Parhami, "Evaluation of Sommerfeld Integrals for Lossy Half-Space Problems". *Electromagnetics,* 1981, 1, pp. 1–28, doi: 10.1080/02726348108915122.

[10] R. E. Collin, "Hertzian dipole radiating over a lossy earth or sea: some early and late 20th-century controversies". *IEEE Antennas Propag. Mag.,* 2004, 46, pp. 64–79, doi:10.1109/MAP.2004.1305535.

[11] K. A. Michalski, "On the efficient evaluation of integral arising in the sommerfeld halfspace problem". *IEE Proc.-Microwaves, Antennas Propag.,* 1985, 132, pp. 312–318, doi:10.1049/ip-h-2.1985.0056.

[12] G. Pelosi, J. L. Volakis, "On the Centennial of Sommerfeld's Solution to the Problem of Dipole Radiation Over an Imperfectly Conducting Half Space", *IEEE Antennas Propag. Mag.,* 2010, 52, pp. 198–201, doi: 10.1109/MAP.2010.5586629.

[13] J. R. Wait, "The Ancient and Modern History of EM Ground-Wave Propagation.", *IEEE Antennas Propag. Mag.,* 1998, 40, pp. 7–24, doi:10.1109/74.735961.

[14] A. Baños, *Dipole Radiation in the Presence of a Conducting Half-Space*, Pergamon Press, Oxford, UK, 1966; pp. 151–158.

[15] S. S. Sautbekov, R.N. Kasimkhanova,; P.V. Frangos, *"Modified Solution of Sommerfelds's Problem:*, In Proceedings of the CEMA'10 Conference, Athens, Greece, 7–9 October 2010; pp. 5–8. Available online: http://rcvt.tu-sofia.bg/CEMA/proceedings/CEMA_2010_proc.pdf (accessed on May 2021).

[16] S. Sautbekov, "The Generalized Solutions of a System of Maxwell's Equations for the Uniaxial Anisotropic Media. In Electromagnetic Waves Propagation in Complex Matter"; *IntechOpen Limited*: London, UK, 2011; Chapter 1, pp. 1–24, doi:10.5772/16886.

[17] K. Ioannidi, C. Christakis, S. Sautbekov, P. Frangos, and S. K. Atanov, "The Radiation Problem from a Vertical Hertzian Dipole Antenna above Flat and Lossy Ground: Novel Formulation in the Spectral Domain with Closed–Form Analytical Solution in the High Frequency Regime," *Int. J. Antennas Propag. (IJAP)*, 2014, Special Issue on 'Propagation of Electromagnetic Waves in Terrestrial Environment for Applications in Wireless Telecommunications', doi:10.1155/2014/989348.

[18] S. Bourgiotis, K. Ioannidi, C. Christakis, S. Sautbekov, P. Frangos, "The Radiation Problem from a Vertical Short Dipole Antenna Above Flat and Lossy Ground: Novel Formulation in the Spectral Domain with Numerical Solution and Closed-Form Analytical Solution in the High Frequency Regime", *Proceedings of CEMA'14 Conference*, Sofia, Bulgaria, 16–18 October 2014; pp. 12–18, Available online: http://rcvt.tu-sofia.bg/CEMA/proceedings/CEMA_2014_proc.pdf (accessed on May 2021).

[19] S. Bourgiotis, A. Chrysostomou, K. Ioannidi; S. Sautbekov and P. Frangos, "Radiation of a Vertical Dipole over Flat and Lossy Ground using the Spectral Domain Approach: Comparison of Stationary Phase Method Analytical Solution with Numerical Integration Results", *Electronics and Electrical Engineering Journal,* 2015, 21, pp. 38–41, doi:10.5755/j01.eee.21.3.10268.

[20] A. Chrysostomou, S. Bourgiotis, S. Sautbekov, K. Ioannidi, and P. Frangos, "Radiation of a Vertical Dipole Antenna over Flat and Lossy Ground: Accurate Electromagnetic Field Calculation using the Spectral Domain Approach along with Redefined Integral Representations and corresponding Novel Analytical Solution," *Electronics and Electrical Engineering Journal,* 2016, 22, pp. 54–61, doi:10.5755/j01.eie.22.2.14592.

[21] S. Sautbekov, S. Bourgiotis, A. Chrysostomou, and P. Frangos, "A Novel Asymptotic Solution to the Sommerfeld Radiation Problem: Analytic Field Expressions and the Emergence of the Surface Waves," *PIER M*, 2018, 64, pp. 9–22, doi:10.2528/PIERM17082806.

[22] S. Bourgiotis, P. Frangos, S. Sautbekov and M. Pshikov, "The Evaluation of an Asymptotic Solution to the Sommerfeld Radiation Problem using an Efficient Method for the Calculation of Sommerfeld Integrals in the Spectral Domain", *'Electronics' Journal*, MDPI Publisher, 1, https://doi.org/10.3390/electronics1010000, https://www.mdpi.com/journal/electronics, Special Issue on 'Propagation of Electromagnetic Waves in Terrestrial

Environment for Applications in Wireless Telecommunications and Radar Systems', June 2021.

[23] J. Fikioris, *Introduction to Antenna Theory and Propagation of Electromagnetic Waves;* National Technical University of Athens: Athens, Greece, 1982. (In Greek).

[24] International Organization for Standardization, "General requirements for the competence of testing and calibration laboratories," ISO/IEC 17025:2017, Geneva, Switzerland, Nov. 2017.

[25] T. S. Rappaport, *Wireless Communications: Principles and Practice*. (2nd ed.), Prentice Hall, Upper Saddle River, New Jersey, 2002.

[26] Electrical Characteristics of the Surface of the Earth, document ITU-R P.527-6, International Telecommunication Union, Geneva, Switzerland, Sep. 2021.

[27] Monte Carlo simulation methodology for the use in sharing and compatibility studies between different radio services or systems, document ITU-R SM.2028-2, International Telecommunication Union, Geneva, Switzerland, Jun. 2017.

[28] J. J. Egli, "Radio Propagation above 40 MC over irregular terrain," Proc. IRE, vol. 45, no. 10, pp. 1383-1391, Oct. 1957.

[29] E. Östlin, H. J. Zepernick, and H. Suzuki, "Macrocell path-loss prediction using artificial neural networks," *IEEE Trans. Veh. Technol.*, vol. 59, no. 6, pp. 2735-2747, Jul. 2010.

[30] Y. Zhang, *et al.*, "Path loss prediction based on machine learning: Principle, method, and data expansion," *Appl. Sci.*, vol. 9, no. 9, pp. 1-18, May 2019.

[31] J. D. Parsons, *The Mobile Radio Propagation Channel.* 2nd ed., New York: Wiley, 2000.

[32] X. Zhou, *et al.*, "Experimental characterization and correlation analysis of indoor channels at 15 GHz," *Int. J. Antennas Propag.*, Article ID 601835, 2015.

[33] W. C. Y. Lee, *Mobile communications design fundamentals*. Wiley series in telecommunications and signal processing. Wiley, 1993.

[34] M. J. Campbell and & T. D. V. Swinscow. *Statistics at Square One*. (11th ed.). Wiley, 2011.

TERRAIN CLASSIFICATION BY USING A LARGE SET OF SYNTHETIC APERTURE RADAR IMAGES AND MODIFIED FRACTAL SIGNATURE METHOD

Petros Doukas(1), Basil Massinas(1), Faethon Karagiannopoulos(1), Panayiotis Frangos(1)
and Seil Sautbekov(2)

(1) School of Electrical and Computing Engineering,
National Technical University of Athens (NTUA),
9, Iroon Polytechniou Str., 157 73 Zografou, Athens, Greece
Tel. : +30 210 772 3694; e-mail: pfrangos@central.ntua.gr

(2) Department of Physics and Technology, Al-Farabi Kazakh National University
Almaty, Kazakhstan
e-mail : sautbek@mail.ru

Abstract

In this paper a large dataset of satellite Synthetic Aperture Radar (SAR) Images from Capella's SAR mode satellite constellation system is analyzed by using the Modified Fractal Signature Method, for terrain classification. Four (4) types of terrain are considered (urban, mountain, rural and sea), and our numerical results show a good classification between them. Furthermore, nonlinear regression models are used to our results, showing also satisfactory differentiation between the four (4) terrain types.

1. INTRODUCTION

In this paper we obtained a large number of SAR satellite images from Capella's SAR mode satellite constellation system for classification purposes. Namely, we chose four (4) types for terrain classification, which are the following: urban, mountain, rural and sea. The classification is performed by using a well – known in the literature fractal technique, namely the Modified Fractal Signature (MFS) Method [1-9]. Namely, compared to Ref. [9], the main advantage here is that we used a very large number of SAR images, that is 100 images for each type of terrain (400 SAR images), which we consider as an important advantage as compared to [9].

2. SAR DATA PRESENTATION USED IN THIS WORK

In this work we used SAR images obtained by the Capella X-SAR Earth observation satellite constellation system [10], collecting high-resolution X-band synthetic aperture radar images, with spatial resolution less than 1 m. The constellation operates at an altitude of 485-525 km. We used 'Single Look Complex' (SLC) images, which are free offered data [10], containing both the amplitude and phase of the radar signal. The SLC SAR images are available in GeoTIFF format, which means georeferenced TIFF images. The SAR used frequency band is at X-band (9.4 – 9.9 GHz).

The dataset consists of:

1. 100 SAR images for mountainous regions.
2. 100 SAR images for urban regions.
3. 100 SAR images for rural regions.
4. 100 SAR images for sea regions.

GeoTIFF images collected from Capella's SAR mode satellite constellation, which offer spatial resolution less than 1m and well-defined area coverage. Below follow four (4) representative images from the dataset.

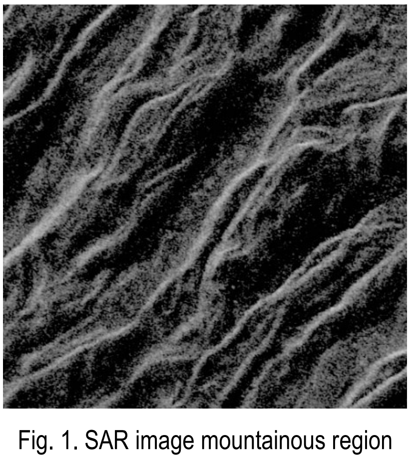

Fig. 1. SAR image mountainous region

Fig. 2. SAR image urban region

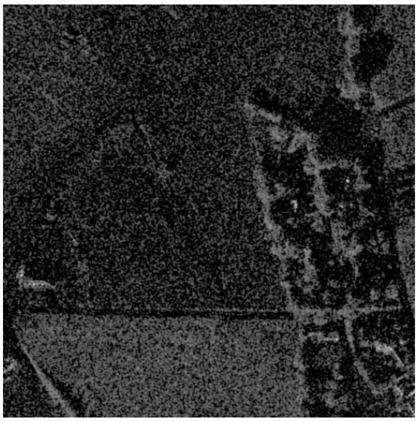

Fig. 3. SAR image rural region

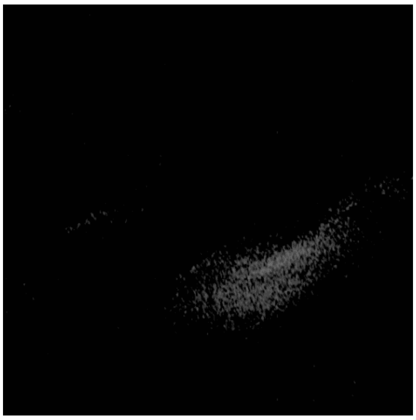

Fig. 4. SAR image sea region

Each one of the 400 SLC SAR images has 500 x 500 pixels size resolution and the amplitude magnitude of each one of these images is in the range 0 to 256.

3. MODIFIED FRACTAL SIGNATURE (MFS) METHOD USED IN OUR WORK

In this paper we are using the MFS fractal method, as we also did in Ref. [9] [see also Refs. [3], [4]], but here with the very important advantage using a very large number of real spaceborne SAR data.

The main function that we are using here is $F_D(\delta)$

$$F_D = 2 - \frac{\log_2 A_{\delta 1} - \log_2 A_{\delta 2}}{\log_2 \delta_2 - \log_2 \delta_1} \qquad (1)$$

which represents the 'Fractal Dimension' of the SLC SAR image (it is a characteristic function of the image ([3], [4], [8],[11]). Please note here that δ denotes the *resolution* in the image (i.e. δ=1 means maximum resolution of the image, and furthermore as δ increases the resolution of the image is decreasing). For this reason function $F_D(\delta)$ is a decreasing function of δ. Note also that δ is the iteration number in this procedure ([3], [4], [8]), that is if F_D was a true fractal surface it would be a constant, i.e. independent of δ. Finally, note that function $F_D(\delta)$ in some way gives a measure of the 'roughness' of the surface, and this 'roughness' is increasing with increasing function $F_D(\delta)$. Furthermore, note that $F_D(\delta)$ is always a monotinically decreasing function of δ ([3], [4], [8]). Finally, in eq. (1) note that A(δ) is the *area* of the blanket corresponding to the real surface (amplitude of the SAR image [see ([3], [4], [8] for details].

4. SAR DATA PROCESSING AND NUMERICAL RESULTS (QUANTITATIVE TERRAIN CLASSIFICATION)

By obtaining 100 GeoTIFF SAR images per terrain class (1. Sea, 2. Rural, 3. Mountain, 4. Urban, as mentioned above), and by calulating the amplitude average for each pixel per SAR image and class, we obtained the following results, where in Fig. 5 we show the fractal dimension function $F_D(\delta)$ as a function of resolution (iteration) δ for the whole set of 400 images. Here, we can easily observe the nice quantitative classification between the four (4) types of terrain, which are in good agreement with our expectation (as mentioned in Section 3, above).

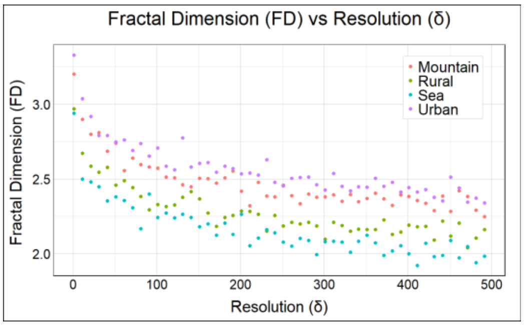

Fig. 5. Fractal dimension F_d as a function of δ (image resolution – iteration) in the MFS method for all chosen terrain classes

In the following two (2) figures we also obtained two types of curve fitting by using nonlinear regression analysis (3rd degree polynomial curve fitting, fig. 6, and logarithmic curve fitting, fig. 7).

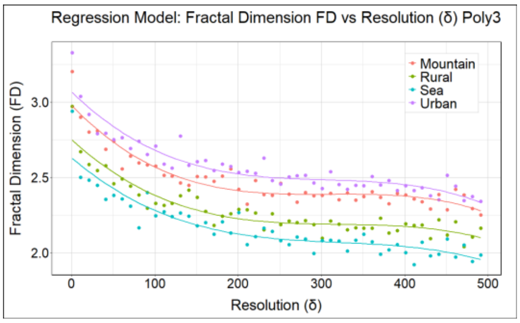

Fig. 6. Polynomial regression (3rd degree) for F_D vs δ

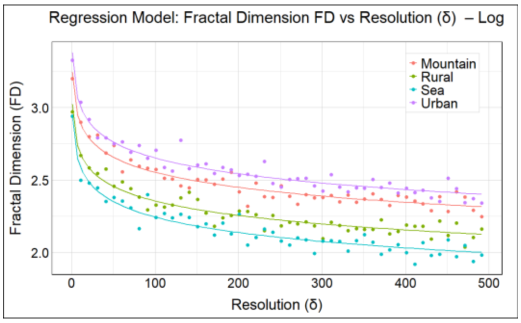

Fig. 7. Logarithmic regression for F_D vs δ

These two (2) figures (Fig. 6 and Fig. 7) show in an even clearer way the excellent classification of the four (4) spaceborne SAR images types (100 images per type).

Finally, please note that all the above quantitative classification processing was developed by using *R-software* (*R-software* is a modern free software environment for statistical computing-programming and graphics).

5. CONCLUSIONS – FUTURE RESEARCH

In this paper we used the MFS fractal method for quantitative terrain classification by using a very large set of spaceborne SAR SLC images. The numerical classification results were very promising.

As future research, we intend to use machine learning techniques (training and testing of real spaceborne SAR data), as well as by using more advanced fractal techniques.

ACKNOWLEDGEMENTS

The authors would like to thank the Ministry of Education and Science of the Republic of Kazakhstan (Grant No. AP19676900), which supported this research.

Furthermore, the authors would like to thank Professors N. Ampilova and I. Soloviev for many years discussions and scientific cooperation in the area of fractals.

References

[1] K. J. Falconer, Fractal Geometry: Mathematical Foundations and Applications. J. Wiley and Sons, 1990.

[2] D. Jaggard, A. Jaggard, P. Frangos, “Fractal electrodynamics: surfaces and superlattices”, in ’Frontiers in Electromagnetics”, IEEE Press, 2000.

[3] S. Peleg, J. Naor, R. Hartley, D. Avnir, “Multiple resolution texture analysis and classification”, IEEE Trans. Pattern Analysis and Machine Intelligence, vol. PAMI-6, no. 4, pp. 518–523, 1984.

[4] Y. Tang, H. Ma, D. Xi, X. Mao, C. Suen, “Modified fractal signature (MFS): a new approach to document analysis for automatic knowledge acquisition”, IEEE Trans. Knowledge and Data Engineering, vol. 9, no. 5, pp. 747–762, 1997.

[5] N. B. Ampilova, E. Y. Gurevich, I. P. Soloviev, “Application of modified fractal signature and Regny spectrum methods to the analysis of biomedical preparation images”, in Int. Conf. (CEMA 2011), Sofia, Bulgaria, 2011, pp. 96–100.

[6] D. Dai, W. Yang, H. Sun, “Multilevel local pattern histogram for SAR image classification”, IEEE Geoscience and Remote Sensing Letters, vol. 8, no. 2, pp. 225–229, 2011.

[7] O. Aytekin, M. Koc, I. Ulusoy, “Local primitive pattern for the classification of SAR images”, IEEE Trans. Geoscience and Remote Sensing, vol. 51, no. 4, pp. 2431–2441, 2013.

[8] A. Malamou, C. Pandis, A. Karakasiliotis, P. Stefaneas, E. Kallitsis, P. Frangos, “SAR imaging: an autofocusing method for improving image quality and MFS image classification technique”, Applications of Mathematics and Informatics to Science and Engineering, vol. 91, 2013.

[9] A. Malamou, C. Pandis, P. Frangos, P. Stefaneas, A. Karakasiliotis, and D. Kodokostas, “Application of the modified fractal signature method for terrain classification from synthetic aperture radar images”, Elektronika ir Elektrotechnika, Vol. 20, no. 6, pp. 118–121, 2014. DOI: 10.5755/j01.eee.20.6.7281.

[10] Capella Space Open Data Gallery: https://www.capellaspace.com/earth-observation/gallery

[11] A. Kotopoulis, B. Massinas, G. Pouraimis and P. Frangos,[11] ‘Sea State Characterization using Experimental Synthetic Aperture Radar Raw Data in Two-Dimensions and the Modified Fractal Signature Method’, ‘Elektronika ir Elektrotechnika’ Journal ELEKTRONIKA IR ELEKTROTECHNIKA, ISSN 1392-1215, VOL. 28, NO. 6, 2022.

DIGITAL VISUALIZATION OF SPACE CONFIGURATION OF LOW-FREQUENCY MAGNETIC FIELD USING EXPERIMENTAL DATA GENERATED FROM SYSTEMS FOR MAGNETOTHERAPY

Vladimir Nikolov

Faculty of Telecommunication, TU-Sofia, Bulgaria
Postal address: Bulgaria, Sofia, PostCode 1000, boulevard Kliment Ohridski 8
T.+359 965 2278 ; F. .+359 965 2278; E. v_nikolov@tu-sofia.bg

Abstract

The paper is devoted to the presentation of methods of investigation of the influence of low-frequency magnetic field on the human body. These methods are useful not only for scientific investigations in medicine and engineering, but also for education in the process of lifelong learning and perform calculation and visualization of the value of magnetic induction of low frequency magnetic field created by several coils, which is a typical situation for the modern systems for magneto-therapy.

1. INTRODUCTION

Visualization of space temporal configuration of the vectors of magnetic induction around and in the human body is very important requirement for obtaining of good results in magneto-therapy. This visualization can be obtained using one preliminary mathematical description of space temporal configuration of the vectors of magnetic induction around and in the human body. In most cases, in practice the required space configuration of the magnetic field is created by means of one or more air coils, which are appropriately arranged in the space. For a coil there is a linear relationship between the magnetic flux density of the excited magnetic field and current in the coils. It is assumed that the environment, in which the space-time configuration of the magnetic field is considered, is linear. The resulting field is the superposition of the fields of the individual coils, which forms a more complex time-spaced magnetic field. We suppose that the environment around the coils is homogeneous and the relative magnetic permeability is constant, i.e.

2. MATHEMATICAL MODEL FOR THE BASE CONFIGURATION

The results of mathematical, computer and experimental studies of the spatial configuration of the magnetic field excited by a cylindrical coil, one of the most common structures of the low-frequency excitation magnetic field, Visualization was performed in the plane orthogonal to the base plane of the coil. Numerical experiments were also performed for two coaxial coils. In what follows we use Fig.1 [11] illustrating a base model in the study of the spatial configuration of the magnetic field excited by a cylindrical coil.

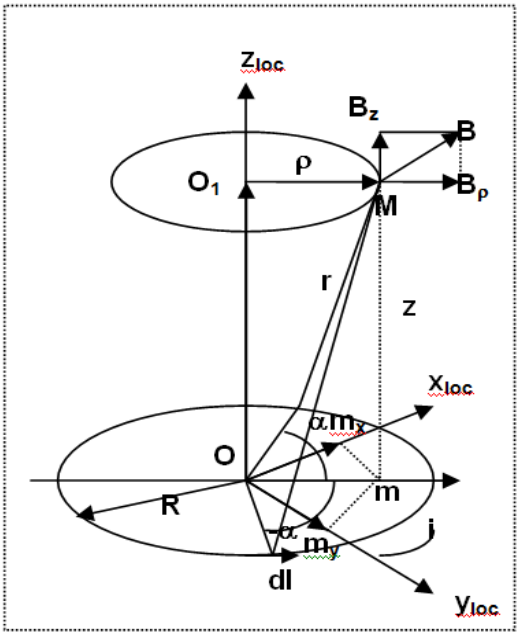

Fig. 1. Local cylindrical and Cartesian coordinate systems of a coil

Every coil has its own coordinate system — local cylindrical one. We denote this system by LC (with coordinates $\rho, z = z_{LC}$) and introduce the following notations:

i – current value in a single current loop;

R – radius of the current loop;

O – the origin of the cylindrical coordinate system of the coil;

M – an arbitrary point in which the magnetic induction is calculated;

m – the projection of the point M in the plane of current loop;

O_1 – the center of the circle lying in a plane parallel to the plane of the current loop and passing through the point M;

ρ – radius of the circle lying in the plane parallel to the plane of the current loop and passing through M;

dl – an elemental segment of the current loop;

2α – the central angle corresponding two symmetrical elemental segments;

r – the distance from any of endpoints of $2dl$ segment to the point M.

It should be noted that on Fig. 1 a current loop coincides with the base plane of the coil.

The vector of magnetic induction B in the point M has two components which can be calculated as the following [11]:

$$B_{\rho} = \frac{\mu_0 i}{2\pi} \frac{z}{\rho\sqrt{(R+\rho)^2+z^2}} \left(\frac{R^2+\rho^2+z^2}{(R-\rho)^2+z^2} L - K\right), \qquad (1)$$

$$B_{zLC} = \frac{\mu_0 i}{2\pi} \frac{1}{\sqrt{(R+\rho)^2+z^2}} \left(\frac{R^2-\rho^2-z^2}{(R-\rho)^2+z^2} L + K\right), \qquad (2)$$

where K and L are complete elliptic integrals of 1 and 2 sort as functions of k and

$$k^2 = \frac{4\rho R}{(R+\rho)^2+z^2}.$$

An example of visualization of magnetic induction for one coil is given below.

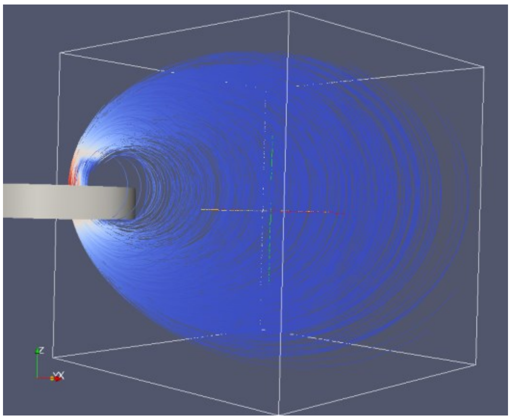

Fig. 2. 3D visualization of the magnetic field for one coil. The given space area is bounded by parallelepiped

3. MODEL FOR OUT-OF-LINE COILS

The real problem is to calculate and visualize in 3D magnetic field (in a given space area) generated by several coils, which are in an arbitrary disposition [1, 5, 6].

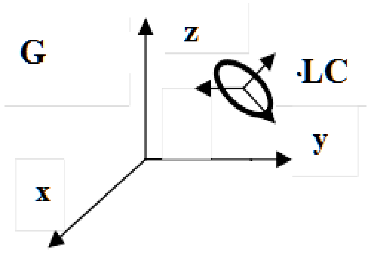

Fig. 3. Global coordinate system (G) and local cylindrical system (LC) of a coil

To do it, for a coil we consider a global coordinate system (G) with the origin O_G , local rectangular coordinate system (LR) with the origin O_L and local cylindrical coordinate system of the coil. The calculation of total magnetic field for several coils is performed in the area bounded by a rectangular parallelepiped. The area is divided on cells with the same size, which are also rectangular parallelepipeds. The calculation is performed in the nodes of the constructed mesh. The origin of G is supposed to be in the left bottom angle of the area (Fig.4).

Coils may be located both inside the area and outside it. Magnetic field values are calculated only inside the area. The direction of the coil axis is defined in accordance with the direction of current.

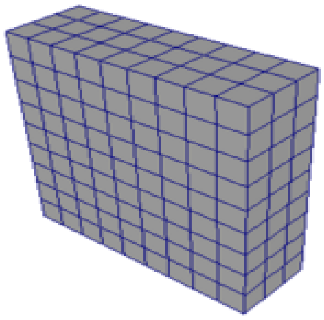

Fig. 4. The mesh of based points in a given area

For every coil we use an auxiliary local rectangular coordinate system (LR) to reduce calculations, because the transition from one Cartesian coordinate system to another is coordinate shift and multiplication on a transition matrix. In this way for every coil the transition and inverse transition matrix can be calculated only once.

So, for given coordinates of a coil in G the sequence of calculation is the following:

1. $G \rightarrow LR$
2. $LR \rightarrow LC$, calculations by (1)
3. $LC \rightarrow LR$
4. $LR \rightarrow G$.

The magnetic induction should be calculated in many points around the coils. The number of these points depends on the resolution of computer images and the space configuration of the field of magnetic induction. It is clear that the increasing of resolution of computer images would need increasing of number of points. To optimize running time a variant of the algorithm using parallel calculations has been implemented: for every coil calculation of magnetic induction has been performed in a separate flow. The results of experiments are described in [1] and show that such an optimization leads to significant decreasing of the run time.

An example of visualization of results of calculations for 3 given out-of-line coils is shown below.

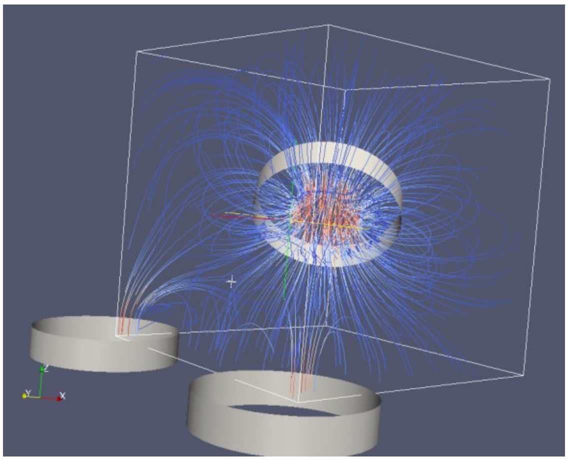

Fig. 5. Magnetic field generated by 3 out-of-line coils. Parallelepiped shows the area where magnetic induction is calculated

4. INTERPOLATION AS A METHOD FOR REDUCING RUN TIME

The described algorithm of calculation of magnetic induction may be optimized by combining calculation in some base points of the area with interpolation in the rest of points.

In [7, 8] we used values obtained by calculations as the base ones. These values are in nodes of 3-dimensional lattice and form interpolation nodes. We consider the following methods: 1) 3-dimensional linear interpolation, 2) one-dimensional quadratic Lagrange interpolation and 3) coordinate-wise cubic spline. Numerical experiments show that any of methods reduces the run-time considerably and does not lead to a loss of accuracy. For example, the results of experiments given in [7] show that 3D linear interpolation more effective than 1D Lagrange interpolation and it decreases run-time nearly 9 times for the number of nodes $2.5\text{x}10^6$.

5. INTERPOLATION BY USING EXPERIMENTAL DATA

For a special magnetotherapy device (magnet bed) the solution the problem of magnetic field interpolation by using experimental data was presented in [9]. In such a configuration at any moment only one pair of coils is active. In the process of the system functioning every pair of coils is active by turns, and a movement of magnetic field occurs.

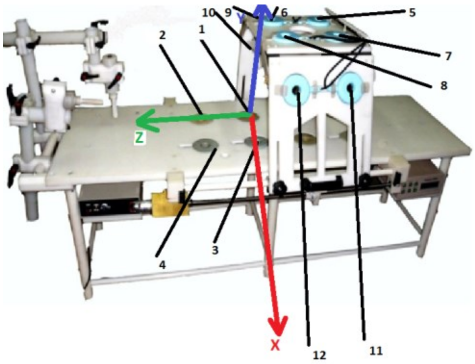

Fig. 6. Magneto bed, the coils and the coordinate system XYZ

For every given pair of coils the magnetic field was measured in the centers of coils and the middle of the interval between the centers. The measurement of magnetic induction is on the base special algorithm of microprocessor of information system for monitoring of magnetic field in the process of magneto-therapy. The values of magnetic induction are scalars (i.e. the module of the induction was measured). The interpolation of magnetic induction value in a given segment connecting centers of the coils (pair) and visualization of results have been performed. The order of the choice of pairs of coils is defined by a data table which also contains the coordinates of every measurement point.

We use one-dimensional quadratic Lagrange interpolation. As the electromagnetic induction value continuously depends on the point position, for any given pair of coils we at first calculate the induction value in all the points of the segment by step 1 mm (base points). Then we show the obtained distribution of the induction values in a special area in the interface in accordance with the following scheme (B denotes the induction value).

$B \in [0, a]$ –> blue,

$B \in [a, b]$ –> lightblue,

$B \in [b, c]$ –> yellow,

$B \in [c, d]$ –> orange,

$B > d$ –> red.

The user can choose the values of parameters a, b, c, d defining the color distribution. In this implementation the segment [0, d] is partitioned on 5 equal parts, where d is the maximal value of induction in the base points. Thus the diagram of color distribution is in agreement with the position of the point the user chooses as the interpolation one.

User interface is shown on Fig. 7.

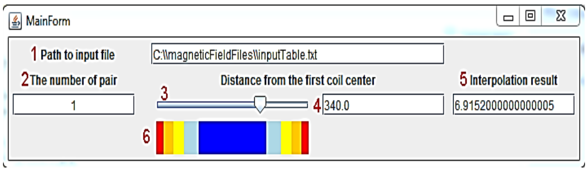

MainForm

1 Path to input file: C:\\magneticFieldFiles\\inputTable.txt

2 The number of pair: 1

Distance from the first coil center: 4 340.0

5 Interpolation result: 6.9152000000000005

Fig. 7. User interface for interpolation by experimental data

The user gives the path to the input file (in .txt format) that contains experimental data. In the field 2 one can choose a pair of coils (row number in the data table). Elements 3 and 4 are for input of the interpolation point. In 3 we select a point by slider, and when using 4 we should point a distance from the left end of the segment to the interpolation point. When changing data in 3 or 4 the result of interpolation is shown in 5 in real time. Note that color distribution diagram is drawn in element 6 immediately after the choice of coils, in doing so the position of slider corresponds the diagram.

6. CONCLUSION

The conclusion exemplifies the main results and the fundamental ideas presented in the paper. It should allow to fully recognize the goals of the presentation. In the conclusion, papers concerning educational activities should include an opening to the education community.

References

[1] N. Ampilova, D. Dimitrov, B.Kudrin. Mathematical modeling of low frequency magnetic field in systems for magnetotherapy .Proc. 8 Int. Conf. CEMA13, 17-19 Oct. 2013, Sofia, Bulgaria.

[2] N. Ampilova, I. Soloviev, E. Gurevich. Computer Methods of Investigation of Ultralow Doses Effects in Biomedical Applications. Proceedings of the International Conference on Biomedical Engineering and Systems, Prague, Czech Republic, August 14-15, 2014.

[3] D. Dimitrov. Medical Systems for Influence of Electromagnetic Field on the Human Body (in Bulgarian), Sophia, Technical University, 2008.

[4] L.N. Gall. Physical principles of functioning of a live organism matter. SPb, 2014 (in Russian)

[5] B. Kudrin, A.Dimitrov. An algorithm for visualization of low-frequency magnetic signals in systems for magnetotherapy. Proc. 8 Int. Conf. CEMA13, 17-19 Oct. 2013, Sofia, Bulgaria.

[6] B.Kudrin, A.Dimitrov. Computer visualization of low-frequency magnetic signals in systems for magnetotherapy with variable parameters. Proc. 8 Int. Conf. CEMA13, 17-19 Oct. 2013, Sofia, Bulgaria.

[7] B.Kudrin, I.Soloviev On interpolation methods of low frequency magnetic field in systems for magnetotherapy. Proc. 9 Int. Conf. CEMA14, 16-18 Oct. 2014, Sofia, Bulgaria.

[8] B. Kudrin, V. Nikolov. Algorithms of interpolation and visualization of low frequency magnetic field using experimental data. Proc. 9 Int. Conf. CEMA14, 16-18 Oct. 2014, Sofia, Bulgaria.

[9] B. Kudrin, V. Nikolov. On the mathematical model of interpolation of low frequency magnetic field using experimental data. Proc. 9 Int. Conf. CEMA14, 16-18 Oct. 2014, Sofia, Bulgaria.

[10] ParaView Tutorial: http://paraview.org/Wiki/images/d/d5/ParaViewTutorial398.pdf

[11] K. Brandiski, G. Georgiev, V. Mladenov, R. Stancheva Theoretical Electrical Sofia, Bulgaria

ALGORITHM FOR PROCESS CONTROL WHEN MEASURING MAGNETIC INDUCTION GENERATED BY A MAGNETIC PHYSIOTHERAPY BED

Vladimir Nikolov

Faculty of Telecommunication, TU-Sofia, Bulgaria
Postal address: Bulgaria, Sofia, PostCode 1000, boulevard Kliment Ohridski 8
T.+359 965 2278 ; F. .+359 965 2278; E. v_nikolov@tu-sofia.bg

Abstract

In this article is considered the algorithm for measuring the low-frequency magnetic fields. The algorithm used to construct the apparatus for measuring low frequency magnetic fields generated by systems for magnetotherapy, using moving magnetic field. The possibility for simultaneously influence of low frequency magnetic field on different part of the human body is one additional advantage of systems for magnetotherapy, using moving magnetic field.

1. INTRODUCTION

One new method for magneto-therapy by movement of magnetic wave is used during the last time in medicine. This kind of magneto-therapy can be provided by several pairs of coils, situated on the bed for therapy. All coils are connected with the outputs of apparatus for magneto therapy, which can be situated under the bed for magneto therapy. The movement of magnetic wave can be provided by electronic switching of different coils. Usually there is a microprocessor is upgraded in the apparatus for magneto therapy. The switching of coils can be provided using appropriate software for the microprocessor. It‘s very friendly to be changed parameters of magnetic fields of different coils by the same software, also.

2. DESIGN OF INFORMATION SYSTEM FOR MONITORING OF PROCESS FOR MAGNETOTHERAPY WITH RUNNING MAGNETIC FIELD

The functional scheme of system for monitoring of magnetic induction in system for magneto-therapy with running magnetic field can be seen in Fig.1. It consists of two basic units: patient’s bed for magneto-therapy and unit for measuring of parameters of low frequency magnetic field. The patient’s bed consists apparatus for magneto-therapy and inductors. The unit for measuring of parameters of low frequency magnetic field consists magnetic sensors for measurement of magnetic induction of low frequency magnetic field, microprocessor for management of process of measurement of magnetic induction in different point around the human body USB unit and display or PC for visualization of results of measurement. There is feedback from unit for measurement to the apparatus for magneto-therapy for keeping the preliminary defined values of parameters of magnetic induction in different points around the human body and their changes in the time.

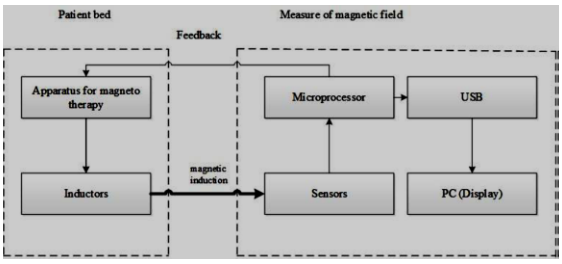

Figure 1. Functional scheme of system for monitoring of magnetic induction in system for magneto-therapy with running magnetic field

The magnetic bed with running low frequency magnetic field can be seen on fig.2. It’s consists plastic patient’s bed and plastic carriage on the bed, inductors , which are situated on the patient’s bed and on the carriage, apparatus for magneto-therapy (under the bed) , sensors for measurement of magnetic induction on every inductor. The apparatus for magneto-therapy provides low frequency pulses of electrical current with preliminary defined parameters according to the program for procedure of therapy. The magnetic inductors are connected to the outputs of apparatus for magneto-therapy. The magnetic sensors are connected to the inputs of microprocessor’s unit using coaxial cables for reducing influence of noise. The carriage can do axial movement on the axis of patient's bed during the procedure of therapy or can be without movement according to the medical requirements for therapy.

The running of magnetic field can be provided not only on axis of magnetic bed by movement of carriage, but by switching over of inductors, also. This switching can be according to different programs of microprocessor's unit. It's clear that it's possible to be provided many kinds of movement (running) of low frequency magnetic field by using microprocessor's unit.

This is one of the important advantages of described systems. In the same time can be provided permanent measurement of magnetic induction of magnetic field created by every inductor. On the base of results of these measurements can be provided visualization of space configuration of magnetic field around the human body on the display. The treatment of results of measurements is according of special algorithm, described below. The results of measurement are used simultaneously for feedback from microprocessor's unit to the apparatus for magneto-therapy. There are 8 inductors on the patient's bed and 8 inductors on the carriage (Fig. 2). The number of used sensors is 16.

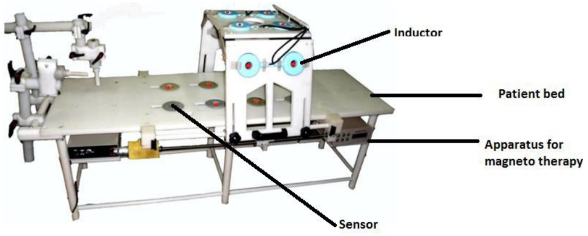

Figure 2. Magnetic bed

3. ALGORITHM FOR MANAGEMENT OF MICROPROCESSOR UNIT IN THE PROCESS OF MEASUREMENT OF MAGNETIC INDUCTION

3.1. Basic principles in the process of measurements

The duration of measurements is 1s.The maximal measured value for this period is defined as a maximum is recorded in the register as the maximum value. There are also additional control which reduces errors caused by external disturbances. When the measured value of the amplitude is more high than the preliminary defined maximum possible value of the field, the measured value is ignored and not included the min determining the maximum value of the measuring field. When the difference between two measured values is more high than a predetermined value, the measured value is ignored and not included in subsequent measurements in the determination of the maximum value of the field. In both cases the measurement errors can arise when there is an external disturbance in the system.

Because of these preliminary defined requirements the mistakes in the process of measurements can be reduced. The algorithm for management of microprocessor's unit in the process of measurement of magnetic induction can be seen on fig.3.

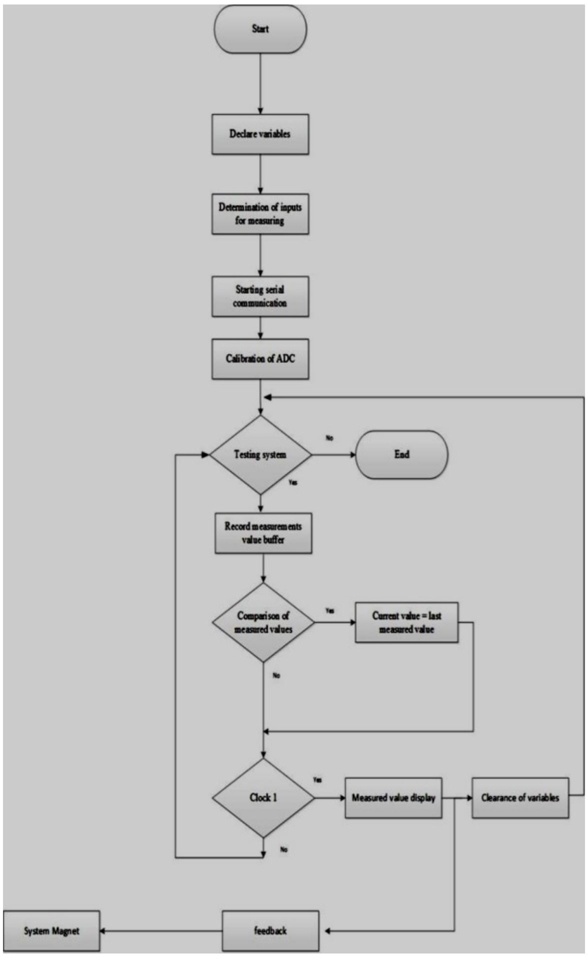

Figure 3. Algorithm for management of microprocessor's unit in the process of measurement of magnetic induction

3.2. Description of algorithm

Declaring variables: This block describes all variables which will be used in the program of the microprocessor.

Determination of inputs for measurement: In this block, the algorithm determines which pins on the microprocessor will be used, which are input pins and which are output pins.

Additionally in this block pins for analog signals and pins for digital signals are defined.

Starting serial communication: This is the block of connection between the microprocessor and the next device (PC), which will be processed measured data is performed via the serial interface. This iteration configures the speed of data transmission between microprocessor and PC.

Calibration of the ADC-This is the block for definition of maximum value of magnetic induction which will be measured using ADC.

Testing of system-This is the cycle in which the program runs continuously.

Recording of measured values from sensors in buffer: In this block the measured values of magnetic induction in every moment are saved in the local memory of microprocessor.

Comparison of measured values: In this block there is a comparison between the value of the instantaneous measured value of the sensor and the previous measured value. If the new measured value is more high than the previous value and the new measured value is more high than the maximum permissible value, the measured value will be determined as maximum and will be stored in the microprocessor. If the above condition is not met, the measured value is ignored.

Clock – 1: In this block should be determined length of the interval for measurements of the amplitude of the magnetic induction (e.g. 1s) and should be chosen the maximum measured value of magnetic induction, which will be transmitted to the next device.

4. CONCLUSION

The described system for monitoring of magnetic induction is very actual and friendly used in magneto-therapy. It's provides on line visualization of space distribution of values of magnetic induction around the human body and in the human body during the procedure of therapy. The microprocessor's unit of this system allows to manage measurement of amplitude of magnetic induction in the case of application of magnetic signals with frequency and/or amplitude modulation. This system allows also to be provided space visualization of space distribution of the values of magnetic induction in the case of "running" low frequency magnetic field. The scheme of described information system, which is suggested in the paper and suggested microprocessor's algorithms for management of simultaneously measurement of the values of magnetic induction in different points are tested successfully in real conditions in hospitals.

References

[1] W. Y. Riadh, "Electromagnetic Fields and Radiation (Human Bioeffects and Safety)", Marcel Dekker Inc., Canada, 2001 ISBN 0-8247-0877-3, p.420.

[2] B. Kudrin, V. Nikolov, "Algorithms of interpolation and visualization of low frequency magnetic field by using experimental data" 9th International Conference CEMA'14, Sofia, 2014, pp.43-45.

[3] B. Kudrin, V. Nikolov, "On the mathematical model of interpolation of low frequency Magnetic field using experimental data" 9th International Conference CEMA'14, Sofia, 2014, pp.80-84.

[4] D. Tz. Dimitrov, A.Computer Simulation of Low Frequency Magnetic Field, Proceedings of 17th EAEEIE Annual Conference on Innovation in Education for Electronical and Information Engineering, Craiova, Romania, 2006, p. 33-36.

[5] Lin, J. C., (ed.), Electromagnetics in Biology and Medicine, Review of Radio Science, 2000, p.330.

[6] Lin, J. C., (ed.), Electromagnetics in Biology and Medicine, Review of Radio Science 1993-1996, Oxford University Press, London, UK, p.470,1996.

[7] Malmivuo, J., and R. Plonsey, Principlesand Applications of Bioelectric and Biomagnetic Fields, Oxford University Press, New York, NY, 1995, p.480.

[8] P. J. Rosch, M. S. Markov, "Bioelectric Medicine", The American Institute of Stress, Yonkers, New York, U.S.A., and New York Medical College, Valhalla, New York, U.S.A.1999, ISBN: 0-8247-4700-3, 1999, p.360.

ESTIMATIONS OF REAL-WORLD ACOUSTIC DATA VIA COMPRESSED SENSING

I. Simeonov, N. Yordanov

Vasil Levski National Military University, Veliko Tarnovo, Bulgaria
76, Bulgaria Blvd., 5000, Veliko Tarnovo, Bulgaria
Tel. +359 62 618724, Fax. +359 62 618899, E-mail: ivanov_ivan@nvu.bg, nkyordanov@nvu.bg

Abstract

Last years the potentials of compressed sensing - CS systems were demonstrated in many information theory and signal processing application for improving the sampling efficiency and achieving the high-precision reconstruction.

CS simplifies the sampling and compression procedures, but it was difficulties to the signal reconstruction.

Some experiments with spectral entropy variations of empiric acoustic data are carried out.

In this work we apply the CS method to solve a practical problem of improving the real-world signal detection and estimation in case of small signal to noise ratio, like drone acoustic signal signatures, gunfire noises etc..

1. INTRODUCTION

Numerous team projects have resulted in collection of an extensive amount of acoustic data and in the study of signal processing of high dynamic range acoustic signals in the presence of noise [1, 2, 3, 4, 11].

Those works have addressed the specific applications and analyses using Approximate Entropy (ApEn).

Some concepts of entropy have been proposed as an interesting approach used in the field of compressed sensing, based on Shannon's Source Coding Theorem (see the work of Zbili and Rama, 2021, [7]).

The concept of entropy was introduced by Clausius in mid-19th century as an abstract mathematical property in thermodynamics. It is known that Shannon entropy is one of the fundamental measures used for evaluating entropy. This concept has found numerous applications in fields such as information theory communication theory, biology, neuroscience, and many others [1–12]. A literature review on the empirical estimation of entropy can be found in Verdú, 2019 [5].

Recently, predator–prey models of interactions have become gained attention. Tsvetkov and Angelova-Slavova [6] proposed a description of the continuous-time Leslie–Gower model, where they proved the existence of positive ω-periodic solutions using the operator method in Banach spaces. The dynamic behaviors of a new Leslie–Gower discrete-time system with the Allee effect was investigate in Hamadneh, T. et al. [8]. For the chaotic dynamics of this system Hamadneh et al. used a measure of approximate entropy.

Approximate Entropy (ApEn) was initially developed to analyze medical data, such as heart rate variability, in 1991 [9].

ApEn was developed by Steve M. Pincus to address the limitations related to the vast amounts of data required for accurate entropy calculation and the fact that results can be greatly influenced by system noise [10].

2. EXPERIMENTAL ACOUSTIC DATA ENTROPY

The experimental setup consists hardware:

Teleoperated compact quadcopter DJI Mavic Air 2s; Bruel and Kjaer 5-channel PULSE Data Acquisition Unit 3560B; 1/2" low frequency pressure field microphone BK 4193; laptop, and accessories.

The microphone is mounted on a mast at a height of 4.6 meters above the surface. The terrain is a flat grassy area. The air temperature was 25 degrees Celsius, wind speed - 0.9 m/s, the humidity - 43%. In Fig. 1 a, b, c is presented the recorded sound when the drone landed at a distance of 10 m.

Some experiments were made with a compact quadcopter DJI in the area in order to register the sound picture during takeoff and landing. In this study, we focus on the analysis of drone acoustic signatures, particularly the noise generated during landing.

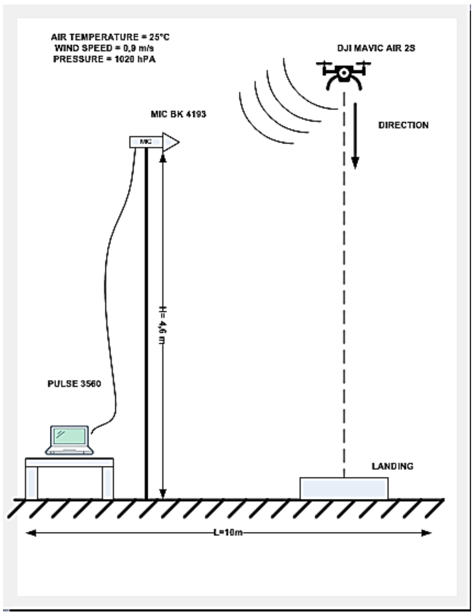

a) Schema of experimental set up

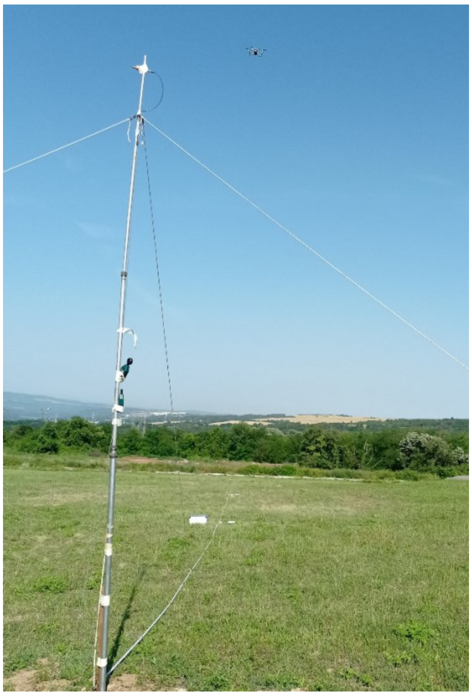

b) Experimental set up view

c) Experimental set up view

Figure 1

The following section describes the analysis of a set of experimental data, analogous to the work [4] and the estimated unpredictability of signal fluctuations by Approximate entropy calculations.

Fig. 2 illustrates the recorded signal of 54 seconds in total in the form of a spectrogram made with software Audacity. Low-frequency components caused by the wind has been noticeable, a high-pass filter HPF 0.7 Hz was used in the recording. The harmonics caused by the rotation of the propellers are also well distinguished.

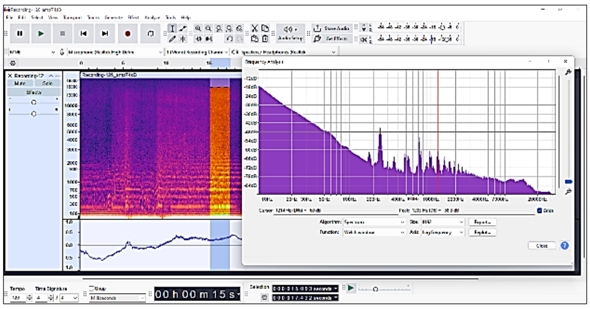

a) Spectrum in moment of flying. The drone descent 52 seconds, and 2sec. landing, 131072 samples,data126 all (1048576:1081343)

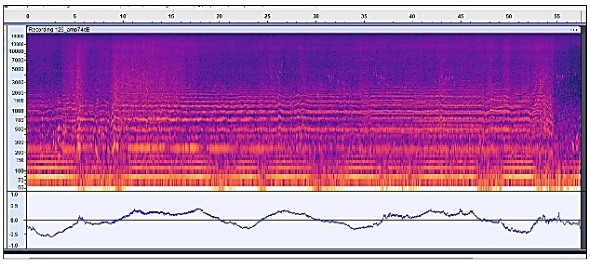

b) STFT for the drone descent 52 seconds, and 2 sec landing, 131072 samples

Figure 2

Fig 3a) shows a part of the record's signal that describes the flying before landing (16-16.5 seconds). The power spectral density is calculated in MatLab for the same time fragment, 16-16.5 seconds, (Fig. 3b).

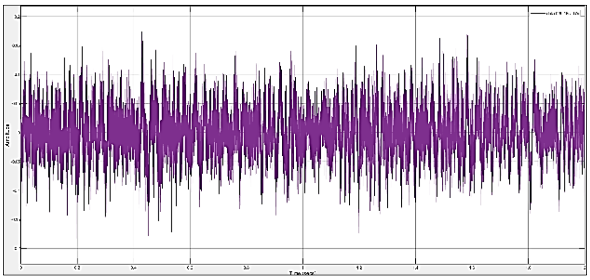

Figure 3. a) Part 16-16.5 seconds of signal in time, 32768 samples, data126all (1048576: 1081343).

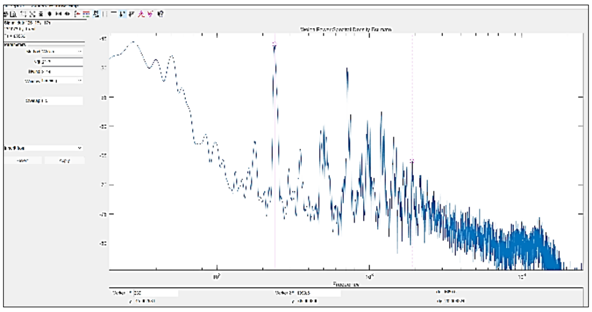

Figure 3. b) The power spectral density of 16-16.5 seconds, "data126all(1048576:1081343)",

Previous studies [3,4] have demonstrated the analysis of a set of experimental data for pulse signals (Fig. 4). Some raw data, that consists of time signals recorded from the blasts from 122 mm 2S1 howitzer ("Gvozdika"), has been analysed in MatLab and evaluated with calculations of the ApEn. [3,11]

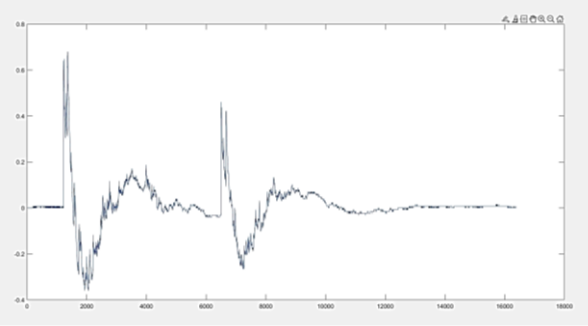

Figure 4. Part of signal in time recorded from the 2S1 howitzer blasts, $\mathbf{2^{14}}$ samples, ApEn=0,30635 see rec9sss [4]

Fig. 4 presents a signal in the time domain for a burst of two pulses. In previous works [3, 11] it has been demonstrated that the presence of a strong energy and a noise-like component does not significantly change the spectral entropy picture.

The approximate entropy for the blast signal see fig. 4 and for similar pulse signals have been found in MatLab and the ApEn calculating steps has been described in the works of Delgado-Bonal et al. [12].

Tab. 1 illustrates two parts of the landing drone's signal data126, with respectively time periods of 0.5 and 1 seconds, for which ApEn values were calculated in MatLab.

Signal "date 126" is a 4.7 sec. part of the entire 54 sec. record "date126all". That is, these are the last 4.7 sec. where the drone lands.

It can be seen in Table1 that App entropy was decrease for increasing of signal time duration, i.e. number of samples.

Table 1.

Name of signal*	App. Entropy	Number of samples	Dim; Lag
data126p8	1.3154	2^15	2; 10
data126p8p9	1,247	2^16	2; 10

* Signals of moment of landing that consist 32768 and 65536 samples, see last seconds fig. 2a).

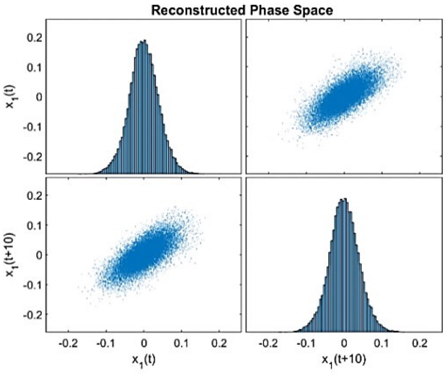

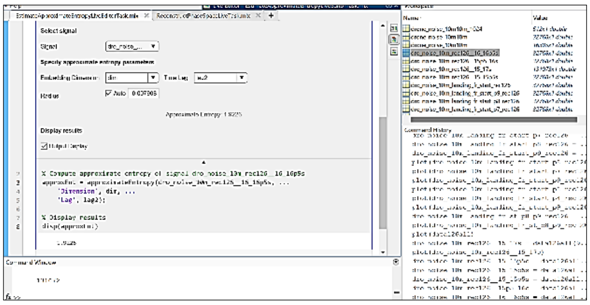

```
% Compute approximate entropy of signal dro_noise_10m_rec126__16_16p5s
approxEnt = approximateEntropy(dro_noise_10m_rec126__16_16p5s, ...
    'Dimension', dim, ...
    'Lag', lag2);

% Display results
disp(approxEnt)
```

Figure 5. a) Signal waveform and reconstruction the phase, for time slice 0,5 sec., moment of drone flying at height of about 10 m, data126all, 16 to 16,5 sec.
App. Ent. = 1,9226, dim = 2, lag = 10.

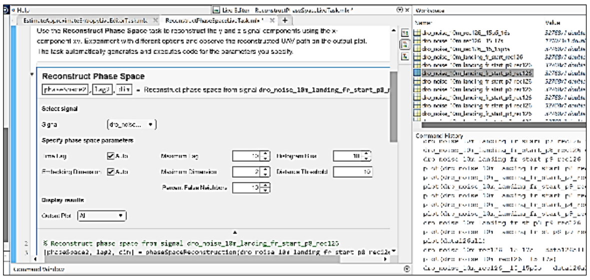

Use the Reconstruct Phase Space task to reconstruct the y and z signal components using the x-component xv. Experiment with different options and observe the reconstructed UAV path on the output plot. The task automatically generates and executes code for the parameters you specify.

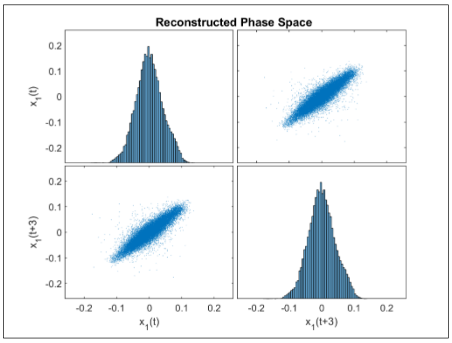

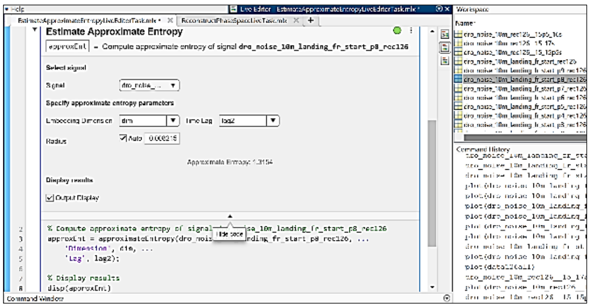

Estimate Approximate Entropy

approxEnt = Compute approximate entropy of signal dro_noise_10m_landing_fr_start_p8_rec126

Select signal

Signal: dro_noise_...

Specify approximate entropy parameters

Embedding Dimension: dim   Time Lag: lag2

Radius: ☑ Auto 0.000215

Approximate Entropy: 1.3154

Display results

☑ Output Display

```
% Compute approximate entropy of signal      se_10m_landing_fr_start_p8_rec126
approxEnt = approximateEntropy(dro_nois      nding_fr_start_p8_rec126, ...
    'Dimension', dim, ...
    'Lag', lag2);

% Display results
disp(approxEnt)
```

Figure 5. b) Signal waveform and reconstruction the phase for time slice 0,5 sec., moment of landing data126 (229376:262143); App. Ent. = 1.3154, dim = 2, lag = 10.

In next part are presented sections, "time slices", of 32768 samples(0,5sec.), cut from the initial signal data126 and the calculated ApEn in MatLab. Signal waveform and corresponding reconstruction the phase space of the signal for three of these slices are illustrated on fig. 6 a, b.

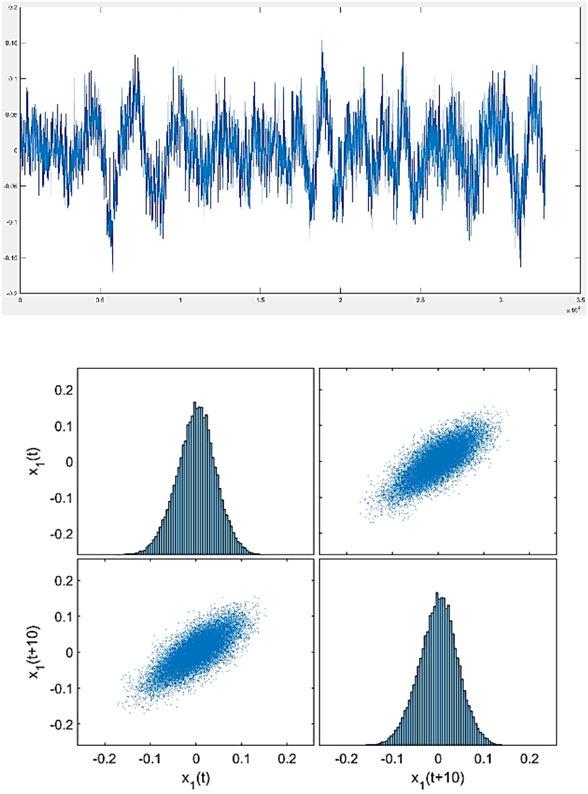

Figure 6. a) Signal waveform and reconstruction the phase space of the signal of 32768 samples, Dim=2; lag=10. of the end 0,5 second part of the signal (2 seconds before the drone landing), Ap.En. = 1.8591; data126(98304: 131071).

The entropies were calculated for three time files, each of 2^{17} samples, for three consecutive segments of 0.5 seconds, for moment of drone flying at height of about 10 m and 15 to16.5 seconds, from the entire signal describing the descent: 15-15.5s; 15.5-16s;16-16.5 s.

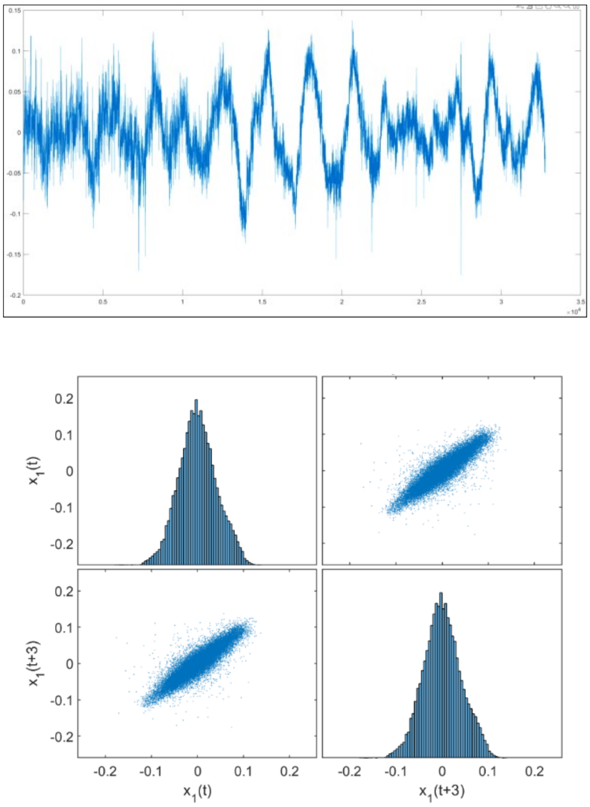

Figure 6. b) Signal waveform and reconstruction the phase space of the 0,5 second part of the signal (drone was landing), Ap.En. = 1,3154; data126 (229376:262143).

In Table 2 are shown results for ApEn for this three 0,5 s 'time slices', where Dim=2, Lag = 10, and consist 32768 samples.

Table 2.

Name of signal	Approximate Entropy	N samples
rec126__15_15p5s	1,9742	(983040:1015807)
rec126__15p5_16s	1,9664	(1015808:1048575);
rec126__16_16p5s	1,9226	(1048576:1081343);

The Approximate Entropy variations through different time signal parts can be seen as a tool for the estimation of unpredictability of signal fluctuations.

In Table 3 are shown results for ApEn for 0.5 second 'time slices', where Dim=2, Lag =10, and consist 32768 samples, sampling rate was 2^{16}.

Table 3.

Name of signal	Approximate Entropy	N samples
data126	1,8837	(1:32768)
data126	1,9942	(32768:65535)
…	1.7058	(65536:98303)
…	1.8591	(98304:131071);

…	1,9740	(131072:163839)
…	1.8214	(163840:196607);
…	1.8035	(196608:229375);
..	1.3154	(229376:262143);
data126	1.1135	(262144:294911)

The likelihood that similar patterns of observations are not followed by additional similar observations corresponds to a higher value of approximate entropy.

3. CONCLUSION AND FUTURE RESEARCH

It was demonstrated that the statistics of fluctuations’ unpredictability of a specific acoustic signal can be evaluated using approximate entropy.

An ApEn was calculated in MatLab for some parts of the signal or “time slices”, that were cut from the initial studied signal.

As a result of these ApEn calculations, the values of ApEn are increasing when there is a decrease of the ratio signal/noise, for empirical acoustic data.

It should be noted that in case of pulse signals or of signals containing strong harmonics, the ApEn variations show an unpredictability in the changes of the signal’s fluctuations.

ACKNOWLEDGEMENTS

We would like to thank our colleagues from dep. of CIS prof. Tihomir Trifonov, prof. Dimiter Tsvetkov, eng. Kabakchiev from Vasil Levski National Military University for their collaboration. We would also like to extend my thanks to doctor Georgi Dimkov from the Institute of mathematics, Bulgarian academy of sciences for their collaboration and for providing the hardware PULSE.

References

[1] Simeonov, I.; Trifonov, T.; Georgieva-Trifonova, T., Signal Processing and Storing of High Dynamic Range Acoustic Data for Knowledge Discovery, Proc. of 14th International Conference on Communications, Electromagnetics and Medical Applications CEMA’19, Sofia, Bulgaria, October 17th-19th, 2019, pp. 58-62, ISSN: 1314-2100.

[2] Simeonov I., An Analysis of Uncertainty and Statistics of High Dynamic Range Acoustic Signals, Proc. of 15th International Conference on Communications, Electromagnetics and Medical Applications CEMA’21, Athens, Greece, October 21st, 2021, pp. 10-14, ISSN: 1314-2100.

[3] Simeonov, I., An Uncertainty and Mutual Information of Acoustic Signals with High Dynamics, Proc. of 17th International Conference on Communications, Electromagnetics and Medical Applications CEMA’23, Athens, Greece, November 3rd, 2023, pp. 40-43

[4] Simeonov, I., Entropy level estimations of real-world acoustic data, Proc. of 18th International Conference on Communications, Electromagnetics and Medical Applications CEMA’24, Sofia, Bulgaria, October 21st, 2024, pp. 11-15, ISSN: 1314-2100.

[5] Verdú, S. Empirical estimation of information measures: a literature guide. Entropy 2019, 21, 720. https://doi.org/10.3390/e210.

[6] Tsvetkov, Dimiter & Angelova-Slavova, Ralitsa. (2020). Positive periodic solutions for periodic predator-prey systems of Leslie-Gower or Holling-Tanner type. Nonlinear Studies, 27(4), pp. 991–1002., https://arxiv.org/abs/2008.01530

[7] Zbili M and Rama S (2021) A Quick and Easy Way to Estimate Entropy and Mutual Information for Neuroscience. Front. Neuroinform. 15:596443. doi: 10.3389/fninf.2021.596443.

[8] Hamadneh, T.; Abbes, A.; Abu Falahah, I.; AL-Khassawneh, Y.A.; Heilat, A.S.; Al-Husban, A.; Ouannas, A. Complexity and Chaos Analysis for Two-Dimensional Discrete-Time Predator–Prey Leslie–Gower Model with Fractional Orders. Axioms 2023, 12, 561. https://doi.org/10.3390/axioms12060561

[9] Pincus, S. M.; Gladstone, I. M.; Ehrenkranz, R. A. (1991). A regularity statistic for medical data analysis. Journal of Clinical Monitoring and Computing. 7 (4): 335–345. doi:10.1007/BF01619355.

[10] Pincus, Steven M. Approximate entropy as a measure of system complexity. Proceedings of the National Academy of Sciences. 1991 88 (6) 2297-2301; doi:10.1073/pnas.88.6.2297.

[11] Yordanov N., Noise characteristics in tactical trainings, Proc. Annual University Scientific Conf., Vol. 9, 2021, Veliko Tarnovo, National Military University Press, Bulgaria, pp. 182-191 (in Bulgarian), ISSN 1314-1937.

[12] Delgado-Bonal, A., Marshak, A., Yang, Y. et al. Analyzing changes in the complexity of climate in the last four decades using MERRA-2 radiation data. Sci Rep 10, 922 (2020). https://doi.org/10.1038/s41598-020-57917-8.

PROCESSING OF ACOUSTIC INFORMATION, CAPTURED IN A CLOSED ROOM VIA WIRELESS ACOUSTIC SENSOR NETWORK

Kostadin Panchev, Snezhana Georgieva Pleshkova

Technical University of Sofia, Faculty of Telecommunications
1000 Sofia, 8 Kl. Ohridski Blvd
snegpl@tu-sofia.bg

Abstract

There are many ways to process acoustic information using open-source programs, different software products etc. More specifically this paper is about acoustic information processing, captured in a closed room via wireless acoustic sensor network. For this goal it is proposed to use Python programming language with appropriates Python libraries to develop programming application for processing acoustic information. The most important acoustic information parameters are chosen included as corresponding program modules and the experimental results from their calculations are presented and commented in conclusion.

Keywords – acoustic information, wireless acoustic sensor network, ADSR Envelope, reverberation time and echo.

1. INTRODUCTION

Acoustic signal processing is focused on the acquisition, analysis, and manipulation of sound signals to extract meaningful information, to enhance auditory experiences and to be used in broad spectrum of applications, including speech recognition, audio enhancement, environmental monitoring, and bioacoustics studies. The MEMS microphones, have led to the development of compact arrays that facilitate innovative methods for sound field analysis and rendering. These advancements have expanded the scope of acoustic signal processing applications, enabling more precise sound capture and manipulation [1]. Machine learning of acoustic information processing have been applied and demonstrating compelling results and significant future promise [2]. Bio mimicry-inspired designs of acoustic met materials are developed by mimicking the biomechanical properties of biological hearing systems, leading to innovations in acoustic material design [3]. Therefore, the scope of this article is to propose and develop programming application for processing acoustic information, using Python programming language with appropriates Python libraries and to demonstrate the experimental results from the chosen and calculated acoustic information parameters, presented and commented in conclusion.

2. GENERAL DESCRIPTION OF THE DEVELOPED BLOCK DIAGRAMS OF PROCESSING OF ACOUSTIC INFORMATION, CAPTURED IN A CLOSED ROOM VIA WIRELESS ACOUSTIC SENSOR NETWORK

In Figure 1 are shown the following stages in one acoustic sensor network:

- the acoustic sensors node capturing the audio information and saving as WAV files;
- the wireless acoustic sensor node transferring the audio files to the acoustic server node via Wi-Fi Network;
- processing the WAV files with open source software for audio and giving the results as graphics and some acoustic parameters.

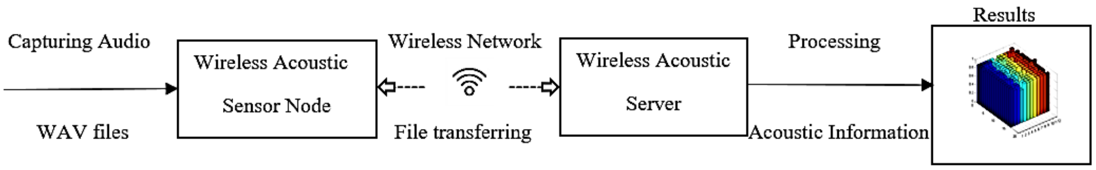

Fig. 1. Block scheme of acoustic sensor network for acoustic measurements in closed rooms

In the following part of this article, it is described the entire process of the acoustic signal processing, together with the reasons for using the relevant programming language.

3. PROCESSING OF ACOUSTIC INFORMATION, CAPTURED IN A CLOSED ROOM VIA WIRELESS ACOUSTIC SENSOR NETWORK

The described in Figure 1 entire process of the acoustic signal processing is proposed to be realized using the Python programming language both as a wide spread general-purpose programming language and also containing a lot of libraries [4,5], suitable for processing acoustic signals like: NumPy; Py dub; SciPy; Wave; Contextlib; the Matplotlib and Mpl_toolkits [6]. With the mentioned above libraries is created the appropriate program application to calculate the following acoustic parameters from the set of acoustic signals, captured via wireless acoustic sensor network in a closed room: duration; loudness; noise levels; pitch; wavelength; velocity; ADSR Envelope (Attack Decay Sustain Release Envelope); reverberation time and echo [7].

Each of these, calculated after processing, acoustic parameters are basic and very important to carry out the appropriate analysis, to estimate and to correct for increasing the acoustic quality of acoustic situation in closed room from these captured via wireless acoustic sensor network of acoustic signals. For example, if the goal is to analyze the speech intelligibility, then the loudness, noise levels and pitch are more important in estimation and correction. In other cases, if the goal is to analyze the sounds of music, then the ADSR Envelope (Attack Decay Sustain Release Envelope), reverberation time and echo may be must be chosen and use as more important in analysis, estimation and correction of sound music quality. These statements have been confirmed through the conducted experimental studies of the proposed acoustic information processing to calculate acoustic parameters from the captured via wireless acoustic sensor network of acoustic signals in a chosen closed room.

4. EXPERIMENTAL RESULTS OF PROCESSING OF ACOUSTIC INFORMATION, CAPTURED IN A CLOSED ROOM VIA WIRELESS ACOUSTIC SENSOR NETWORK

The experimental studies of the processed acoustic information, captured in a closed room via wireless acoustic sensor network, are carried out as the following concrete example:

- the measurements to capture the acoustic information via wireless acoustic sensor network are conducted in a closed room;
- closed room dimensions are: length 12.7, width 8.6 and height 3.5 in meters and with the following existing types and numbers of objects in this room: tables 8 and chairs 16;
- as sound source is used a loudspeaker to reproduce from it the chosen test audio signal of an acoustic guitar recorded in audio file on wave audio format.

It can be mentioned, that it is possible to change the choice of the test audio signals according to the concrete task of room acoustic measurements, analysis and room acoustic quality correction [8].

The visual view of table's (Desks) placement in the measured acoustic information on closed room and the corresponding positions of the wireless network acoustics sensors (ASN) on the tables is presented in Figure 2.

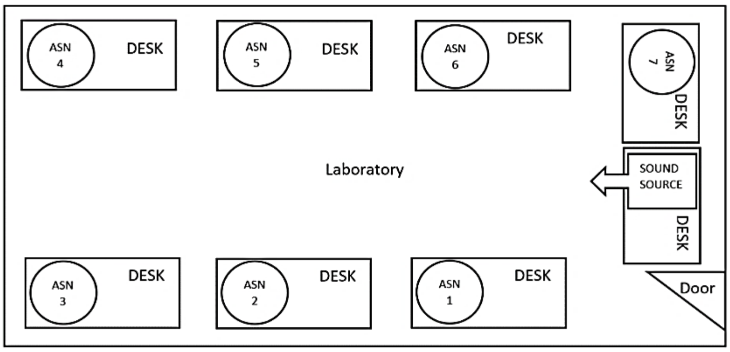

Fig. 2. Block scheme of the experimental staging for capturing the audio signals in a closed room, via wireless acoustic sensor network

With the proposed in Figure 2 block scheme of experimental staging are conducted a lot of measurements for capturing the audio signals in the chosen closed room. Each of the captured audio signal is transferred via wireless acoustic sensor network and all captured audio signals are collected in the wireless acoustic server, shown in Figure 1, as a set of captured audio signals (in this example six captured audio signals) in the chosen concrete closed room. The spectral characteristics of one of six (for this example) collected in wireless acoustic server captured audio signals are presented as amplitude-frequency characteristic in Figure 3 (left) and as 3D plot spectrogram in Figure 3 (right), respectively.

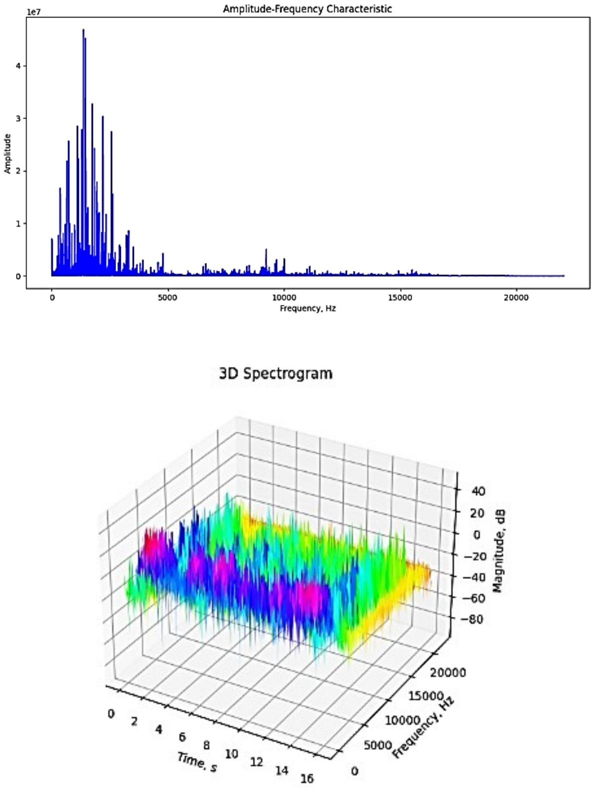

Fig.3. Amplitude-frequency characteristic (left) and 3D plot spectrogram (right) of one of the captured audio signals in a closed room, via wireless acoustic sensor network

For each of the captured acoustic parameters of the applied test audio record (test_file_path) in Python program application) are created the corresponding function in the Python program application and some more important from them are listed below:

- the function def N_LVL(test_file_path) for noise levels calculating;
- the function def PITCH(test_file_path) for pitch calculating;
- the function def ADSR(test_file_path) for calculating ADSR Envelope (Attack Decay Sustain Release Envelope);
- the function def RT60 (test_file_path) for calculating reverberation time.

First in the experimental studies, using the developed with Python program application, is executed the program module for capturing all audio signals (in this example six captured audio signals), then they are sensed to wireless acoustic server where they are collected as corresponding audio files in WAVE format. After that, is started the program module for calculating the acoustic parameters of each six captured audio signals.

After the execution of all the developed with Python program application, are achieved the results from the processing of the captured audio signals (in this example six captured audio signals), collected as a set in the wireless acoustic server.

The experimental results of processing of acoustic information (six captured audio signals from acoustic guitar record in audio file on wave audio format), captured in a closed room via wireless acoustic sensor network are briefly represented in Figure 4 only for one of the captured and processed in this example six audio signals send to the wireless acoustic server.

The achieved experimental results, shown and listed in Figure 6 for the calculated acoustic parameters for one of the captured in this example six audio signals send to the wireless acoustic server can be comment as follow:

- each of the mentioned above important for room acoustic analysis acoustic parameters like: duration, loudness, noise levels, pitch, wavelength, velocity, ADSR Envelope (Attack Decay Sustain Release Envelope), reverberation time and echo are calculated with the appropriate accuracy;
- these calculated acoustic parameters can be used as a suitable and sufficient acoustic information set to carry out a relevant analysis, estimation and correction of sound speech or music quality, depending to the concrete task.

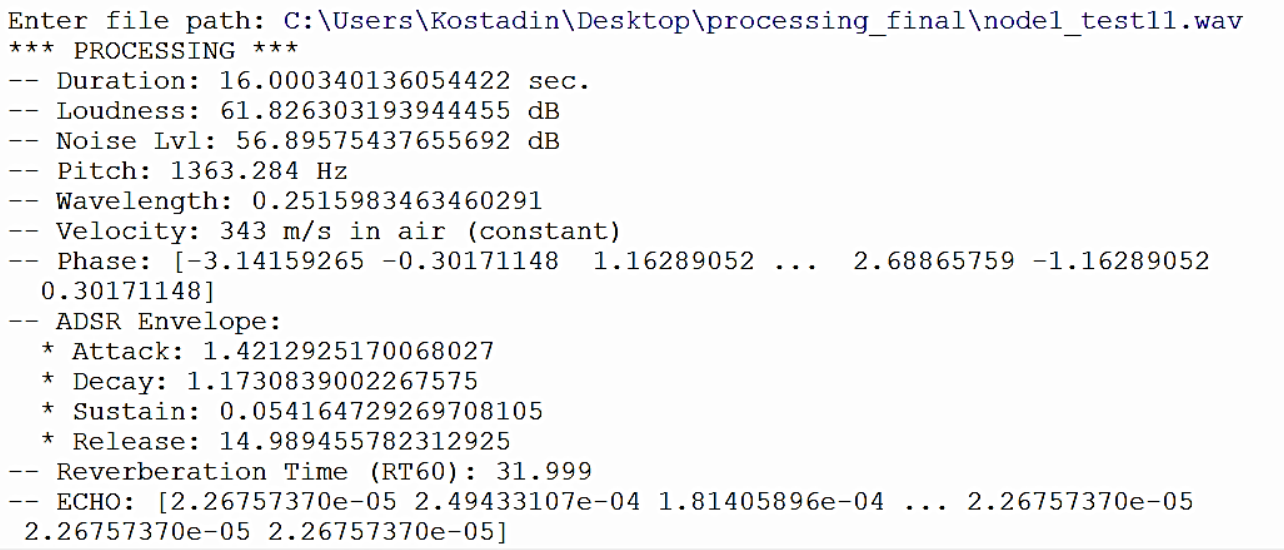

```
Enter file path: C:\Users\Kostadin\Desktop\processing_final\node1_test11.wav
*** PROCESSING ***
-- Duration: 16.000340136054422 sec.
-- Loudness: 61.826303193944455 dB
-- Noise Lvl: 56.89575437655692 dB
-- Pitch: 1363.284 Hz
-- Wavelength: 0.2515983463460291
-- Velocity: 343 m/s in air (constant)
-- Phase: [-3.14159265 -0.30171148  1.16289052 ...  2.68865759 -1.16289052
  0.30171148]
-- ADSR Envelope:
  * Attack: 1.4212925170068027
  * Decay: 1.1730839002267575
  * Sustain: 0.054164729269708105
  * Release: 14.989455782312925
-- Reverberation Time (RT60): 31.999
-- ECHO: [2.26757370e-05 2.49433107e-04 1.81405896e-04 ... 2.26757370e-05
 2.26757370e-05 2.26757370e-05]
```

Fig.4. Experimental results from the processing of acoustic information for one of the captured in this example six audio signals send to the wireless acoustic server

5. CONCLUSION

In conclusion, it could be said that the set objective of the present development has been fulfilled. The processing of acoustic information, captured in a closed room, via wireless acoustic sensor network can be done, work precise and quickly with the developed program application using Python programming language. It successfully calculates and draw for visualization the acoustic parameters of the acoustic information, captured in a closed room, via wireless acoustic sensor network. Understanding and analyzing these acoustic parameters and their measurement techniques is very important for room acoustics optimization and better acoustic environments designing with advancing sound-related technologies.

Based on the results obtained from the development and scientific research discussed in this article, is possible, in next researches, to continue with artificial intelligence analyze of the achieved acoustics characteristics for closed room acoustics quality estimation and also to use the developed Python program application in virtual reality room acoustic simulations or in real room acoustic designs.

ACKNOWLEDGMENT

The authors would like to gratefully acknowledge the Research and Development Sector at the Technical University of Sofia for the financial support.

References

[1] Giampiccolo, R.; Bernardini, A.; Massi, O.; Sarti, A. On the Virtualization of Audio Transducers. Sensors 2023, 23, 5258.

[2] S. Chandrakala, S.L. Jayalakshmi, Environmental audio scene and sound event recognition for autonomous surveillance. ACM Comput. Surv. (CSUR) 52, 1–34 (2020)

[3] Saniie, Jafar, Kupnik, Mario, Oruklu, Erdal, Advances in Acoustic Sensing, Imaging, and Signal Processing, Advances in Acoustics and Vibration, 2012, 901547, 2 pages, 2012.

[4] John Glover, Victor Lazzarini and Joseph Timoney, Python For Audio Signal Processing. Linux Audio Conference 2011.

[5] Guido van Rossum and Fred L. Drake. 2006. Python Language Reference Manual. Network Theory Limited, Bristol, UK.

[6] Doug Hellmann, Python 3 Standard Library by Example, The (Developer's Library), June 2017.

[7] Glen Ballou, Handbook for Sound Engineers, 4th Edition, October 2008.

[8] Test Solution for Room Acoustics. https://www.nti-audio.com/en/applications/room-building-acoustics/room-acoustics/solutions

ELABORATING A 3D BLUEPRINT OF A CONVEYOR AND ITS APPLICATION IN INDUSTRIAL COMMUNICATION NETWORKS

Daniel Denev, Silvia Nikolova, Tsvetoslav Tsankov

Faculty of Technical Sciences, Konstantin Preslavsky University of Shumen, Bulgaria
d.denev@shu.bg, silvia_nikolova73@abv.bg, c.cankov@shu.bg

Abstract

The research addresses the challenge of integrating and optimizing communication at the Field level of industrial networks that manage multiple conveyors. The proposed solution includes virtual modeling and real-time simulation using TIA Portal and Factory I/O software. The author contributes by developing and testing a digital twin of a conveyor-based system with a focus on network reliability under fast-routing conditions. The principal results indicate that such systems, when virtually tested, demonstrate improved performance and reduced susceptibility to operational faults, providing a viable strategy for early-stage validation and optimization in automated industrial environments.

1. INTRODUCTION

In light of industrial advancement, the establishment of production facilities emerges as a paramount objective for companies. The growing trend of automating industrial processes, coupled with the necessity for effective communication networks, underscores the significance of this research. By optimizing the field level of industrial communication networks, there is potential for substantial improvements in operational efficiency. Accordingly, this research endeavors to concentrate on enhancing the Field level of industrial communication networks, which interface with a diverse array of machinery. This emphasis on the Field level specifically targets the integration of conveyors within the industrial communication network. This selection is rationalized by the increasing reliance of companies on expeditious information processing concerning the production process. Analogously, the imperative questions surrounding this endeavor include inquiries into the optimal utilization of such networks and their resultant financial implications. This study primarily aims to create a virtual model of an industrial communication network that incorporates conveyors, thereby offering a well-structured and optimized solution for organizations pursuing greater automation. The principal aim of this developmental endeavor is to furnish companies with a preconfigured network designed to address their primary concerns effectively [4]. A preliminary measure involves the creation of a virtual model of conveyors intended for utilization within a company, constituting the foundational tier of the industrial communication network. The realization of this visualization and conceptual construction will be facilitated through the utilization of 3D design software, notably FACTORY I/O.

Advancements in time and technology have led to the creation of numerous novel devices, among which are the latest iterations of 3D Machine software. Initially employed solely for drafting purposes with limited 2D capabilities, these software programs have evolved over time to meet growing demands. Presently, they maintain their primary function in design while catering to both avid enthusiasts and average users. Enthusiastic users, including engineers, utilize these tools to construct virtual machinery and oversee their operational processes. A thorough review of the existing literature sheds light on prior research endeavors in this area, facilitating a comparative evaluation of various methodologies related to industrial communication and automation. This investigation delves into earlier research endeavors by various scholars. Ivanka Georgieva, in her publication "Automation Systems with Programmable Logic Controllers," delineates optimal strategies for harnessing the potential of 3D Software, drawing from her own expertise to guide researchers and standard users towards maximizing the efficacy of automation systems. Additionally, Emilio Tudoreanu explores the development of Designing Effective Program Visualization Tools aimed at reducing users' cognitive load, while Ji Yan, hailing from Utah State University, contributes to the discourse with insights into 3D Visualization Software. The exploration culminates in Mitchel Alspaugh's examination of design principles and clandestine methodologies in conveyor implementation. Additionally, an examination of supplementary sources, including recent investigations into industrial automation frameworks and communication protocols, will contribute to a well-rounded understanding of the progress made in this field.

2. MATERIALS AND METHODS

Factory I/O is a 3D simulation software designed to facilitate the testing of models developed on STEP7, while also providing a visual representation of the operational environment of an industry incorporating a comprehensive array of machinery.

TABLE 1.
Essential Specifications Needed by a Computer to Execute the Software Program

Hardware	Requirements
CPU	AMD FX – 2.8GHz, similar or more powerful
RAM	4 GB
HDD space	3 GB hard disk for Local Disk C
Operating system	Mac OS
	Windows 7
	Windows 8
	Windows 10
Graphic card	4GB VRAM or more powerful
	256-bit graphics bus or more powerful

Notably, the key strength of this software lies in its compatibility with a wide range of Siemens controllers. The software boasts an extensive library containing a diverse assortment of industrial components, enabling users to construct multiple 3D devices creatively. Upon acquisition and licensing of the software package, users are furnished with several preconfigured scenes tailored for beginners entering the program [3], [9].

To initiate the program's construction, launch TIA Portal v13 and access the taskbar. Choose "Create new project" to establish a fresh project. Select a name for the project, choose a location for the repository, and click on the Create button. As a consequence, the process of creating the project is triggered, followed by the configuration of the other devices by pressing the Config Device button [3]. When this option is selected, a modified dialogue box is displayed, and in this box you are allowed to select Add new device for the purpose of adding a new device. This process is shown in Figure 1.

A diverse array of processors is accessible for the selection of devices. Presently, the unspecified CPU 1200 in version 4.1 is being chosen. Upon selection the CPU is depicted in the workspace as a blank entity. Simultaneously, the "Detect" button becomes available, which upon activation initiates the detection process for the processor. Subsequently a new window emerges, facilitating the discovery of the requisite controller within the network through the utilization of the "Start Search" function. Upon selecting and activating the "Detect" button, the program establishes a connection with the controller, retrieving pertinent information regarding both the controller and its associated blocks. Following the successful establishment of the connection the controller manifests within the workspace, as exemplified in Figure 2.

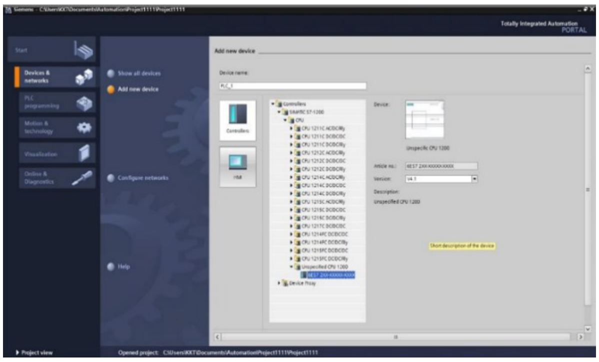

Figure 1. Add a new device

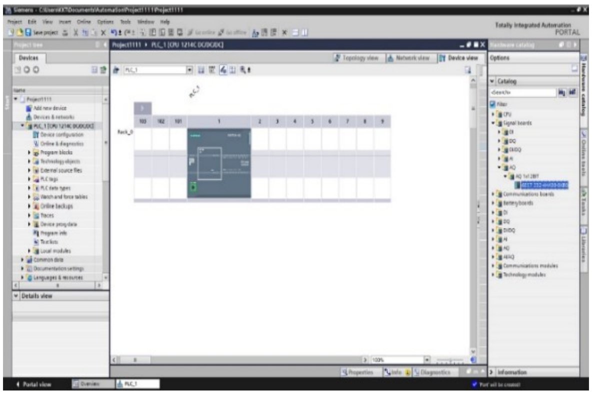

Figure 2. Programmable Logic Controller Processing Unit

Once the controller is initialized, the next step involves constructing the electrical and control circuit, facilitated through the project navigator interface. Within this interface the controller's processor is selected, and the "Main (OBI)" option is chosen from its dropdown menu within the Program blocks subsection. By default, the circuit construction begins in Network 1 with the option to utilize multiple networks depending on the complexity of each circuit. The programming language employed is the default Ladder Diagram (LAD). Components are placed onto the workspace by selecting them from the "FAVORITE" category and clicking within the designated area.

During circuit construction, it may be necessary to create parallel connections for certain elements. A specific example is the construction of timers, which involves utilizing the "Create box" function and subsequently configuring its parameters by right-clicking on the element. Once opened, the parameters allow for complete customization and transformation of the element. The desired Timer On-Delay (TOF) timer is selected and automatically placed within the circuit. This process effectively utilizes the distributive law, which plays a critical role in simplifying logical elements within the TIA Portal environment. Complex equations involving 8 logic operations can be condensed to just 4, as demonstrated in the equations provided below.

$$\alpha_2 /(\alpha_2 - \gamma_2) = (\alpha_2/\beta_2) - (\alpha_2/\gamma_2)$$

$$\alpha_2 - (\alpha_2/ \gamma_2) = (\alpha_2 - \beta_2)/(\alpha_2 - \gamma_2)$$

$$\alpha^2 * (\alpha^2 + \gamma^2) = (\alpha^2 * \beta^2) + (\alpha^2 * \gamma^2)$$

$$\alpha^2 + (\alpha^2 * \gamma^2) = (\alpha^2 + \beta^2) * (\alpha^2 + \gamma^2) \quad (1)$$

Before proceeding with the design, it is crucial to establish the program table configuration, which verifies the readiness of the devices to perform the operations.

```
Program Table per One Device;

…

OneDevice.InputRegister (0x0100B879, 0x80000000);

OnelDevice.CheckRegister (0x0100B879, 0x80004005);

OneDevice.CheckRegister (0x0100B879, 0x80010000);

OneDevice.WriteRegister (0x0100B879, 0x80020001);

OneDevice.WriteRegister (0x0100B879, 0x80030001);

OneDevice.WriteRegister (0x0100B879, 0x80041010);

OneDevice.WriteRegister (0x0100B879, 0x80050101);

OneDevice.WriteRegister (0x0100B879, 0x80060000);

OneDevice.WriteRegister (0x0100B879, 0x80070000);

OneDevice.CheckRegister (0x0100B879, 0x80080401);

OneDevice.CheckRegister (0x0100B879, 0x80090401);

…

OneDevice.OutputRegister (0x0100B874, 0xA0FF0001);
```

Following the construction of the circuit and the verification of the program table configuration the next step involves setting values and adjusting tags. Tag adjustment is a crucial aspect that enhances the connectivity of the circuit and facilitates better visualization [2], [8]. This adjustment process is conducted through the project navigator interface. Within the PLC Tags option and the "Show all tags" function is selected, enabling the modification of tag names and values as required. Inputs are typically designated as %I followed by a numeric identifier, while outputs are labeled as %Q followed by a numeric identifier. Upon completion of these adjustments, the circuit adopts the characteristics illustrated in Figure 3.

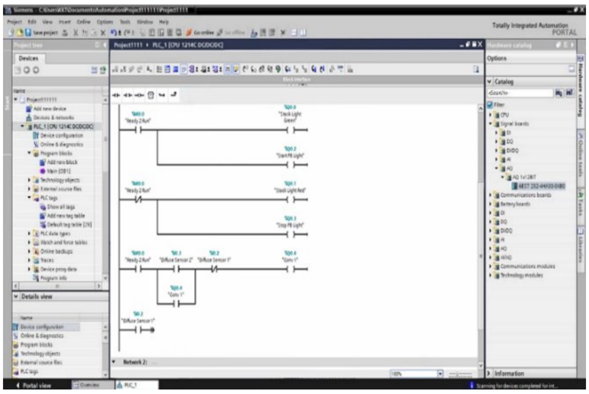

Figure 3. Final diagram

We have now reached the stage where we need to verify the construction and the set values. This verification process is initiated by using the Compile function. To access it navigate to the project navigator, right-click on the processor of the controller (PLC_1) and a list of options will appear, among which is Compile. Upon selecting Compile, several options will become available with Hardware (rebuild all) and Software (rebuild all blocks) being essential selections. Once the compilation process is complete and it's confirmed that the construction is correct, the next step is to proceed with the Download to device operation [1], [10]. This operation facilitates the transfer of the completed program, constructed earlier, to the hardware device of the system, as depicted in Figure 4.

Computational Thesis for data Transfer: The optimal integer solution for transferring the task from PC to PLC is as follows:

$$\varepsilon' = \begin{cases} [\epsilon^0], or\ f([\varepsilon^0]) \leq f([\epsilon^0]) \\ [\epsilon^0]\ otherwise \end{cases} \quad (2)$$

Proof: $f\ (\epsilon)$ is monotonically decreasing when $\epsilon < \epsilon'$; It is monotonically increasing when

$\epsilon > \epsilon'$.. Thus ϵ' gives a minimally fast solution. Let's consider the transfer equation (2).

$$\frac{min}{\epsilon} J(\epsilon) \triangleq [T^0 + (d+PL)/\rho](1-\delta)^{-(d+\varepsilon L)}.N/\epsilon T^0 + \frac{d+\epsilon L}{\rho} \leq T^R, \rho \, \epsilon \, \{1,2,\dots.,N\} \quad (3)$$

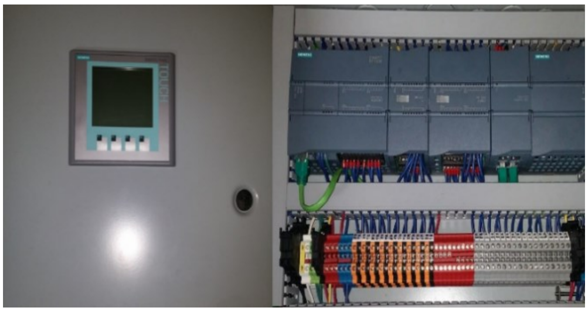

Figure 4. Hardware system with controller

Evidently the objective function does not adhere strictly to mathematical formulation, owing to the aforementioned factors, rendering the attainment of optimality via conventional transmission of data packets. Nonetheless, analytically the solution frequently satisfies the criteria for application in engineering practice. Let us delve into the pertinent issue concerning unrestricted information transfer:

$$\frac{min}{\epsilon} f(\epsilon) \triangleq [T^0 + (d+\epsilon L)/\rho](1-\delta)^{-(d+\epsilon L)}.N/\epsilon \quad (4)$$

By calculating the derivative:

$$\varepsilon^0 = \frac{1}{2L}[-(d+T^0\rho) + +\sqrt{(d+T^0\rho)^2 + 4(d+T^0\rho)L/In^{-L}(1-\delta)}] \quad (5)$$

All local minima for the speed function in $[P'_U, P'_L]$ are shown as:

$$\bar{D} \triangleq \left\{ \frac{N}{\lceil \frac{N}{P} \rceil} | P \in \{P'_L, \dots, P'_U\} \right\} \quad (6)$$

If N is a prime number according to (6), the target $J(P)$ in relation to $N+1$ is considered alternatively within $[2, N+1]$. Therefore, monotony is not guaranteed in limits 1 and N. Let us review:

$$\bar{D} \triangleq \left\{ \frac{N}{\lceil \frac{N}{P} \rceil} | P \in \{P'_L, \dots, P'_U\} \right\} \cup \{1, N\} \quad (7)$$

An optimal solution can be created so the transfer of programs and information can be improved.

3. RESULTS AND DISCUSSION

Upon completion of the construction process, the visualization stage commences. Activating the Factory I/O program initiates the creation of a new project by selecting the "New Project" option from the menu. Notably, the initial impression of the program's interface diverges from conventional visualization displays, transitioning into a 3D representation of a workshop or room environment. Within this environment, the compiled model is visualized in a three-dimensional format, providing a realistic depiction of its appearance under actual conditions. To construct the model, users navigate to the "All" drop-down menu, offering a diverse array of libraries containing construction elements. Specifically, the "Stations" library is accessed to locate the desired pipeline component, initially connected to its platform as a virtual pallet generator. To position the pipeline within the workspace, users simply click and drag it to the desired location, with the program allowing unrestricted placement. Subsequently, another essential component, namely the control panel, is positioned adjacent to the machine within the workspace. The visualization of buttons on the control panel is facilitated by accessing the "Operators" library, wherein two control buttons, signifying start and stop functions, are selected. Upon selection, users click and drag these buttons to their designated location, ensuring proximity to the control panel [5]. These buttons are automatically integrated into the panel through an automated function. During the creation of the visual program in Factory I/O, inputs and outputs for each subprogram are designated to their respective PLCs for allocation [7].

List of Inputs and Outputs:

I:1/0 = Start Input (Input)
N7:1 = X input to Cos function (Input)
N7:2 = Cos X operation data (Input)

N7:3 = Checking register transfer
(Checking)
N7:4 = Numeric Value "3" (To perform 3+Cos x)(Input)
N7:5 = Output of addition 3+Cos X (Input)
N7:6 = Square Root of 3+Cos X (Input)
N7:7 = Numeric Value "3" (To perform 3x) (Input)

N7:3 = Checking register second transfer
(Checking)
N7:8 = Output of Y to power X (3x) (Input)
N7:9 = Lower Limit (10) (Input)
N7:9 = Higher Limit (21) (Input)

N7:3 = Checking register third transfer

```
          (Checking)
O:6 = Output x, multiplication of N7:3 & N7:4     (Output)
O:4 = Output 0, multiplication of N7:3 & N7:6     (Output)
O:2 = Output x, multiplication of N7:3 & N7:8     (Output)
O:0 = Output 0
```

After the performed actions the visualized model takes the form from Figure 5. Each machine and device are created separately. To work in the production line, they are arranged in the appropriate order and then is used the Merge function. This function merges the conveyors. Each conveyor has its own PLC which is responsible for control and Factory I/O extracts these operations and simulates the work process. Based on the development, simulation tests were performed out during the work of the field level and the information process was observed. Mainly the response of the communication network and the processing input data was monitored [6]. The good data processing is due to the implementation of optimized packet technology and new Roughing Scheme. This information and the parameters of the packets and routing schemes are shown in Table 2.

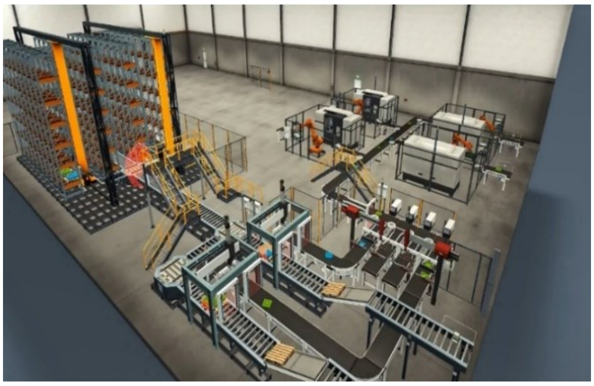

Figure 5. 3D Field level with conveyors

TABLE 2.
Simulation System Parameters Concerning the Field Level's Performance in Correlation With the Network's Information Response by All the Conveyors

Simulation system parameters	**Test 1**	**Test 2**
Additional access time	4 ms	4 ms
Retransmission speed	10^{-8}	10^{-8}
Network bandwidth	150 k	150 k
The total number of subnets	80	80
The upper limit of the time to refresh a package	100 ms	100 ms
The optimized package size	10	5
Optimized number of packages	4	7
Actual processing time per package	30.0	22.3

In operation when the conveyors work in a pipeline system the sample code shown below runs in Factory I/O [11]:

```
<Program>
 <Routine Name=FB “1“ “Type=“Function Block(FB)“>
…
 <Routine Name=FB “4“ “Type=“Function Block(FB)“>
 <Rung Number=“1“>
/ Initializing Registry Entries
 <Type=“MOVE “Source_Value=“%I0.0“ Tar-
get_Address=“%Q0.1“>
 <Condition Type=“AND“ Address=“%Q0.7“/>
 <Input Type=“MOVE“ Source_Value=“%I0.3“ Tar-
get_Address=“%Q0.5“>
 <Input Type=“SET INPUT PROCESS“ Source_Value=“%I0.2“
Address=“%Q0.5“>
 <Input Type=“MOVE“ Source_Value=“%I0.7“ Tar-
get_Address=“%Q0.3“>
 <Input Type=“SET INPUT PROCESS“ Address=“%Q0.4“>
 <Input Type=“CONVERT INPUT INTEGER“
Source_Value=“%I0.2“>
 <Input Type=“TURN RIGHT“ Source_Value=“%I0.1“>
 <Input Type=“TURN LEFT“ Source_Value=“%I0.1“>
 <Input Type=“MOVE FORWARD“ Source_Value=“%I0.1“>
Target_Address=“%Q0.6“>
 <Input Type=“ADD INPUT INTEGER“ First_Input=“%I0.6“
Second_Input=“%Q0.4“ Target_Address=“%Q0.7 “>
 <Rung Number=“2“>
/ Initializing the Register Outputs
 <Type=“MOVE“ Source_Value=“%Q0.3 “ Tar-
get_Address=“%Q0.3“>
 <Output Type=“MOVE“ Source_Value=“%Q0.4“ Tar-
get_Address=“%Q0.4“>
 <Output Type=“OUTPUT PROCESS“
Source_Value=“%Q0.6“ Address=“%Q0.1“>
 <Output Type=“MOVE“ Source_Value=“%Q0.2“ Tar-
get_Address=“%Q0.0“>
 <Output Type=“OUTPUT PROCESS“
Source_Value=“%Q0.5“ Address=“%Q0.6“>
 <Output Type=“SET PROCESS“ Address=“%Q0.5“>
 <Output Type=“CONVERT INTEGER“
Source_Value=“%Q0.3“ Target_Address=“%Q0.4“>
 < Output Type=“TURN RIGHT“ Source_Value=“%I0.1“ Tar-
get_Address=“%Q0.1“>
 < Output Type=“TURN LEFT“ Source_Value=“%I0.1“ Tar-
get_Address=“%Q0.2“>
 < Output Type=“MOVE FORWARD“ Source_Value=“%I0.1“
Target_Address=“%Q0.3“>
 <Rung Number=“3“>
/ Initial Load of Registers to Accept New Input Data
 <Type=“ADD INTEGER“ First_Input=“%I0.1“ Se-
cond_Input=“%I0.3“> Target_Address=“%Q0.5 “>
 <Output Type=“RESET PROCESS“ Address=“%Q0.5“>
…
 <Rung Number=“4“>
 <Routine Name=FB “4“ “Type=“Function Block(FB)“>
…
 <Routine Name=FB “4“ “Type=“Function Block(FB)“>
```

The real-time outcomes depict the lower limit function denoted as F(P) and the optimized packet size characterized by the sawtooth function J(P) in relation to the two experiments, as delineated in the subsequent figures. It is observed that F(P) exhibits convex behavior, whereas J(P) displays nonlinearity and non-convexity, rendering the mathematical determination of the optimal packet size for the network information response. For instance, considering the Test from Figure 6, the global minimum for the convex and unbounded function F(P) is identified as 13, as depicted in the figure. However, the optimized packet size must be selected from the candidate sets of packets with local minima {1,2,11,13,20}, and the optimal solution necessitates validation, which is illustrated in Figure 6.

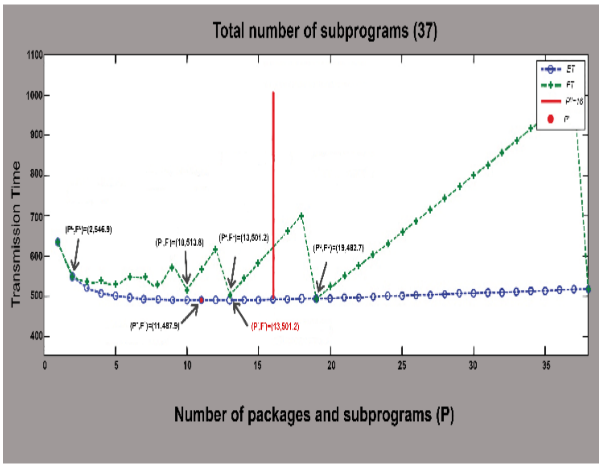

Figure 6. Optimal solution for trouble-free operation with 37 subprograms

It is important to say that with the conveyors and the implemented routing scheme, the field level of each factory in the industry will produce more products in a shorter period of time.

The general statistics Figure 7 show the result after discovering the optimal number of hops with packets which are needed for faster and better information processing.

The best result shows that this is an uneven number of hops and an uneven number of packets. This shows that this type of algorithm is one of the most efficient and would find wide application in the future in industrial networks.

The current research addresses a groundbreaking subject regarding the design of a 3D field level within an industrial network, utilizing state-of-the-art software technology that is at the forefront of innovation. In the existing literature, there has been a notable lack of attention directed towards innovative topics and emerging techniques. Specifically, the exploration of 3D software for designing elements or machinery has been relatively underexplored, with a predominant reliance on traditional techniques from previous generations. This study reaffirms qualitative findings established by prior researchers and identifies existing gaps in the design of elements. Moreover, it highlights the growing popularity of 3D visualization, which is gradually supplanting conventional hand-drawn designs. The utilization of Factory I/O, an innovative software solution, extends beyond the mere design of elements and machines, aiding engineers in virtual machine monitoring and operational analysis. Through this investigation, we further demonstrate the substantial discrepancies between different design methods in terms of both efficacy and quality.

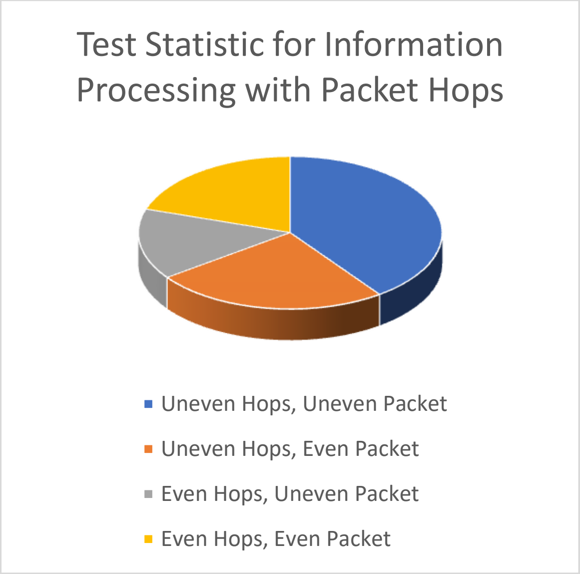

Figure 7. Full Test Result Chart

4. CONCLUSION

This paper introduces a progressive theme concerning the design of a 3D field level within an industrial network. The creation of this network utilizes the TIA Portal software, while visualization is facilitated through the adoption of Factory I/O, a state-of-the-art software solution. The application and benefits of this innovative software are extensively deliberated, highlighting its utility not only in designing components and machinery but also as a tool for machine monitoring and virtual testing of machine operations. The research results demonstrate that the adoption of a virtualized 3D field level markedly improves system adaptability and diminishes the likelihood of errors in industrial automation processes.

The realization of a 3D field level within the industrial communication network holds the potential to significantly benefit numerous companies across various industrial sectors. From a theoretical standpoint, this investigation adds to the existing dialogue on industrial automation by offering valuable insights into the fusion of virtual simulation tools with industrial communication networks. Our research serves as a foundation for future investigations, aiming to advance and explore additional innovative methodologies for designing new structures, machinery, and components. In practical applications, the proposed methodology can be utilized in manufacturing settings to enhance production workflows, optimize resource distribution, and reduce downtime. Its primary objective is to support individuals involved in designing and visualization endeavors by furnishing practical and theoretical insights into working with Programmable Logic Controllers. An upcoming objective entails the analysis and delineation of each sector within an industrial enterprise. Moreover, future research will aim to quantify the efficiency gains realized through 3D simulation in comparison to conventional HMI animation, thereby assisting industries in selecting the most appropriate strategy for their requirements.

ACKNOWLEDGMENTS

In this section, we would like to thank all of our loved ones for their support and motivation throughout the process of our scientific research. This publication is funded by the fund "Support for Publishing Publications in Journals with Impact Factor (IF) and Impact Rank (SJR)" of Konstantin Preslavsky University of Shumen, Republic of Bulgaria.

References

[1] X. Tang and Y. Jiang, *System PLC Programming and Debugging*, Chemical Industry Press, Beijing, 2017.

[2] X. W. Zhang, *Man Machine Interface Equipment and Portal Software Automation Engineering Software. Touch Screen Application Technology from Entry to Mastery*, Chemical Industry Press, Beijing, 2017.

[3] E. Tudoreanu, "Designing Effective Program Visualization Tools for Reducing User's Cognitive Effort," *Proc. ACM. Software Visualization*, 2003.

[4] I. Georgieva, *Automation Systems with Programmable Logic Controllers*, Sofia, 2016.

[5] A. Teyseyre and M. Campo, "An Overview of 3D Software Visualization," *IEEE Transactions on Visualization and Computer Graphics*, 2009.

[6] J. Yan, *An Evaluation of Current Applications of 3D Visualization Software in Landscape Architecture*, Utah State University, 2014.

[7] M. Alspaugh, "Latest Developments in Belt Conveyor Technology," Overland Conveyor Co., Inc., Presented at MINExpo, Las Vegas, NV, USA, September 27, 2004, pp. 1–11.

[8] L. Staneva and I. Vardeva, "Automated Design of Electronic Circuits Modeled with Generalized Networks," *International Scientific Conference "Education, Science, Economy, and Technology"*, Burgas, 2014.

[9] V. Mechkova, L. Staneva, and B. Mechkova, "Mathematical Model for Studying Transient Processes in a Second-Order Linear Electric Circuit," *International Scientific Conference "Education, Science, Economy, and Technology"*, vol. 2, Burgas, 2015.

[10] M. B. Uzun and V. T. Atanasov, "Program Management of Networks Through Models Based on NETCONF and RESTCONF Protocols," *Annual of Konstantin Preslavsky University of Shumen*, Konstantin Preslavsky University Press, vol. XIII E, 2023, pp. 124–131, ISSN 2815-4703.

[11] M. B. Uzun and V. T. Atanasov, "Common Conception of Software-Defined Networks," *Annual of Konstantin Preslavsky University of Shumen*, Konstantin Preslavsky University Press, vol. XIII E, 2023, pp. 112–119, ISSN 2815-4703.

COMPARATIVE ANALYSIS OF THE PERFORMANCE OF DEEP LEARNING-BASED AI FOR VIDEO CAMERAS WORKING WITH DIFFERENT DATABASES

Silvia Nikolova, Daniel Denev, Tsvetoslav Tsankov

Faculty of Technical Sciences, Konstantin Preslavsky University of Shumen, Bulgaria
silvia_nikolova73@abv.bg, d.denev@shu.bg, c.cankov@shu.bg

Abstract

The development of artificial intelligence (AI) for video cameras depends on the use of various database types, each serving specific data handling purposes. This paper addresses the challenge of optimizing AI functionality through appropriate database integration. The authors investigates how structured, unstructured, and real-time databases impact the training and performance of AI in robotic security systems. The principal contribution lies in a comparative analysis of system behavior in real-time conditions and physical environments. The results demonstrate that real-time databases significantly enhance responsiveness and accuracy, while structured and semi-structured formats support efficient data interpretation and learning. The study concludes with practical recommendations for selecting suitable database types to improve the effectiveness of intelligent video surveillance systems.

1. INTRODUCTION

Modern perimeter security systems combine physical security and access control with advanced technologies that complement and enhance their functionality, facilitate management, and ensure reliable operation. Thanks to the latest advances in sensors, video surveillance cameras, and security software, combined with innovations such as artificial intelligence and machine learning, perimeter security continues to be among the most sought-after solutions for ensuring the safety of various commercial, public, institutional, and industrial facilities [1].

In recent years, the field of artificial intelligence has advanced rapidly with applications in a wide range of fields, including video surveillance [2]. Video cameras are now equipped with databases for training artificial intelligence algorithms to recognize objects, behaviors, and patterns in real time. These databases are critical for improving the accuracy and efficiency of video surveillance systems, as well as enabling new capabilities such as object tracking, facial recognition, and anomaly detection [3]. By providing a large amount of labeled data, these databases allow algorithms to learn from examples and improve their performance over time. This can lead to more reliable and accurate detection of objects, activities, and events in real-world scenarios, enabling faster and more effective responses to security threats or emergencies.

Structured databases play a crucial role in effectively organizing data for training AI in video cameras [4]. These databases, which include well-known systems such as MySQL, PostgreSQL, and Microsoft SQL Server, are designed to handle structured data in a tabular format, which facilitates queries and information retrieval [5]. By using structured databases, developers can ensure that the data used to train AI models is well-organized and easily accessible. This organization is essential for tasks such as facial recognition, motion detection, and event classification in video surveillance systems. Furthermore, the structured nature of these databases allows for the implementation of complex queries and analytics, improving the training process and improving the performance of AI algorithms [6].

Unlike structured databases, unstructured databases are essential for managing raw video footage, which is often critical for training AI models in video cameras [7]. These databases store data that does not have a predefined schema, allowing for the flexibility needed to process different video formats and resolutions. Since AI systems often need access to vast amounts of unstructured data for tasks such as object detection and scene understanding, relying on unstructured databases can significantly improve the training process. For example, video footage can be ingested directly without requiring extensive pre-processing, allowing for faster iterations in model training. This adaptability is especially important in real-time applications where AI must learn from and respond to dynamic environments.

Cloud-based databases offer significant scalability and accessibility advantages for AI training in video cameras [7]. These databases allow for the storage and processing of huge volumes of data across multiple servers, which is critical given the vast amount of data generated by video surveillance systems. By leveraging cloud infrastructure, organizations can easily scale their storage solutions as their data requirements grow. Additionally, cloud-based databases provide the necessary accessibility for teams working remotely or in different locations, facilitating collaboration and ensuring that AI models can be trained on the most up-to-date data available. This flexibility not only streamlines the training process, but also supports the integration of machine learning and artificial intelligence tools that can analyze video data effectively and efficiently.

2. MATERIALS AND METHODS

For the purposes of this report, 3 video cameras operating in a real environment and trained with different types of databases were studied over time. The video cameras are part of the TEDI robotic security system [8]. The TEDI / Technological Electronic Digital Intelligent / security robotic security system completely eliminates physical security. The system includes elements of security alarm systems (SOT), video, thermal analysis and intelligent robotic decision-making shown on Figure 1. Artificial intelligence, combined with system algorithms, allows the system to be both a security guard and a dispatcher. The TEDI security robot has unique software developments for management and control of the entire security activity of the facilities, as well as for data collection, transmission and processing, including: IRIS – Intelligent Radio Information System and Smart SOT – Flexible, modular security service with technical means and mobile response forces.

Previous studies [9], [10] compared the advantages and disadvantages of machine learning and deep learning on convolutional neural networks used in CCTV cameras. The highest results, such as training time and efficiency, were received for video surveillance camera AI using convolutional neural networks. Therefore, this type of cameras was selected for the present study.

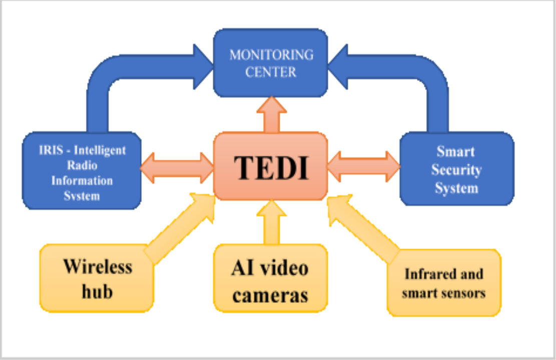

Figure 1. Scheme of TEDI's activities using AI video cameras

The cameras are 5MP IR Vari-focal Bullet WizMind Network; 2.7" CMOS image sensor, low luminance, and high definition image: with deep learning algorithm, it supports: video metadata, smart sound detection, IVS, face detection, smart object detection, and people counting, etc. These cameras use deep learning algorithms and work with back-end devices to accurately match targets, such as people, animals, and motor vehicles, and search live and recorded video to quickly locate targets. These parameters make them suitable for this study.

The cameras are part of the TEDI robotic system [8], located in different sites, on different terrains and at different altitudes. Subjected to different climatic conditions and violation of the perimeter by different animals and other intruders.

In order to exclude side effects on the results, before the start of the study, the reaction of the system was monitored without applying deep AI training, as well as operation at different temperatures for a week. The results were calculated with an efficiency factor (1).

$$K_{ef} = \frac{A_r}{A_g} \qquad (1)$$

where Ag – number of alarms generated by the camera in 48 hours. Ar – number of actual triggers in 48 hours.

The differences obtained in the efficiency coefficient of the systems, presented in Table 1, turned out to be negligibly small and are excluded as influencing factors.

For training the AI in video cameras, three types of databases were selected that are closest in qualitative composition to the goals of the system used. They include a rich set of visual objects.

TABLE 1.

Efficiency Coefficients for Untrained AI

Factors affecting the efficiency ratio	**Video camera 1 595 m altitude**	**Video camera 2 196 m altitude**	**Video camera 3 20 m altitude**
Temperature +20°C	0.4140	0.4432	0.4300
Temperature -18°C	0.4122	0.4420	0.4291
Rain	0.4049	0.4099	0.4189

COCO (Common Objects in Context) – object recognition database

Why is it good: Contains a wide variety of objects in real scenes with detailed annotations (bounding boxes, segmentation, key points).

Applications: Object recognition, segmentation, people detection.

Link: COCO Dataset

https://cocodataset.org/#home/

Open Images Dataset – object recognition database

Why is it good: Huge set of images with over 600 categories and annotations for objects, relationships between them and segmentation.

Applications: Computer vision, object recognition.

Link: Open Images

https://storage.googleapis.com/openimages/web/index.html

UCF101 – Video Analysis Database

Why is it good: Contains 13,320 videos with 101 action categories.

Applications: Action recognition, analysis.

Link: UCF101 Dataset
https://www.crcv.ucf.edu/data/UCF101.php/

The training itself took place remotely through an application for accessing the video camera software. The work proceeds through the following sequential stages (Figure 2).

Database entry – at this stage, the selected data is entered (Figure 3).

Evaluation of the results after 48 hours – by carefully reviewing the records, the number of events registered by the camera's AI and the number of actual events in the guarded area is recorded.

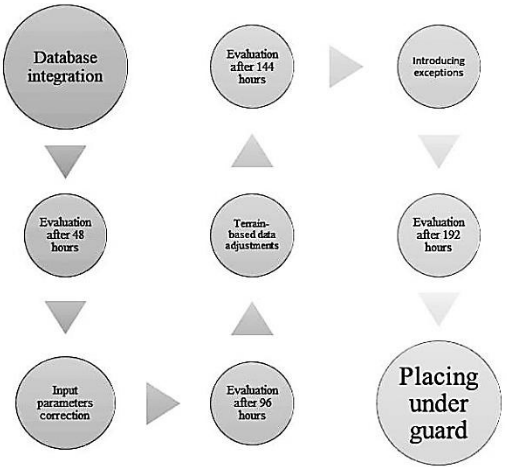

Figure 2. AI training sequence

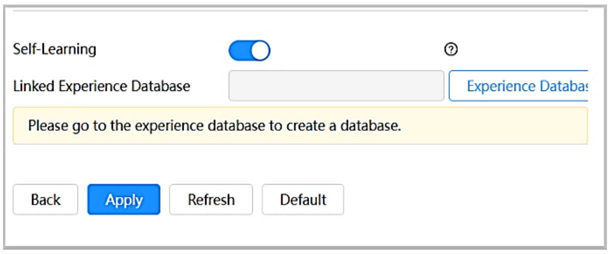

Please go to the experience database to create a database.

Figure 3. AI training sequence

Correction of the input parameters – depending on the reported results, the composition of the initially set database is changed quantitatively and qualitatively.

Evaluation of the results after 96 hours – the records are reviewed again to report the number of events registered by the camera's AI and the number of actual events in the guarded area. Although these information collection operations require a lot of time and work, they are an important part of the training process, because only these stages provide information about the correct operation of the system.

Correction according to the terrain – after the second evaluation of the result, the input data is corrected according to the specifics of the guarded area. If necessary, the intersection zones, illumination, dwell time in the area, and the type of monitored objects are corrected. This stage is more of a part of the AI's machine learning, but it also plays an important role in the overall picture.

Evaluation of the results after 144 hours – this is the place to expect an increase in Kef for the operation of the AI. In case there is no increase in this coefficient, a complete reconfiguration of the system is carried out and starts from scratch. The lack of a positive result at this stage indicates an incorrect design of the initial system and the need for a complete correction of the hardware part of the robotic security system and, if necessary, physical restructuring of the terrain.

Introduction of exceptions – in the case of repeated alarm events that the AI fails to report and correct, a new database with exceptions is introduced (Figure 4).

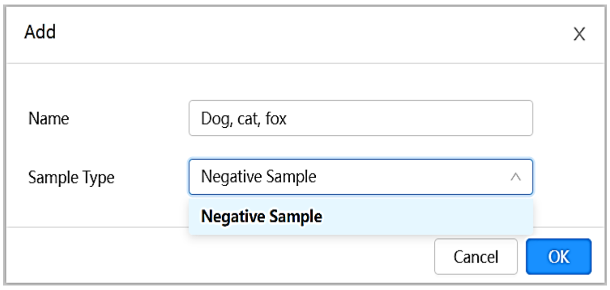

Name: Dog, cat, fox

Sample Type: Negative Sample

Negative Sample

Figure 4. Introducing exceptions for AI

This database contains moving and stationary objects, characteristic of the protected area itself, which the AI should not calculate in its work.

Evaluation of the results after 192 hours – at this stage, the maximum of the AI training has been reached. The goal is for Kef to be as close to unity as possible (2).

$$\lim_{g\to r}\frac{A_r}{A_g}=1 \qquad (2)$$

Handover to security – after a satisfactory assessment of the AI's performance, the system is ready for operation and the object is handed over to security. No trainer intervention is required anymore and the system works autonomously for security and decision-making.

3. RESULTS AND DISCUSSION

The processing of the results of the introduction of the different databases needs to be considered in accordance with the role and purpose of the specific database. The different aspects of the assessment are arranged in Table 2.

Results from implementing a COCO (Common Objects in Context) database for training AI in the video camera

During the initial training, the camera was repeatedly triggered by both humans and dogs (Figure 5a).

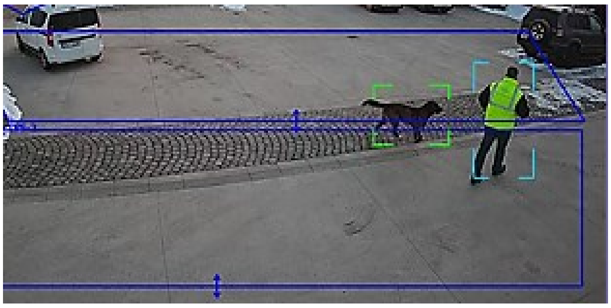

Figure 5a. Start of training

Already with the first correction of the input data, an increase in efficiency was observed, and at the end of the training, the system responded with activation only when people or cars crossed the perimeter (Figure 5b).

Figure 5b. End of training

The achieved efficiency after one week of AI training is 0.9167. Each subsequent correction is until the desired coefficient is reached with a value of one (Figure 6).

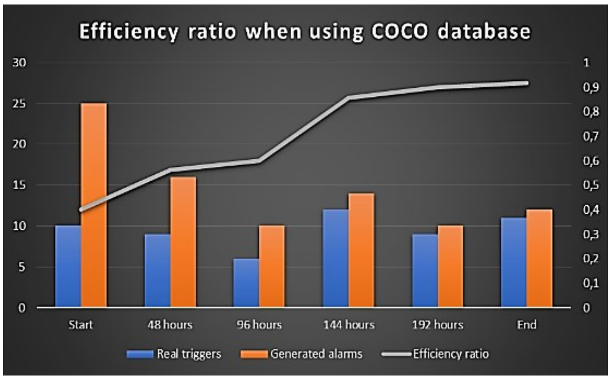

Figure 6. Efficiency coefficient when using the COCO database

Results from implementing the Open Images Dataset database for training AI in the video camera

The problem with introducing this database turned out to be the stationary square objects (Figure 7a).

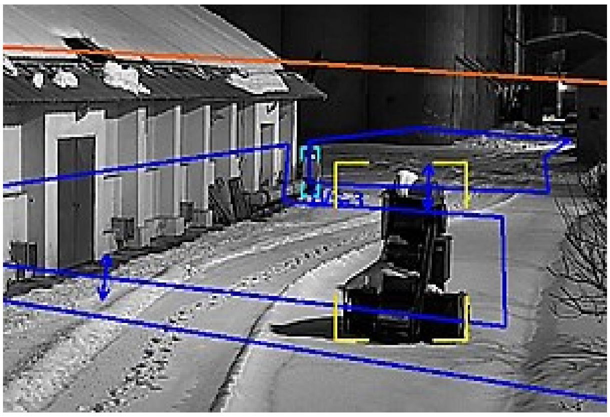

Figure 7a. Start of training

The AI's computational power coped with the problem after the stage of introducing the exceptions. After the last stage, the camera detects only people with a minimal risk of not detecting the movement of motor vehicles, since many of them are included in the exceptions (Figure 7b).

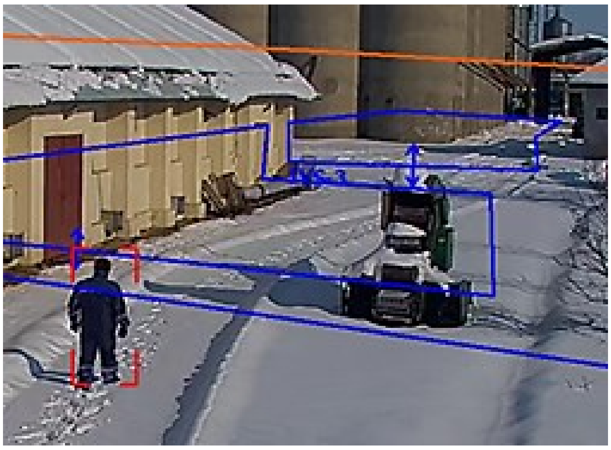

Figure 7b. End of training

TABLE 2.

Aspects of AI Training and Results

Aspect	Training data	Test data
Purpose of the selected database	Trains the AI to recognize intended objects	Confirms how well the AI has learned
Role of the selected database	Preparation for training	Test of already trained AI
Evaluation of the result	Not used to evaluate the effectiveness	Crucial to evaluate the effectiveness (speed, accuracy, correctness)
Optimization via database	Helps in training the AI	Provides optimization of the AI and informs if more training data is needed
Decision-making by the trainer	Used to build the final database	Used to decide on further training or adjustments based on the results

The achieved efficiency after one week of AI training is 0.8236. Any subsequent correction is to reach a coefficient of unity (Figure 8).

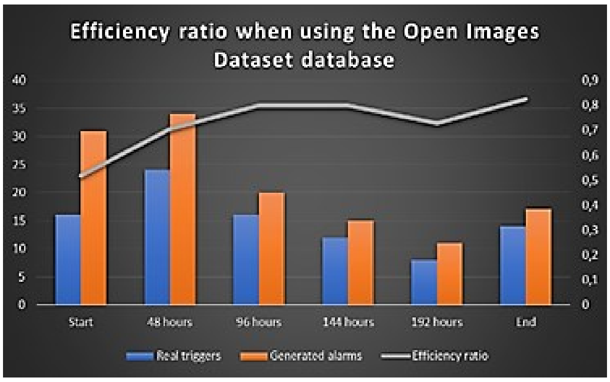

Figure 8. Efficiency ratio when using the Open Images |Dataset database

Results from implementing the UCF101 database for training AI in the video camera

The initial phase of the training process using the UCF101 dataset is illustrated in Figure 9a.

Figure 9a. Start of training

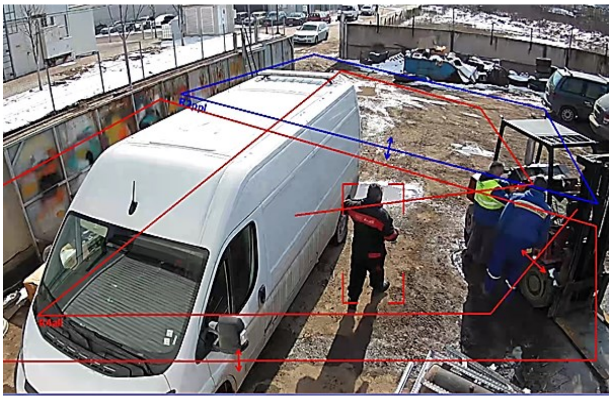

Figure 9b. End of training

The achieved efficiency after one week of AI training is 0.8181. Any subsequent correction is to reach a coefficient of unity (Figure 10).

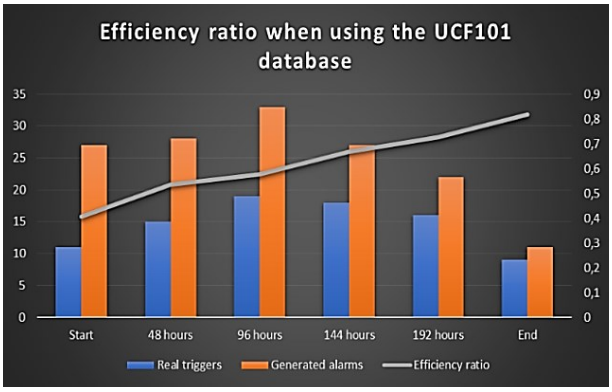

Figure 10. Efficiency ratio when using the UCF101 database

The diversity of data used improves the AI's ability to recognize patterns and make accurate predictions based on real-world scenarios. With minimal intervention from a trainer, a good value for the system's performance improvement index is achieved (3).

$$Ii = \frac{K_{ef}\ end}{K_{ef}\ start} \qquad (3)$$

The efficiency coefficients and improvement indices of the AI system according to the database are shown in Table 3.

TABLE 3.

Improvement Index for Trained AI

Database used	**Video camera 1**	**Video camera 2**	**Video camera 3**
	COCO	Open Images Dataset	UCF101
Kef start	0.4000	0.4161	0.4084
Kef end	0.9167	0.8235	0.8181
Improvement index Ii = Kef end/ Kef start	2.2918	1.9791	2.0032

The results of the study clearly demonstrate that video databases are essential for improving the accuracy and performance of AI algorithms in video camera systems. The selection of appropriate databases significantly affects the training and performance of AI in video camera technology. The quality of training data directly affects the performance and reliability of AI algorithms. Inaccuracies, biases, or missing data in training databases can lead to erroneous results and hinder the effectiveness of AI applications. Therefore, it is extremely important to prepare and maintain training databases with care and attention to detail.

4. CONCLUSION

In conclusion, effective AI training in video cameras relies heavily on the use of different types of databases tailored to meet specific needs. Structured databases provide a framework for effectively organizing and managing data, thereby increasing the accuracy of AI algorithms. Conversely, unstructured databases are essential for processing raw video footage, giving AI systems the ability to learn from diverse and complex visual information. Furthermore, the adoption of cloud-based databases facilitates scalability and accessibility, allowing for the storage and processing of vast amounts of data without the constraints of traditional infrastructures. Continuous learning and adaptation are essential for AI systems to remain relevant and effective in dynamic and complex environments. As AI technology continues to evolve, the integration of these diverse types of databases will play a crucial role in enhancing the capabilities of video cameras, ultimately leading to smarter and more responsive systems.

5. ACKNOWLEDGMENTS

In this section, we would like to thank all of our loved ones for their support and motivation throughout the process of our scientific research. This publication is funded by the fund "Support for Publishing Publications in Journals with Impact Factor (IF) and Impact Rank (SJR)" of Konstantin Preslavsky University of Shumen, Republic of Bulgaria.

References

[1] G. Aleksiev, *Theoretical foundations of the protection of the property of individuals or legal entities*, Alliance for Countering Terrorism-Arkhangel /APTA/, Kavarna, 2021.

[2] H. Varin, *Artificial intelligence in the field of security – advantages and disadvantages*, Collection of the International Scientific Conference „Artificial Intelligence in Security – Advantages and Threats“, vol. 2, 2022, pp. 66–69.

[3] M. Kozhuharov, “Artificial intelligence: basic concepts,” *Pedagogical forum*, 2023, pp. 3–24.

[4] A. Thomasian, "Structured, unstructured, and diverse databases," 2022, https://doi.org/10.1016/b978-0-32-390796-5.00018-8

[5] D. Dahiya, "Query-based information retrieval system adopting whale manhattan optimization-based deep belief neural network," *Multimedia Tools and Applications*, 2024, https://doi.org/10.1007/s11042-024-18783-y

[6] Y. Lee and J. Cho, "A Comparative Study on the Performance of Algorithms on Different AI Platforms," *International Journal on Advanced Science, Engineering and Information Technology*, 2024.

[7] A. Rajuroy et al., *Database Technologies in Real-Time AI Applications*, 2025.

[8] S. Nikolova, "Design, development and research of process efficiency in a robotic intelligent security system 'TEDI'," *KNOWLEDGE – International Journal Scientific Papers*, vol. 63.3, Institute of Knowledge Management, Skopje, 2024, pp. 289–295.

[9] S. Nikolova, "Exploring artificial intelligence machine learning in video surveillance," *Scientific Conference with international participation MATTEH 2024*, Conference proceeding, vol. 2, Shumen, 2024, pp. 17–22.

[10] S. Nikolova, "Application of convolutional neural networks for object recognition in AI video cameras," *Scientific Conference with international participation MATTEH 2024*, Conference proceeding, vol. 2, Shumen, 2024, pp. 136–142.

ANALYSIS OF THE IMPACT OF ARTIFICIAL INTELLIGENCE ON THE COURSE OF DEVELOPMENT IN ENGINEERING EDUCATION

Maria Pavlova

Technical University of Sofia
Bulgaria, 1000 Sofia, 8, Kl. Ohridski Blvd
E-mail: mariapavlova@tu-sofia.bg

Abstract

The rapid development of technology and changes in the ways of obtaining information after the years of the pandemic have, naturally, changed the issues surrounding the learning process. The pervasive integration of artificial intelligence within higher education institutions presents both challenges and opportunities for educators and students. The present article puts forth a cogent and inventive strategy for enhancing students' attention, interest, creativity, and satisfaction in fulfilling their educational obligations.

The study includes proposed approaches and their application in an educational environment, observations of the work of students and teachers, and statistical analysis of the data obtained.

As this is a matter of processes, and this study is in its nascent stages, the results should not be considered fully proven. Undoubtedly, the results delineate trends and processes that will prove instrumental in the development of the learning process in higher education institutions.

Key words: *Artificial Intelligence; Higher Education, GAI (Generative Artificial Intelligent) LA (Learning Analytics), metacognitive laziness*

1. INTRODUCTION

The human spirit is something that cannot be stopped. Throughout the centuries, humans have always sought development in every field. Proof of the scope of this development can be seen in the expansion of scientific fields. For example, in the second half of the 20th century, the number of scientific fields was around 10 (natural sciences, engineering, social sciences, etc.). A distinctive feature of these fields was their focus on the development of physics, mechanics, genetics, weapons, aviation, industry, etc. A distinctive feature is the fundamental nature of scientific research, technologies are analog and digital, the connection with business was indirect, and access to knowledge was limited, as was international cooperation. There is no pronounced interdisciplinarity, but there are clearly defined boundaries.

In the first half of the 21st century, things are different. There are more than 15 scientific fields, some of which are new (biotechnology, nanotechnology, space, etc.). The nature of research is more applied and interdisciplinary. Technologies are extremely digital and intelligent systems; access to knowledge is global and open, and the connection with business is direct through investment and innovation. The boundaries have been greatly expanded, as exemplified by biology and technical sciences.

This brief historical analysis is an excerpt from a larger and more comprehensive picture of the scope of scientific knowledge. It is also proof of the human spirit's relentless quest for knowledge. It is inherent in humans to understand and know, and this is related to both intellectual development and the degree of human satisfaction and happiness.

The following reflections in the article present the influence of artificial intelligence on the creative development of students, as well as their ability to engage in the learning process. Section 2 presents the guidelines and trends in the scientific literature on the topic. Section 3 provides a comparative analysis, and the conclusions are in Section 4.

2. ARTIFICIAL INTELLIGENCE IN HIGHER EDUCATION

The brief exposition presented in the introduction leads us to conclude that knowledge and skill acquisition are directly related to human nature and satisfy a basic human need.

2.1. Relationship between learning time and degree of knowledge and skills acquired

Despite the numerous articles (over 2000) written on the topic of the impact of artificial intelligence in higher education, there are still no in-depth and detailed analyses.

The advantages in the use of new technologies are significant, and there is insufficient exploitation time to discover and systematically describe the disadvantages.

In his study [1] Kestin presented the findings of research conducted with students from different universities. The research methodologies employed by the authors are founded on comparative analysis. Two groups of students were utilized in the study. In the initial study, a convenience sample of willing students who incorporated AI-tutoring into their education was selected. A second control group, receiving their education in the standard way, was also included in the study. The study described the following results: In the Intelligent Tutoring Systems (ITS) strand the students of the Group 1 need 10-20 minutes, while those of the Group 2 – 45 minutes (standart learning time for class). The results of the evaluation indicated that the first group demonstrated a double increase in knowledge retention and exhibited a higher level of engagement in the learning process. In accordance with the aforementioned methodology, the findings in the STEM disciplines, as well as those derived from YouTube, again indicated a preponderance in favor of Group 1.

Similar results are reported from Dr. Philippa Hardman [2]. The study from Harvard with students of the first group which can used AI tutor designed usithe pedagogisal principles and Goup 2 with standart learning approach. The results are similar. The students from Grpup 1 engaged with an AI-touring system for a duration of 49 minutes, while those of the second control group underwent a standard 60-minute lesson, give two times more learning gains tham Students from Group 2.

For the learning time is described also in [3], [4], [5], [6], [7] and more articles. A consensus has emerged among scholars that the effective time for processing educational material is at least half of the standard class period.

The observed outcomes can be rationalized by the following factors: students in the first group engage in independent work, while those in the second group are organized in class. It is also noteworthy that, AI tutorial provides immediate and precise responses, thereby facilitating the acquisition of knowledge at an accelerated pace.

The another reserch from Georg Kuh [8] with around 75000 students in four-year in coleagues or universityes (total 276). The project is National Survey of Student Engagement (NSSE), administered by Indiana University's Center for Survey Research. The focus of the research is does not directly address student success, but rather aims to examine how time spent at university with colleagues and professors influences learning outcomes.

However, a paucity of attention has been devoted to the question of the durability of knowledge and skills acquired by students through artificial intelligence.

Siqi Li at al. [9] in their article presented a "Machine learning-based recommendation system using an optimized collaborative filtering algorithm". This is a model which is compared in article with another and the described system achieve achieved 95% recall and 99% testing accuracy. In light of the results, the researchers implemented the model within a personalized learning system. Their findings suggest that the implementation of the model enhances educational quality and student outcomes.

In the context of academic pursuits, the reduction of learning time can be advantageous when the primary objective is the accumulation of knowledge. Nevertheless, the fundamental objective of the educational process has invariably been to ensure that knowledge is translated into applicable and beneficial skills. In this regard, the efficacy of ITS [3] or STEAM [10] is limited, as the development of skills is influenced by a multitude of factors that extend beyond the scope of knowledge. As discussed in the aforementioned articles, all models similar to those under consideration are, in essence, the development of a tool. During the Renaissance, the advent of printing technology was as transformative as the advent of [3], [4], [6] and etc., is in the contemporary era, characterized by rapid advancements in technology. The medium through which students express themselves, whether in a notebook with a pen or on a digital platform, is of secondary importance when considering the competencies that they develop. The acquisition of skills establishes a foundation for abilities, which in turn fosters the development of specific competencies that benefit the individual, as well as their peers.

This phenomenon, as noted by psychologists and the Creator of the universe [11], fulfills a fundamental human need, thereby contributing to subjective well-being and the attainment of material prosperity. The authors also mentioned about the problem with communication skills of the students, because as I have already shown the ITS is strong in individual learning.

2.2. Relationship between learning community participation and student engagement

The historical context of the evolution from face-to-face teaching and learning processes to distance learning, which was aided by the time of the Coronavirus, has strengthened the model of knowledge adoption through ITS. This model also brings with it problems such as social isolation, lack of critical thinking, metacognitive laziness, etc. similar. The capacity to negotiate and collaborate effectively is of paramount importance, underscoring the significant investment in research in this domain. Pike at al. [12] use 2000 Carnegie classification and appley it in academic education. Similar approach is described by Gellin [13] and Zhang [14] also Bano at al. [15] which have written about the problem in this area. The conclusion is that social life like coffee, pizza, collaborate with educators have directional connection with their learning results and especially student engagement in university live.

3. GENERATIVE AI IN HIGHER EDUCATION

Khosravi at al. [16] represent the impact of the GenAI in Learning Analytics. In their article they present deeply analysis of the impact of GenAI in quality and quantity of the papers in different countries. The methods are used in the article is Clow's LA cycle as an organizing framework (Clow, 2012).

Chiu at al. also have written about GenAI in education [17] as well Pierres at al. [18]. Pierres and colleague made deeply research and discus Pires and his colleagues conduct in-depth research in 30 pages and discuss topics such as:

- Access and information retrieval
- Learning methodologies
- Student engagement
- Faculty adaption

They also write about the problems like risk of plagiarism, low accuracy, the lack of privacy, loss of human values, possible overreliance on technology, job replacement and etc. Their used method is semi-structured interview. Also they made comparison analysis over 35 authors.

3.1. Virtual Reality (VR) in higher education

Another tool used in education is VR. Its implementation in education is a subject of research within the scientific community. VR is not only used for bottle learning, but also in school environments. Developing such software is expensive, so its effectiveness must be proven to justify the investment. Astatke described immersive virtual reality (IVR) [19] applied in STEAM education. Chang at al. [20] and Checa [21] also deeply search the positive effects of IVR in education. They focus their research on the relationship between virtual reality (VR) and the development of creativity and critical thinking in students. Cela at al. made research with Albanian students [22], Reiss [23] made the similar review of the existing articles and He gives the benefits and also the ethical problems with Brazilian students, Baker at al. [24] make comparative analyses between Learning Community (LC) participant and non-LC students. The last mentions authors make the similar conclusion that the IVR give very good results and it raises serious questions about ethical norms, mental laziness, the ability to think critically.

3.2. Methods

The used method in this article is Cross-case comparative analysis and historical analysis. Data for the analysis were collected from studies published in leading global databases such as Springer, GSI, International Journal of Education, WEB of science and etc.

The key points in the reviewed studies are presented objectively. The key points are related to the topic of this review article.

4. CONCLUSION

The objective of this article is to examine the impact of Artificial Intelligence (AI) in higher education on the evolution of engineering education and the personal growth of students. To this end, a comprehensive database has been thoroughly reviewed, and the extant publications of various scientists in this field have been presented. A portion of the data collection is cited in the bibliography.

The development of AI models has been shown to reduction of the learning time required for knowledge acquisition. Furthermore, these measures have been demonstrated to enhance student engagement and interest.

The speed of knowledge acquisition does not lead to speed in the acquisition of skills.

The speed of acquisition and assimilation of knowledge is further facilitated by the individualized approach that is widely used and well developed in the context of ITS and GenAI.

The integration of GenAI has been demonstrated to enhance student engagement and academic performance. As a GenAI system, it is imperative that it be developed to be perceived by as many senses as possible.

The basic and conceptual knowledge is around 30-50% from all comprehensive process of learning and shaping the personality. Comprehension and application are also important part and this part is not possible to be evaluated by AI.

That is the reason that all of the mention scientistic give conclusion that the AI is instrument which support the teachers, but in no case should it replace them.

The course of development in engineering education will evolve towards increasing the implementation of modern technologies in various ways.

The involvement of students in the social life of the university, as well as in joint activities with teachers, increases their commitment to the learning process. This proves that AI can be an aid to teaching and preparation, but not a substitute for the teacher.

One of the main goals of education is to achieve self-control [25] in basic human principles and values on the part of students. Only with students who have mastered self-control would the use of AI be useful and metacognitive laziness be prevented.

ACKNOWLEDGEMENT

The author would like to thank the Research and Development Sector at the Technical University of Sofia for the financial support.

References

[1] G. Kestin, K. Miller, A. Klales, T. Milbourne, and G. Ponti, "AI tutoring outperforms in-class active learning: an RCT introducing a novel research-based design in an authentic educational setting", doi: 10.1038/s41598-025-97652-6.

[2] "AI Tutors Double Rates of Learning in Less Learning Time." Accessed: Aug. 04, 2025. [Online]. Available: https://drphilippahardman.substack.com/p/ai-tutors-double-rates-of-learning

[3] Létourneau, M. Deslandes Martineau, P. Charland, J. A. Karran, J. Boasen, and P. M. Léger, "A systematic review of AI-driven intelligent tutoring systems (ITS) in K-12 education," NPJ Sci Learn, vol. 10, no. 1, p. 29, Dec. 2025, doi: 10.1038/S41539-025-00320-7.

[4] "Global Education Monitoring Report 2023: Technology in education: A tool on whose terms?," Global Education Monitoring Report 2023: Technology in education: A tool on whose terms?, Jul. 2023, doi: 10.54676/UZQV8501.

[5] "22 Thoughts on Using AI to Learn Better - Scott H Young." Accessed: Jul. 30, 2025. [Online]. Available: https://www.scotthyoung.com/blog/2025/05/13/22-thoughts-on-using-ai-to-learn-better/

[6] K. vanLehn, "The relative effectiveness of human tutoring, intelligent tutoring systems, and other tutoring systems," Educ Psychol, vol. 46, no. 4, pp. 197–221, 2011, doi: 10.1080/00461520.2011.611369.

[7] "Rethinking Learning Tools: Beyond the AI vs Traditional Debate | LinkedIn." Accessed: Jul. 30, 2025. [Online]. Available: https://www.linkedin.com/pulse/rethinking-learning-tools-beyond-ai-vs-traditional-debate-john-dolman-d5kuc/

[8] G. D. Kuh, " Assessing What Really Matters to Student Learning Inside The National Survey of Student Engagement ," Change: The Magazine of Higher Learning, vol. 33, no. 3, pp. 10–17, May 2001, doi: 10.1080/00091380109601795;

[9] S. I. Q. I. LI and D. LI, "Research on personalized learning recommendation system based on machine learning algorithm," Scalable Computing, vol. 26, no. 1, pp. 432–440, 2025, doi: 10.12694/SCPE.V26I1.3844.

[10] R. W. A.-H. Bedar and M. A. Al-Shboul, "The Effect of Using STEAM Approach on Motivation Towards Learning Among High School Students in Jordan," International Education Studies, vol. 13, no. 9, p. 48, Aug. 2020, doi: 10.5539/IES.V13N9P48;

[11] "OFFICIAL KING JAMES BIBLE ONLINE: AUTHORIZED KING JAMES VERSION (KJV)." Accessed: Aug. 05, 2025. [Online]. Available: https://www.kingjamesbibleonline.org/

[12] G. R. Pike, G. D. Kuh, and A. C. McCormick, "An Investigation of the Contingent Relationships Between Learning Community Participation and Student Engagement," Res High Educ, vol. 52, no. 3, pp. 300–322, May 2011, doi: 10.1007/S11162-010-9192-1/METRICS.

[13] Gellin, "The effect of undergraduate student involvement on critical thinking: A meta-analysis of the literature, 1991–2000," J Coll Stud Dev, vol. 44, no. 6, pp. 746–762, 2003, doi: 10.1353/csd.2003.0066.

[14] S. Zhang, "Artificial Intelligence in Higher Education: Opportunities, Challenges, and Future Prospects," Creativity and Innovation, vol. 8, no. 6, pp. 55–62, Dec. 2024, doi: 10.47297/WSPCIWSP2516-252710.20240806.

F. Bano, S. H. Serbaya, A. Rizwan, M. Shabaz, F. Hasan, and H. S. Khalifa, “An artificial neural network and Levenberg-Marquardt training algorithm-based mathematical model for performance prediction,” Applied Mathematics in Science and Engineering, Dec. 2024, doi: 10.1080/27690911.2024.2375529; WEBSITE: TFOPB;PAGEGROUP:STRING:PUBLICATION.

[15] H. Khosravi, O. Viberg, V. Kovanovic, and R. Ferguson, “Generative AI and Learning Analytics,” Journal of Learning Analytics, vol. 10, no. 3, pp. 1–6, Dec. 2023, doi: 10.18608/jla.2023.8333.

[16] T. K. F. Chiu, “The impact of Generative AI (GenAI) on practices, policies and research direction in education: a case of ChatGPT and Midjourney,” Interactive Learning Environments, vol. 32, no. 10, pp. 6187–6203, 2024, doi: 10.1080/10494820.2023.2253861.

[17] O. Pierrès, A. Darvishy, and M. Christen, “Exploring the role of generative AI in higher education: Semi-structured interviews with students with disabilities,” Educ Inf Technol (Dordr), vol. 30, no. 7, pp. 8923–8952, May 2025, doi: 10.1007/S10639-024-13134-8.

[18] M. Astatke, C. Weng, and A. Yohannes, “What is the role of immersive virtual reality (IVR) in the development of creativity skills and engagement among students in STREAM (Science, Technology, Religion, Engineering, Art, and Mathematics)-based learning?,” Educ Inf Technol (Dordr), pp. 1–23, May 2025, doi: 10.1007/S10639-025-13610-9/TABLES/4.

[19] Y. S. Chang, C. H. Chou, M. J. Chuang, W. H. Li, and I. F. Tsai, “Effects of virtual reality on creative design performance and creative experiential learning,” Interactive Learning Environments, vol. 31, no. 2, pp. 1142–1157, 2023, doi: 10.1080/10494820.2020.1821717.

[20] D. Checa and A. Bustillo, “A review of immersive virtual reality serious games to enhance learning and training,” Multimed Tools Appl, vol. 79, no. 9, pp. 5501–5527, Mar. 2020, doi: 10.1007/s11042-019-08348-9.

[21] E. Çela, M. M. Fonkam, and R. M. Potluri, “Risks of AI-Assisted Learning on Student Critical Thinking: A Case Study of Albania,” https://services.igiglobal.com/resolvedoi/resolve.aspx?doi=10.4018/IJRCM.350185, vol. 12, no. 1, pp. 1–19, Jan. 1AD, doi: 10.4018/IJRCM.350185.

[22] M. J. Reiss, “The use of AI in education: Practicalities and ethical considerations,” London Review of Education, vol. 19, no. 1, pp. 1–14, 2021, doi: 10.14324/LRE.19.1.05.

[23] S. Baker and N. Pomerantz, “Impact of Learning Communities on Retention at a Metropolitan University,” J Coll Stud Ret, vol. 2, no. 2, pp. 115–126, Aug. 2000, doi: 10.2190/62P5-CQ2U-NTUW-DM1C;

[24] “Fundamentals of Christian Education — Ellen G. White Writings.” https://m.egwwritings.org/en/book/32.279?hl=.4&ss=eyJ0b3RhbCI6NzcsInBhcmFtcyI6eyJxdWVyeSI6Ii40IiwidHlwZSI6ImJhc2ljIiwibGFuZyI6ImVuIiwibGltaXQiOjIwLCJwdWJucyI6MzJ9LCJpbmRleCI6OH0%3D#283

A LABORATORY SESSION ON SPECTRUM SENSING

Ludwig Lubich

Technical University of Sofia, Faculty of Telecommunications
1000 Sofia, 8 Kl. Ohridski Blvd
lvl@tu-sofia.bg

Abstract

The paper presents the experience in developing a laboratory session on spectrum sensing. It is suitable for undergraduate students in wireless communications and can also be useful for the students in related areas. The laboratory session includes both computer simulations and experiments with real-world signals. For the purposes of the exercise, a Matlab program with a graphical user interface and a GNU Radio Companion flow graph have been developed. These have been briefly described in the paper. A sample plan for the laboratory session is also given.

1. INTRODUCTION

Spectrum sensing is the process of monitoring the radiofrequency spectrum in order to discover unoccupied bands. It is a key component of cognitive radio systems which allows them to use the spectrum in an opportunistic manner.

Although it has been long since spectrum sensing became a topic of considerable importance, publications presenting the approach to teaching it through laboratory sessions are rare. Despite the author's best efforts, only one detailed description of a laboratory exercise was found [1]. It undoubtedly pocess a flawless scientific accuracy, but from a pedagogical point of view it has weaknesses such as unclearly articulated objectives and a somewhat unsystematic structure. Based on all this, it could be assumed that sharing experience in developing of a laboratory session on spectrum sensing could be useful for the academic community.

The paper will not deal with the theoretical preparation of the students for the lab, as this is the subject of the lectures, and there are also enough tutorials, as for example [2] and [3], as well as plenty of other publications. Only the author's approach to some basic issues that, according to his observations, are stumbling blocks for students will be shared.

The rest of the paper is organized as follows: Section 2 provides the objectives of the exercise and the main considerations taken into account in its development; Section 3 presents the Matlab program and the GNU Radio Companion (GRC) flow graph developed for the needs of the laboratory session; Section 4 provides a sample plan and guidelines for conducting it; Section 5 presents the conclusions.

2. CONCEPTION OF THE LABORATORY SESSION

The main goal of the laboratory session is for the students to gain a better understanding of spectral sensing from a more practical perspective through experimentation. Specifically, the following objectives are intended to be achieved:

1. Developing a good understanding of the possible outcomes of hypothesis testing in signal detection, the corresponding probabilities and their interrelations, the influence of the detector threshold choice on the detection probability and false alarm probability, the meaning of the ROC curve and the process of construc-ting it.
2. Learning about the influence on the detector performance of the signal to noise ratio (SNR), the number of processed samples, the noise PSD uncertainty, and the choice of additional detector options.
3. Achieving a better understanding of the advantages and disadvantages of different signal detection algorithms.

In order to achieve these purposes, clean experiments with good repeatability are appropriate. In view of this, simulations were preferred over detection of signals received from the air.

Further, experiments with signals received by a software defined radio (SDR) are provided to acquaint students with the peculiarities of the real-world radio frequency spectrum.

Four types of detectors are examined in the laboratory session: energy [4], matched filter [5], eigenvalue-based [6], and cyclostationary feature detector [7].

Some aspects of the spectrum sensing have been omitted because they are appropriate for more advanced courses or because of the limited amount of knowledge that can be absorbed in a single session.

3. TOOLS

A Matlab program with a graphical user interface (GUI) has been developed to perform the simulations of detectors. To receive real-world signals, an inexpensive software-defined radio can be used, which in our case is RTL-SDR [8]. A GRC flow graph has been developed for real-time processing of the received samples.

3.1. The program for detector simulations

The program can simulate repeatedly any of the four types of detectors mentioned above. We chose to detect a DVB-T2 signal (simplified), because it has a wide variety of features. The main window of the program is shown in Fig. 1. The GUI allows setting of:

- The type of detector that will be examined and some of its options.
- The detector threshold.

Detector type: Matched filter

Pattern: P2 pilots

Threshold: 7

SNR, dB: -30

Noise PSD, dBm/Hz: -168

Number of samples: 17408

Number of trials: 1000

The number of samples is corrected to 17408

No signal		Signal present	
N n	1000	N s+n	1000
T avg	-0.060067	Tavg	12.5447
N tn	972	N det	927
N fa	28	N miss	73
P tn	0.972	P det	0.927
P fa	0.028	P miss	0.073

Figure 1. GUI screenshot of the detector simulation program

- The number of trials, i.e. the number of noise realizations and noise plus signal realizations for which the detector is simulated.
- The number of samples that will be processed by the detector in each trial. For some types of detectors or their options, the number of samples cannot be arbitrary. In these cases, when an inappropriate number of samples is entered, the program automatically corrects it and gives a message.
- The signal-to-noise ratio (SNR).
- The power spectral density (PSD) of the noise. This makes possible to examine the influence of the noise PSD uncertainty on the detector performance.

The simulation is launched by the **Start** button. If too many samples or trials are chosen and the simulation is running too long, it can be stopped by the **Terminate** button.

After the simulation is completed, all set values and selected options remain locked, which makes it impossible to see values, options and results that do not correspond to each other. To proceed with a new simulation, first the **New** button should to be pressed to unlock them, which clears the results of the last simulation. The following results are displayed:

1) The average values of the test statistic for the cases where there is only noise and for the cases where a signal is present. This can be used to obtain an initial rough orientation about the range of the appropriate threshold values. Calculating them requires the use of cumbersome expressions, which would hardly contribute to a better understanding of the subject being studied.

2) The counts of detections, false alarms, missed detections, and true negatives, as well as their relative frequencies, which are estimates of the corresponding probabilities. Undoubtedly, there is a redundancy in these results, but displaying all of them is appropriate from an educational point of view.

In addition to the simulation results, PSD estimates of the noise and signal separately and a PSD estimate of the mixture of signal and noise for the last trial are displayed. When examining a cyclostationary feature detector, an auxiliary window opens, showing the time-varying autocorrelation function and its spectrum for the last trial.

The ROC curves and other possible dependencies are obtained point by point. To construct a ROC curve, students must make several simulations, choosing different thresholds for each of them. Clearly, the procedure could be highly automated so that the ROC curve is obtained at once. However, the author's view is that students should touch at least a little under the hood of the objects being studied. The point-by-point investigating and recording of the relationships makes the student think about what is actually happening in the detector under study and what needs to be done at any particular moment. This ultimately leads to a better understanding of the subject. Conversely, automatically obtained results hardly contribute to achieving the goals of the lesson even among the most conscientious students. The following should always be kept in mind: The belief that the core of a laboratory session is to mechanically obtain and correctly record numerical results without thinking about them, is surprisingly common among some students. That is why, all measures should be taken in to stimulate their mental activity.

3.2. The GRC flow graph for real-world signal detection

The flow graph developed (Fig. 2) implements a cyclostationary feature detector similar to the one proposed in [7]. In our case, it is oriented towards detecting DVB-T signals. The fact that the bandwidth that can be processed is narrower than the bandwidth of a television channel is not an obstacle to its operation. A screenshot of the created QT GUI is given in Fig. 3. Using sliders, the frequency of the TV channel whose occupancy is checked is set, and a fine tuning can also be made if desired. The duration of the guard interval duration can be set using a menu. The remaining parameters are fixed according to the DVB-T signals received in the area of the Technical University of Sofia. The value of the test statistic is shown in a logarithmic scale by a bar graph display. The PSD of the input signal, the time-varying autocorrelation function and its spectrum are also displayed.

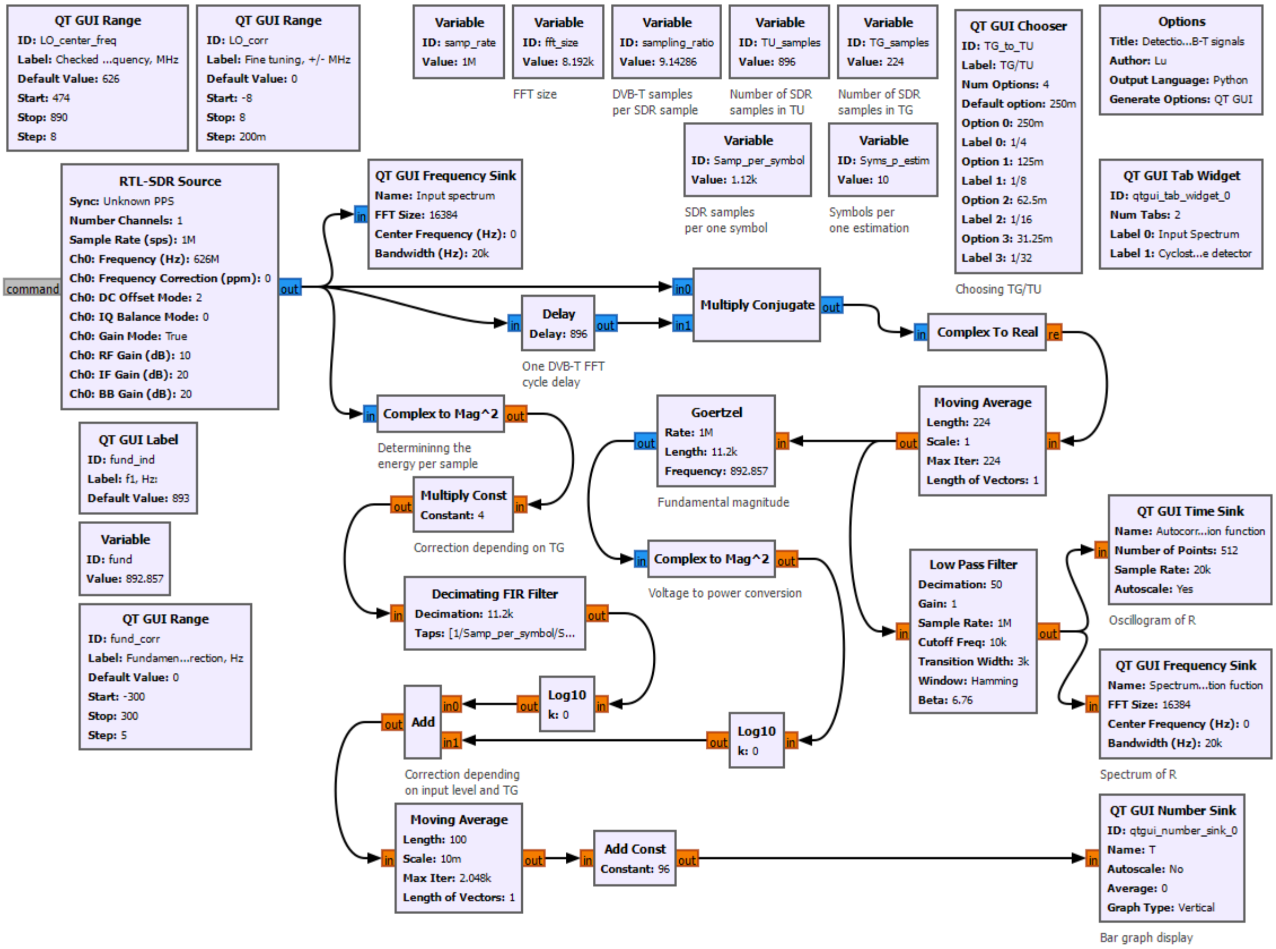

QT GUI Range
ID: LO_center_freq
Label: Checked ...quency, MHz
Default Value: 626
Start: 474
Stop: 890
Step: 8

QT GUI Range
ID: LO_corr
Label: Fine tuning, +/- MHz
Default Value: 0
Start: -8
Stop: 8
Step: 200m

Variable
ID: samp_rate
Value: 1M

Variable
ID: fft_size
Value: 8.192k

Variable
ID: sampling_ratio
Value: 9.14286

Variable
ID: TU_samples
Value: 896

Variable
ID: TG_samples
Value: 224

QT GUI Chooser
ID: TG_to_TU
Label: TG/TU
Num Options: 4
Default option: 250m
Option 0: 250m
Label 0: 1/4
Option 1: 125m
Label 1: 1/8
Option 2: 62.5m
Label 2: 1/16
Option 3: 31.25m
Label 3: 1/32

Options
Title: Detectio...B-T signals
Author: Lu
Output Language: Python
Generate Options: QT GUI

Variable
ID: Samp_per_symbol
Value: 1.12k

Variable
ID: Syms_p_estim
Value: 10

QT GUI Tab Widget
ID: qtgui_tab_widget_0
Num Tabs: 2
Label 0: Input Spectrum
Label 1: Cyclost...e detector

RTL-SDR Source
Sync: Unknown PPS
Number Channels: 1
Sample Rate (sps): 1M
Ch0: Frequency (Hz): 626M
Ch0: Frequency Correction (ppm): 0
Ch0: DC Offset Mode: 2
Ch0: IQ Balance Mode: 0
Ch0: Gain Mode: True
Ch0: RF Gain (dB): 10
Ch0: IF Gain (dB): 20
Ch0: BB Gain (dB): 20

QT GUI Frequency Sink
Name: Input spectrum
FFT Size: 16384
Center Frequency (Hz): 0
Bandwidth (Hz): 20k

Delay
Delay: 896

Multiply Conjugate

Complex To Real

QT GUI Label
ID: fund_ind
Label: f1, Hz:
Default Value: 893

Complex to Mag^2

Goertzel
Rate: 1M
Length: 11.2k
Frequency: 892.857

Moving Average
Length: 224
Scale: 1
Max Iter: 224
Length of Vectors: 1

Multiply Const
Constant: 4

Variable
ID: fund
Value: 892.857

Complex to Mag^2

QT GUI Time Sink
Name: Autocorr...ion function
Number of Points: 512
Sample Rate: 20k
Autoscale: Yes

Low Pass Filter
Decimation: 50
Gain: 1
Sample Rate: 1M
Cutoff Freq: 10k
Transition Width: 3k
Window: Hamming
Beta: 6.76

QT GUI Range
ID: fund_corr
Label: Fundamen...rection, Hz
Default Value: 0
Start: -300
Stop: 300
Step: 5

Decimating FIR Filter
Decimation: 11.2k
Taps: [1/Samp_per_symbol/S...

Add

Log10
k: 0

Log10
k: 0

QT GUI Frequency Sink
Name: Spectrum...tion fuction
FFT Size: 16384
Center Frequency (Hz): 0
Bandwidth (Hz): 20k

Moving Average
Length: 100
Scale: 10m
Max Iter: 2.048k
Length of Vectors: 1

Add Const
Constant: 96

QT GUI Number Sink
ID: qtgui_number_sink_0
Name: T
Autoscale: No
Average: 0
Graph Type: Vertical

Figure 2. The GRC flow graph for cyclostationary feature detector exploration

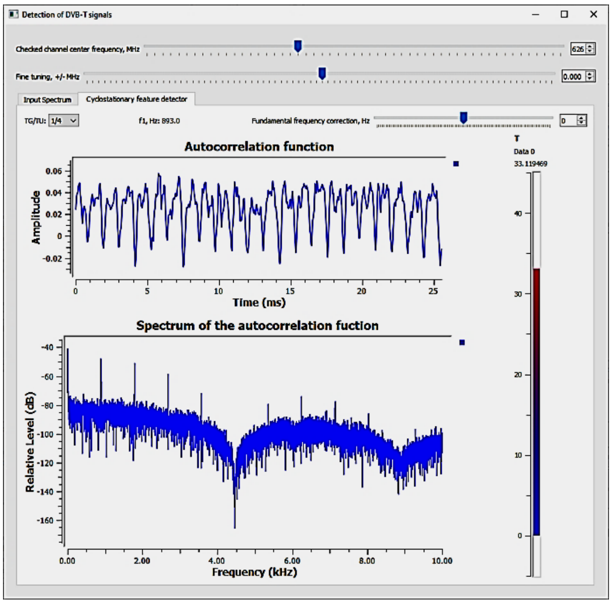

Detection of DVB-T signals

Checked channel center frequency, MHz 626

Fine tuning, +/- MHz 0.000

TG/TU: 1/4

f1, Hz: 893.0

Fundamental frequency correction, Hz 0

Data 0 33.119469

Figure 3. QT GUI for cyclostationary feature detector exploration

4. A SAMPLE PLAN AND GUIDELINES FOR CONDUCTING THE LABORATORY SESSION

Naturally, the laboratory exercise should begin with a brief discussion of the theory with the students.

The experience in conducting this exercise shows that students have difficulties in understanding the ROC curve, more specifically its meaning and the way it is constructed. Related to this is the lack of understanding how the basic probabilities of interest are affected by the choice of the detector threshold. To address these problems, it is good to offer students some tasks and questions alongside direct explanations.

It can be started with the following joke problem: Imagine someone orders a detector to be developed with a 100% detection probability, forgetting to set any requirements regarding the false alarm probability. How would an unscrupulous person proceed to formally satisfy the customer's requirements in the easiest way? Solving this problem, students will clearly understand that the detection and false alarm probabilities must be considered jointly.

Next, it is appropriate to show the students some typical probability density functions of the test statistic in the absence and in the presence of a signal and ask them to figure out how the detection and false alarm probabilities will depend on the choice of the threshold. It is best to consider an energy detector, because that it is the most intuitive. After this investigation, students should clearly realize that there is a trade-off between the detection and the false alarm probability. At this point, they should be ready to understand the meaning and the importance of the ROC curve and how it is constructed.

Further on, it is appropriate to ask students to speculate on following questions:

How will the two probability density functions change when the SNR varies, and what will they look like at extremely large and extremely small SNR values in particular? Accordingly, how will the dependences of the detection and false alarm probabilities on the threshold as well as the ROC curve change?

Then students are asked to figure out what the ideal and the worst possible ROC curve should look like. After that, they will be able to compare different detectors based on their ROC curves.

Students can also be asked to make predictions how the detector performance would change if the number of samples processed is increased.

After completing this preparation, the experimental part of the session can be started. A sample plan is given below, which can be modified according to the students' abilities and interests.

1) Simulations are performed to confirm the speculations made during the theoretical preparation. This includes the following tasks:

- The dependences of the detection and false alarm probabilities on the threshold for a given detector type, number of samples and two SNR values are recorded and graphically presented.
- The corresponding ROC curves are drawn.
- The influence of the number of processed samples on the detector performance is examined. For this purpose, the ROC curves for two given numbers of samples at fixed SNR and threshold values are constructed.

2) Various types of detectors are examined in detail. For each detector the following is done:

- The ROC curves for three SNR values are constructed. Two of the SNR values are chosen in such a way as for one of the ROC curves to be nearly perfect and one to be near the random guessing line. This choice is made in order to allow the comparison between the different detectors.

- The influence of the noise PSD uncertainty is investigated. For this purpose, the threshold should be chosen to obtain some good combination of detection and false alarm probabilities; then the noise PSD is varied at fixed SNR and the values of the two probabilities are observed. While doing this, it should be taken into account that the noise PSD uncertainty is normally 1 to 2 dB in practice [6].

For detectors with additional options, studies are performed when selecting different options.

3) The results of the different simulations are compared and short conclusions are written. This, although often underestimated, is actually vital for the fruitful performance of laboratory exercises in general. Otherwise, the risk of them turning into a mechanical execution of prescribed actions is very high even for diligent students.

4) A detector is examined using real-world signals received through an SDR. In particular, in described laboratory session, the occupancy of television channels in a given frequency interval is checked. This can be enriched with some additional tasks that depend on the specific needs of the students being taught, so they will not be discussed here.

The exercise involves a relatively large amount of graphic work. It is significantly facilitated by providing students with forms containing titled boxes for the graphs with graduated and labeled axes. Tabulation of the results in the lab report is not required, and the values obtained are directly marked as points in the corresponding coordinate planes. Alternatively, any program capable of drawing graphs can be used, which often takes more time than the first option. As long as the student is aware of what he is doing, constructing the graphs manually is quick and easy and poses almost no burden.

CONCLUSION

A laboratory session on spectrum sensing was presented. The experience of conducting it shows that the set objectives have been achieved. It was also found that the topic is relatively difficult for many students. Therefore, it is possible, depending on the participants' level of preparation, to reduce the set of tasks so that they can better understand the basic concepts. It is also advisable to ensure a closer interaction between the teacher and the students during this exercise.

References

[1] "ECE4305: Software-Defined Radio Systems and Analysis, Laboratory 4: Spectrum Sensing Techniques" http://courses.washington.edu/ee506/projects/lab4.pdf. Acessed 09 July 2025.

[2] D. A. Guimaraes, "Spectrum Sensing: A Tutorial", Journal of Communication and Information Systems, Vol. 37, No.1, 2022.

[3] Tellambura, C., "Spectrum Sensing Methods and Their Performance". In: Zhang, W. (eds) Handbook of Cognitive Radio . Springer, Singapore, 2019.

[4] P. Pandya, A. Durvesh and N. Parekh, "Energy Detection Based Spectrum Sensing for Cognitive Radio Network", 2015 Fifth International Conference on Communication Systems and Network Technologies, Gwalior, India, 2015, pp. 201-206.

[5] S. Kapoor, S. Rao and G. Singh, "Opportunistic Spectrum Sensing by Employing Matched Filter in Cognitive Radio Network", 2011 International Conference on Communication Systems and Network Technologies, Katra, India, 2011, pp. 580-583.

[6] Y. Zeng and Y.-C. Liang, "Eigenvalue-based spectrum sensing algorithms for cognitive radio", IEEE Transactions on Communications, vol. 57, no. 6, pp. 1784-1793, June 2009.

[7] A. Tani, R. Fantacci and D. Marabissi, "A Low-Complexity Cyclostationary Spectrum Sensing for Interference Avoidance in Femtocell LTE-A-Based Networks", IEEE Transactions on Vehicular Technology, vol. 65, no. 4, pp. 2747-2753, April 2016.

[8] "About RTL-SDR", https://www.rtl-sdr.com/about-rtl-sdr/. Acessed 09 July 2025.

AN AI-POWERED FRAMEWORK FOR REAL-TIME WILDFIRE DETECTION USING THERMAL IMAGING (THERMOVISION)

Svetlin Antonov

Technical University of Sofia, Faculty of Telecommunications
1000 Sofia, Bulgaria, 8 Kl. Ohridski Blvd
https://orcid.org/0000-0002-1698-8506;
svantonov@tu-sofia.bg

Abstract

The rapid and reliable detection of early-stage wildfires remains a significant challenge, as traditional methods often suffer from delays and high false alarm rates. This paper presents an AI-powered framework to address this problem. The core of our contribution is a custom-developed Convolutional Neural Network (CNN) trained on a large, curated dataset of thermal (thermovision) images acquired from both ground-based and aerial (UAV) platforms. The principal results are highly promising: the model achieved a detection accuracy of 99.2% in identifying the thermal signatures of incipient fires. Furthermore, it demonstrated exceptional robustness against common false positives such as sun glint and hot rocks, representing a significant improvement over conventional threshold-based detection algorithms.

1. INTRODUCTION

The growing frequency and intensity of wildfires present a significant and escalating global challenge. Driven by climate change and shifting land-use patterns, these events inflict devastating ecological damage, pose severe risks to human life and property, and result in substantial economic losses [1]. A critical factor in mitigating the impact of a wildfire is the speed and accuracy of its initial detection. The earlier an incipient fire can be identified, the more effectively and safely it can be contained and suppressed.

Traditional wildfire detection methods, which include human observers in watchtowers, public reporting, and satellite-based monitoring, have inherent limitations. Human-centric approaches are constrained by geography and are not scalable, while satellite systems often suffer from significant temporal delays between passes, allowing a fire to grow substantially before it is detected. While automated sensors offer a potential solution, simple thermal sensors that trigger an alarm based on a fixed temperature threshold are notoriously prone to high false alarm rates, being activated by non-fire sources such as sun-heated rocks, metallic surfaces, or other benign thermal anomalies [2].

This research addresses the need for a more intelligent and reliable detection system by combining the strengths of thermal imaging (thermovision) with the pattern-recognition capabilities of artificial intelligence. Thermal cameras can detect the heat signature of a fire day or night and through smoke, providing a rich data source [3]. However, interpreting this data requires a sophisticated approach. Deep learning, specifically through the use of Convolutional Neural Networks (CNNs), is exceptionally well-suited for this task, as it can learn to distinguish the complex spatial and temporal patterns of a real fire from the myriad of potential false positives [4].

The objective of this paper is to develop and validate a CNN-based framework for the accurate and rapid detection of early-stage wildfires from thermovision data. We present the design of a custom CNN model, its training on a diverse dataset of thermal images from ground and aerial platforms, and a comprehensive evaluation of its performance, demonstrating its high accuracy and robustness against common false alarms.

2. METHODOLOGY

2.1. Dataset and Image Acquisition

The foundation of this study is a large and diverse dataset of thermal images, comprising a total of 15,000 images. The data was collected using two primary platforms to ensure variability. A ground-based system, consisting of a FLIR E 40 thermal camera mounted on a panoramic tripod, was used to capture static scenes. For aerial data, a DJI Matrice 300 RTK unmanned aerial vehicle (UAV) equipped with a Zenmuse H20T thermal camera was flown over various terrains, a common practice in modern environmental surveillance [5].

The dataset was carefully curated to create a balanced representation of two classes: 'Fire' and 'No Fire'. The 'Fire' class (7,500 images) includes images of controlled burns of various sizes, from small incipient fires to more developed flames. The 'No Fire' class (7,500 images) was specifically designed to include common false positive scenarios, such as sun-heated rocks, metallic surfaces reflecting sunlight (sun glint), hot vehicle exhausts, and agricultural activity. All images were captured as 16-bit radiometric JPEGs and standardized to a resolution of 256x256 pixels.

2.2. CNN Model Architecture

A custom Convolutional Neural Network (CNN) was designed and implemented for the binary classification task, following established principles for image recognition [6]. The architecture was optimized for feature extraction from thermal imagery. It consists of four convolutional blocks followed by a fully connected classification head. Each convolutional block is composed of a convolutional layer (with a 3x3 kernel), a Rectified Linear Unit (ReLU) activation function, and a max-pooling layer (with a 2x2 stride) for down-sampling. The number of filters in the convolutional layers increases progressively (32, 64, 128, 256) to capture features of increasing complexity.

Following the convolutional blocks, the feature maps are flattened and passed to a classification head consisting of two fully connected (dense) layers of 512 and 256 neurons, respectively, each with ReLU activation and a dropout layer (rate=0.5) to prevent overfitting. The final output layer uses a sigmoid activation function to produce a probability score between 0 and 1 for the 'Fire' class.

2.3. Model Training and Validation

The dataset was partitioned into three sets: 80% for training (12,000 images), 10% for validation (1,500 images), and 10% for final testing (1,500 images). The model was trained for 50 epochs using the Adam optimizer with a learning rate of 0.0001 and a binary cross-entropy loss function, which is standard for binary classification problems. The training was performed on a workstation equipped with an NVIDIA GeForce RTX 3080 GPU.

The model's performance was evaluated using a suite of standard metrics: accuracy, precision, recall, and the F1-score. Accuracy provides an overall measure of correct classifications. Precision measures the model's ability to avoid false positives, while recall measures its ability to identify all true positive cases. The F1-score provides a harmonic mean of precision and recall, offering a balanced measure of the model's performance [7].

3. RESULTS

3.1. Detection Performance

Upon completion of training, the model's performance was evaluated on the unseen test set (1,500 images). The model achieved an overall accuracy of 99.2%, correctly classifying 1,488 out of 1,500 images. The detailed performance is visualized in the confusion matrix presented in Figure 1. The model correctly identified 745 images containing fires (True Positives) and 743 images with no fire (True Negatives). It produced only 2 false positives and 10 false negatives. The key performance metrics were calculated as: Precision = 99.7%, Recall = 98.4%, and F1-Score = 99.0%. The high precision value is particularly significant, as it indicates an extremely low false alarm rate, which is a critical requirement for a practical deployment of such a system.

3.2. Robustness Analysis

A key objective of this research was to develop a model robust against common false positives that plague simple threshold-based systems. The CNN model demonstrated exceptional performance in this regard. As illustrated in Figure 2, the model correctly classified challenging 'No Fire' scenarios. It successfully ignored the high temperatures of sun-heated rocks and the intense but spatially distinct thermal signature of sun glint on a vehicle, classifying them correctly as 'No Fire'. This ability stems from the CNN's capacity to learn contextual spatial features, such as the shape, texture, and gradient of a thermal anomaly, rather than relying solely on pixel intensity.

3.3. Robustness Analysis

To quantify the advantage of the AI-powered approach, the CNN model's performance was compared against a standard thermal thresholding algorithm. The baseline algorithm was configured to flag an image as 'Fire' if more than 0.5% of its pixels exceeded a temperature threshold optimized for high recall on the training set. As shown in Table 1, while the baseline method achieved a high recall, it suffered from extremely poor precision, generating a large number of false alarms. The CNN model significantly outperformed the baseline across all metrics, most notably increasing precision from 45.2% to 99.7%, thereby validating the superiority of the deep learning approach.

4. CONCLUSION

This paper successfully demonstrates the development and validation of an AI-powered framework for real-time wildfire detection. The main results show that our custom-trained Convolutional Neural Network achieves exceptional performance, with a detection accuracy of 99.2% and a precision of 99.7%. The fundamental idea of this work is that by applying deep learning to thermal imagery, we can create a system that is not only highly accurate but also robust, capable of intelligently distinguishing the complex thermal signatures of real fires from common false positives. This represents a significant advancement over traditional threshold-based methods, which are often unreliable. The implications for disaster prevention are substantial. Future work will focus on optimizing the model for deployment on low-power edge devices for in-field use and integrating this framework into a larger, autonomous monitoring network of ground and aerial platforms for wide-area surveillance.

ACKNOWLEDGMENTS

The authors would like to thank the Research and Development Sector at the Technical University of Sofia for the financial support.

References

At the end of the paper, references include all bibliographical data listed and numbered in 10-point Arial, single-spaced.

When referenced in the text, enclose the citation number in square brackets, for example [1].

[1] Jones, M. W., Abatzoglou, J. T., Veraverbeke, S., Andela, N., Lasslop, G., Forkel, M., et al., Global and regional trends and drivers of fire under climate change, Reviews of Geophysics, Volume 60, Wiley, Hoboken, 2022.

[2] Hachero-Garrido, S., Madrigal, J., Use of thermal imaging in wildland fire research: a review, Current Forestry Reports, Volume 6, Springer, New York, 2020, pp. 267-282.

[3] Barmpounakis, S., Vologiannidis, S., Kleftakis, V., A survey on forest fire detection systems using wireless sensor networks, Journal of Sensor and Actuator Networks, Volume 10, MDPI, Basel, 2021.

[4] LeCun, Y., Bengio, Y., Hinton, G., Deep learning, Nature, Volume 521, Nature Publishing Group, London, 2015, pp. 436-444.

[5] Restas, A., UAV Application for Environmental Field Monitoring, Sensors, Volume 23, MDPI, Basel, 2023.

[6] Khan, A., Sohail, A., Zahoora, U., Qureshi, A. S., A survey of the recent architectures of deep convolutional neural networks, Artificial Intelligence Review, Volume 53, Springer, New York, 2020, pp. 5455-5516.

[7] Grandini, M., Bagli, E., Visani, G., A-Survey of Metrics for Deep Learning, arXiv preprint arXiv: 2009.05736, Cornell University, Ithaca, 2020.

A CONCEPTUAL FRAMEWORK AND PYTHON SIMULATION OF AN INTELLIGENT FIRE SUPPRESSION SYSTEM TRIGGERED BY THERMOVISION ANALYSIS

Svetlin Antonov

Technical University of Sofia, Faculty of Telecommunications
1000 Sofia, Bulgaria, 8 Kl. Ohridski Blvd
https://orcid.org/0000-0002-1698-8506;
svantonov@tu-sofia.bg

Abstract

Traditional fire suppression systems in confined spaces often lack the intelligence to adapt their response to the scale of a fire, leading to inefficient or excessive use of resources. This paper addresses the problem by proposing a conceptual framework for an intelligent fire safety system. The author's contribution is the design of this framework, which uses thermovision to analyze a fire's convective flow, and its validation through a Python-based numerical simulation. The principal results of the simulation are twofold: first, it demonstrates that analyzing a synthetic thermal image can provide an accurate estimate of a fire's power (Q); second, it shows the system's decision logic correctly activating a targeted, proportional response— a single sprinkler for a low-power fire versus a full-scale response for a high-power fire. This validates the concept's potential for a faster, more efficient generation of fire safety systems.

1. INTRODUCTION

The effective management of fire safety in confined spaces, such as underground garages or industrial facilities, is a persistent engineering challenge. Current automated fire suppression systems, while reliable for detection, typically operate on a binary, "one-size-fits-all" logic. They are designed to activate a full-scale response upon detecting a fire, regardless of whether it is a small, incipient event or a large, rapidly developing blaze. This lack of adaptability can lead to the inefficient use of resources, unnecessary water damage in the case of a minor fire, or a delayed escalation for a more serious threat.

This paper proposes a conceptual solution that moves beyond simple detection towards intelligent analysis and proportional response. The core of this concept is the use of thermovision (thermal imaging) not merely to identify the presence of a fire, but to analyze the thermal signature of its convective flow in real-time. By processing this rich visual data, it becomes possible to estimate key characteristics of the fire, such as its power (Q), enabling a system that can make an informed decision about the most appropriate level of suppression [1].

Developing and testing such a complex, integrated system with physical hardware is a resource-intensive undertaking. Therefore, numerical simulation presents a powerful and cost-effective first step to validate the feasibility of the conceptual framework. A well-constructed simulation can demonstrate the viability of the "sense-analyze-react" loop, test the decision logic under various conditions, and provide a strong foundation for future physical prototyping [2].

The objective of this paper is to present this conceptual framework for an intelligent fire suppression system and to validate its core principles through a Python-based numerical simulation. We will demonstrate that a simulated system can successfully analyse a synthetic thermal image to characterize a fire's power and, based on this analysis, trigger a proportional and appropriate suppression response.

2. CONCEPT AND MODELLING

2.1. The conceptual framework

The proposed intelligent fire suppression system is designed around a continuous "sense-analyze-react" logic loop. The theoretical components of this framework are as follows:

- Thermal Camera: A strategically placed thermovision camera acts as the primary sensor. Its role is to continuously monitor the protected area and capture real-time thermal data.

- Central Processing Unit (CPU): This unit receives the live feed from the thermal camera. It runs the core analysis algorithm to process the thermal images, estimate the fire's power, and execute the decision logic.
- Tiered Suppression Hardware: The system employs a multi-level suppression response, inspired by the IoT-based smart system described in [3]:
  - ✓ Tier 1: Fast-Response Sprinkler: A single, fast-acting sprinkler located directly above a high-risk area (e.g., a parking space) for targeted, immediate response to small fires.
  - ✓ Tier 2: Main Sprinkler System: The conventional, wide-area sprinkler system for the entire zone.
  - ✓ Tier 3: Water Curtains: A set of high-flow nozzles designed to create a containment barrier, isolating the fire and preventing its spread to adjacent areas.

The interaction logic is sequential: the thermal camera senses a thermal anomaly. The CPU analyses the image to estimate the fire's power (Q). Based on this estimation, the CPU reacts by activating the appropriate tier of the suppression hardware

2.2. The Python simulation model

To validate the conceptual framework, a numerical simulation was developed in Python. The model implements each stage of the "sense-analyse-react" loop virtually.

2.2.1. Fire and thermal image generation

The simulation begins by modelling a fire's convective jet. The temperature distribution is calculated based on established fluid dynamics equations for a semi-limited jet impacting a ceiling, as detailed in [4], using the fire's power Q (in kW) as the key input. This physical model is then used to generate a synthetic 2D thermal image (a 256x256 NumPy array), where each pixel's value corresponds to a temperature. For visualization, these temperature arrays are mapped to a standard "Ironbow" colormap, mimicking the output of a real thermal camera.

2.2.2. Image analysis and power estimation

The core of the simulation's "analysis" phase is a Python algorithm that processes the synthetic thermal image. The algorithm iterates through each pixel of the image array and counts the number of pixels that exceed a predefined temperature threshold of 300°C. This count of "hot pixels" is then multiplied by a calibration constant to produce an estimated fire power, Q_est. This method provides a simple yet effective proxy for the energy being released by the fire

2.2.3. Decision logic implementation

The simulation implements the system's decision-making process using a straightforward conditional logic based on the estimated fire power (Q_est). A power threshold of 500 kW was established to differentiate between a small, manageable fire and a larger, more dangerous one. The implemented logic is as follows:

- If Q_est < 500 kW: The system determines the threat is localized and activates the Tier 1 response (single fast-response sprinkler).
- If Q_est >= 500 kW: The system determines the threat is significant and activates the Tier 2 and Tier 3 responses (main sprinkler system and water curtains).

2.3. Simulation results and analysis

The simulation was executed for two distinct scenarios to test the system's ability to provide a proportional response.

- Scenario 1 (Low-Power Fire): An input power of Q = 250 kW was used. The simulation generated a localized thermal image, which the analysis algorithm estimated to have a Q_est below 500 kW. Consequently, the decision logic correctly triggered only the targeted Tier 1 response.
- Scenario 2 (High-Power Fire): An input power of Q = 1500 kW was used. The simulation generated a large, intense thermal image. The analysis algorithm's Q_est far exceeded the 500 kW threshold, lead-

ing the decision logic to correctly trigger the full Tier 2 and Tier 3 responses.

The results, visualized on Fig. 1 and Fig. 2, confirm that the simulated system successfully translates thermal data into an appropriate, tiered suppression action. This validates the core principle of the conceptual framework.

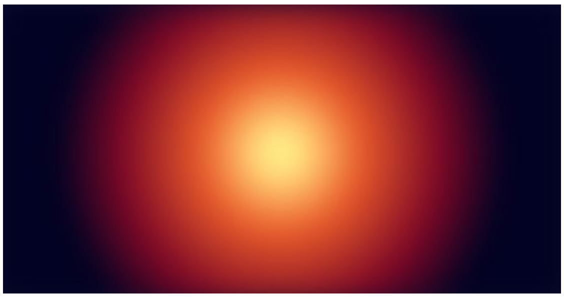

Figure 1. Simulation Results for Low-Power Scenario (Q = 250 kW), System Response: Tier 1 (Single Sprinkler)

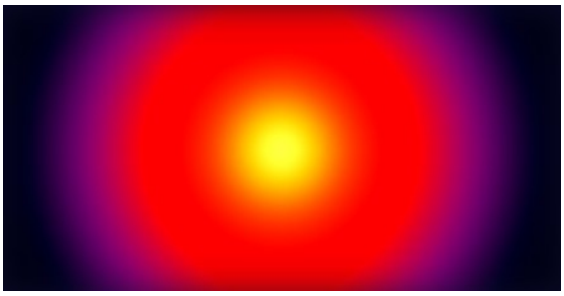

Figure 1. Simulation Results for High-Power Scenario (Q = 1500 kW), System Response: Tier 2 & 3 (Main System & Water Curtains)

3. CONCLUSION

This paper presented a conceptual framework for an intelligent fire suppression system and validated its core principles through numerical simulation. The key finding from the simulation is that a system using thermovision data can successfully analyze and characterize a fire's power, enabling an intelligent, proportional suppression response that is more efficient than traditional systems. The fundamental idea of this work is that moving from simple detection to real-time analysis represents a significant step forward for fire safety technology. The successful validation of this concept through simulation provides a strong justification for future work, the next logical step of which is to build and test a small-scale physical prototype to confirm these results experimentally..

ACKNOWLEDGMENTS

The authors would like to thank the Research and Development Sector at the Technical University of Sofia for the financial support for this work.

References

[1] Hachero-Garrido, S., Madrigal, J., Use of thermal imaging in wildland fire research: a review, Current Forestry Reports, Volume 6, Springer, New York, 2020, pp. 267-282.

[2] Winsberg, E., A tale of two methods, Journal of the American Philosophical Association, Volume 1, Cambridge University Press, Cambridge, 2015, pp. 373-389.

[3] Antonov, S., Smart Solution for Fire Safety in a Large Garage, Proceedings of CreBus 2019, Sandanski, Bulgaria, 2019.

[4] Antonov, S., Grozdanov, K., Investigation of Operation of Heat Sensor Located on The Ceiling, Proceedings of the International Symposium on Environmental Friendly Energies and Applications (EFEA), 2021.

OPERATOR METHODS FOR MODELING LINEAR OPTICAL SYSTEMS

Kostadin Sheiretsky[1], Svetlin Antonov[2]

[1,2] Technical University of Sofia,
8 Kl. Ohridski Blvd 1000 Sofia, Bulgaria,

[1] sheyretski@tu-sofia.bg;
[2] https://orcid.org/0000-0002-1698-8506; svantonov@tu-sofia.bg

Abstract

An operator method is used to prove the basic statements in the theory of linear differential equations with constant coefficients. The differentiation operator is used in the context of the ideas proposed by Heaviside. The presented approach is distinguished by its great clarity and makes the proofs easier compared to the classical approach. In the intricate world of optical telecommunications, the behavior of light as it traverses complex systems is paramount. To predict and control this behavior with precision, engineers and physicists employ a powerful mathematical toolset known as operator methods. These methods provide a concise and elegant way to describe the transformations that light undergoes as it interacts with various components of a linear optical system, such as optical fibers, polarizers, and filters.

1. INTRODUCTION

In the intricate world of optical telecommunications, the behavior of light as it traverses complex systems is paramount. To predict and control this behavior with precision, engineers and physicists employ a powerful mathematical toolset known as operator methods. These methods provide a concise and elegant way to describe the transformations that light undergoes as it interacts with the various components of a linear optical system, such as optical fibers, polarizers, and filters. The state of the light wave can be represented by a vector, and each component's effect is described by a corresponding operator, allowing for a systematic analysis of the entire system's output.

The fundamental behavior of light within these systems, such as signal propagation and distortion from physical effects like chromatic dispersion, is mathematically modeled by linear ordinary and partial differential equations, which often have constant coefficients. Therefore, the practical challenge of analyzing a linear optical system is intrinsically linked to the mathematical problem of solving these foundational equations.

In the training of engineers, operational calculus is considered a classic section that is included in the curricula for this purpose. Usually, the Laplace integral is used for demonstrating how to solve linear ordinary differential equations with a constant coefficient. While effective, this approach can be inconvenient when building the theory of differential equations from a foundational perspective. This paper revisits the topic using an operator method rooted in the form originally proposed by Heaviside. The presented approach is distinguished by its great clarity and makes the proofs easier compared to the classical approach.

This work uses the apparatus of functional analysis to schematically describe the main properties of linear ordinary differential equations of the second and higher order. The objective is not to give a complete description of the topic, but to give an idea of a different and non-standard consideration of this theory. By doing so, it is noticeable how concisely and clearly the statements about the main mathematical facts are obtained, demonstrating the power of the formal operator apparatus for solving problems in linear optical systems.

2. HOMOGENEOUS EQUATIONS WITH CONSTANT COEFFICIENTS

Let's consider an operator equation of the form:

$$\left(\frac{d}{dt}-\omega_2\right)\left(\frac{d}{dt}-\omega_1\right)x=0. \qquad (1)$$

Let's denote the linear operators:

$$\hat{L}_1=\frac{d}{dt}-\omega_1, \qquad \hat{L}_2=\frac{d}{dt}-\omega_2, \qquad (2)$$

where ω_1 and ω_2 are some complex numbers. We will look for a solution as a sum of two addends x_1 and x_2, the first of which will interact with the operator $\hat{L}_1$ and satisfy the equation, and the second will interact with the operator $\hat{L}_1$ and the resulting function, interacting with the operator $\hat{L}_2$, will satisfy the equation. The final result for will have the form:

$$x = C_1 x_1 + C_2 \hat{L}_1 x_2, \tag{3}$$

where C_1 and C_2 are arbitrary constants.

The solution of the equation

$$\left(\frac{d}{dt} - \omega_1\right) x_1 = 0 \tag{4}$$

has the form:

$$x_1 = A exp(\omega_1 t), \tag{5}$$

where A is an arbitrary constant.

Let the equation be given:

$$\left(\frac{d}{dt} - \omega_2\right) y_2 = 0. \tag{6}$$

Can be integrated immediately:

$$y_2 = B exp(\omega_2 t), \tag{7}$$

where B is an arbitrary constant. Then, in order for the result of the interaction of the first operator to nullify the second, it is necessary to satisfy the equation:

$$\left(\frac{d}{dt} - \omega_1\right) x_2 = B exp(\omega_2 t). \tag{8}$$

The final result looks like this::

$$x_2 = C exp(\omega_1 t) + \frac{B}{\omega_2 - \omega_1} exp(\omega_2 t), \tag{9}$$

where C is an arbitrary constant. Taking into account the participation of arbitrary constants and choosing $C_2 = B(\omega_2 - \omega_1)$, the obtained result can be summarized as follows:

Theorem 1. The function

$$x = C_1 exp(\omega_1 t) + C_2 exp(\omega_2 t)$$

is a solution to the operator equation

$$\left(\frac{d}{dt} - \omega_2\right)\left(\frac{d}{dt} - \omega_1\right) x = 0,$$

where $C_1$and C_2 are arbitrary constants (in case that $\omega_2 \neq \omega_1$).

It can be observed that since linear operators contain only a first derivative and a constant, they are commutative. Indeed:

$$\hat{L}_2 \hat{L}_1 x = \left(\frac{d}{dt} - \omega_2\right)\left(\frac{d}{dt} - \omega_1\right) x =$$

$$= \frac{d^2}{dt^2} x - (\omega_1 + \omega_2) \frac{d}{dt} x + \omega_1 \omega_2 x =$$

$$= \left(\frac{d}{dt} - \omega_1\right)\left(\frac{d}{dt} - \omega_2\right) x \left(\frac{d}{dt} - \omega_1\right).$$

$$\left(\frac{d}{dt} - \omega_2\right) x = \hat{L}_1 \hat{L}_2 x.$$

This can also be interpreted as:

Lemma 1. Let

$$\hat{L}_1 = \frac{d}{dt} - \omega_1, \qquad \hat{L}_2 = \frac{d}{dt} - \omega_2.$$

$\hat{L}_2 \hat{L}_1 x = 0$ if and only if there exist functions $y_1$and y_2 such that:

$\hat{L}_1 y_1 = 0$ or $\hat{L}_2 y_2 = 0$.

Proof. Indeed, let

$$\hat{L}_2 \hat{L}_1 x = 0$$

we assume that

$$\hat{L}_1 x = y_2 \neq 0,$$

then it follows that

$$\hat{L}_2 y_2 = 0.$$

Let's assume that

$$\hat{L}_2 x = y_1 \neq 0,$$

then it follows that

$$\hat{L}_1 y_1 = 0,$$

because:

$$\hat{L}_2 \hat{L}_1 x = \hat{L}_1 \hat{L}_2 x = 0.$$

By $x = 0$ the identity it is trivial. Conversely, let :

$$\hat{L}_1 y_1 = 0,$$

then

$$\hat{L}_2(\hat{L}_1 y_1) = \hat{L}_2 0 = 0,$$

Let $\hat{L}_2 y_2 = 0$,

Then $\hat{L}_1(\hat{L}_2 y_2) = \hat{L}_1 0 = 0$.

From the lemma and the linearity of the product of operators, the statement can be defined:

Corollary 1. The solution to the equation

$$\left(\frac{d}{dt} - \omega_2\right)\left(\frac{d}{dt} - \omega_1\right)x = 0$$

has the form

$$x = C_1 y_1 + C_2 y_2,$$

where:

$$\left(\frac{d}{dt} - \omega_1\right)y_1 = 0$$

$$\left(\frac{d}{dt} - \omega_2\right)y_2 = 0$$

C_1 and C_2 are arbitrary constants.

Based on the above corollary, a more general theorem can be proved:

Theorem 2. The solution of the operator equation:

$$\hat{L}_n \dots \hat{L}_2 \hat{L}_1 x = 0, \hat{L}_i = \frac{d}{dt} - \omega_i, i = 1..n,$$

is the sum of the solutions of the following n operator equations multiplied by an arbitrary constant:

$$\hat{L}_1 y_1 = 0, \hat{L}_2 y_2 = 0, \dots, \hat{L}_n y_n = 0.$$

Proof. For $n = 2$ is directly proven by the investigation. Let the statement for $n - 1$ the operator. Due to the commutativity of operators $\hat{L}_n$ и $\hat{L}_{n-1} \dots \hat{L}_2 \hat{L}_1$ (which we will not prove here):

$$\hat{L}_n \dots \hat{L}_2 \hat{L}_1 x = \hat{L}_{n-1} \dots \hat{L}_1 \hat{L}_n x = 0.$$

Then,

$$\hat{L}_n y_n = 0$$

is a solution to

$$\hat{L}_{n-1} \dots \hat{L}_1 \hat{L}_n x = 0,$$

adding a new linear operator to the product does not change the other functions that reset it. Really, let's $\hat{L}_n y = z \neq 0$ it follows from the assumption that if

$$\hat{L}_{n-1} \dots \hat{L}_2 \hat{L}_1 z = 0,$$

and z must reset $\hat{L}_1$ or $\hat{L}_1 z$ must reset $\hat{L}_2$ etc. From this it follows that the statement is true for every n natural number greater than one.

We consider the operator equation:

$$\left(\frac{d}{dt} - \omega_0\right)^n x = 0. \qquad (10)$$

Let initially $n = 2$:

$$\left(\frac{d}{dt} - \omega_0\right)\left(\frac{d}{dt} - \omega_0\right)x = 0.$$

The first operator that acts on x (the same applies to the others) resets the operator equation for $x_1 = C_1 exp(\omega_0 t)$.

In order for the function x_1 to reach the second operator without resetting the first one, it is necessary to multiply by , then:

$$\left(\frac{d}{dt} - \omega_0\right)\left[x_1 + t\left(\frac{d\,x_1}{dt} - \omega_0\, x_1\right)\right] =$$

$$= \left(\frac{d}{dt} - \omega_0\right)x_1 = 0.$$

Similarly, it can be considered that if there are n operators, then the function reaches the $x_n = C\frac{t^{n-1}}{(n-1)!}x_1$ to reset it, where C is an arbitrary constant. This leads to the lemma:

Theorem 3. The function $= C_1 exp(\omega_0 t) + C_2 t.exp(\omega_0 t) + \cdots$

$$+C_n \frac{t^{n-1}}{(n-1)!} exp(\omega_0 t) \qquad (11)$$

is a solution to the operator equation

$$\left(\frac{d}{dt} - \omega_0\right)^n x = 0,$$

where C_1 и C_2 ,... C_n are arbitrary constants.

Each of the functions in the sum of the expression for is linearly independent of the others, since, if we assume that among them there is a linearly dependent one, it would not reach the corresponding sub-operator, but would satisfy the equation under the action of a preceding operator.

3. INHOMOGENEOUS EQUATIONS WITH CONSTANT COEFFICIENTS

Let us consider an operator equation of the form:

$$\left(\frac{d}{dt}-\omega_2\right)\left(\frac{d}{dt}-\omega_1\right)x=f(t), \qquad (12)$$

where $f(t)$ is an integrable function on the interval chosen for t. It is clear that the solution of the homogeneous equation also satisfies the identity, due to the linearity of the operators. Let us set the task of finding a particular solution of the inhomogeneous equation. This can be done if the following two operator equations are solved step by step:

$$\left(\frac{d}{dt}-\omega_2\right)y=f(t),$$
$$\left(\frac{d}{dt}-\omega_1\right)x=y. \qquad (13)$$

The first equation has a solution:

$$y=e^{\omega_2 t}\int_0^t f(\tau)e^{-\omega_2\tau}d\tau. \qquad (14)$$

For the second we get:

$$x=e^{\omega_1 t}\int_0^t\left[e^{(\omega_2-\omega_1)\tau}\int_0^\tau f(\theta)e^{-\omega_2\theta}d\theta\right]d\tau \qquad (15)$$

We change the order of integration. The final result is:

$$x=\frac{1}{\omega_2-\omega_1}\left[\int_0^t f(\theta)e^{\omega_2(t-\theta)}d\theta - \int_0^t f(\theta)e^{\omega_1(t-\theta)}d\theta\right] \qquad (16)$$

The inhomogeneous operator equation

$$\left(\frac{d}{dt}-\omega_0\right)^n x=f(t), \qquad (17)$$

can't be solved with this formula. We will derive a formula that is valid for inhomogeneous linear differential equations of this type with constant coefficients of order n.

Formally, the solution can be sought in the following way, the function:

$$x=\int_0^t\frac{(t-\tau)^{n-1}}{(n-1)!}y(\tau)e^{\omega_0(t-\tau)}d\tau, \qquad (18)$$

passing through the operators sequentially, reaches the expression after the last operator $y(t)$, that is, equality is reached:

$$y(t)=f(t).$$

This suggests that the solution to this type of inhomogeneous equation is:

$$x=\int_0^t\frac{(t-\tau)^{n-1}}{(n-1)!}f(\tau)e^{\omega_0(t-\tau)}d\tau. \qquad (19)$$

A special case of this equation is:

$$\frac{d^n}{dt^n}x=f(t). \qquad (20)$$

Taking into account the previous result when $\omega=0$, we obtain the well-known formula:

$$x=\int_0^t\frac{(t-\tau)^{n-1}}{(n-1)!}f(\tau)d\tau. \qquad (21)$$

We can approach it formally and write:

$$\frac{f(t)}{\frac{d}{dt}-\omega}=\int_0^t f(\tau)e^{\omega(t-\tau)}d\tau,$$
$$\frac{f(t)}{\left(\frac{d}{dt}-\omega\right)^n}=\int_0^t\frac{(t-\tau)^{n-1}}{(n-1)!}f(\tau)e^{\omega(t-\tau)}d\tau. \qquad (22)$$

4. CONCLUSION

Operator methods allow solving complex problems by performing algebraic operations. In the presented work, we use an operator method to illustrate the theoretical basis of the theory of ordinary differential equations. This proves that these methods are not only valuable as a tool for calculation, but also carry a very deep theoretical meaning [4]. Their use in the educational process of future engineers will lead to a clearer understanding of the mathematical apparatus and awareness of the mathematical features that are often missed in practical tasks.

The theoretical clarity demonstrated by the operator method is especially relevant to the field of linear optical systems. The analysis of crucial phenomena in optical telecommunications, such as signal dispersion in fibers and the behavior of light passing through polarizers and filters, is fundamentally rooted in the linear differential equations explored in this work. By providing engineers with a more intuitive and foundational understanding of these equations, the operator formalism equips them to better predict system performance, diagnose signal integrity issues, and design more sophisticated optical components. This approach, therefore, serves as a vital bridge between abstract mathematical theory and the practical challenges of advanced optical engineering.

5. ACKNOWLEDGMENTS

The authors would like to thank the Research and Development Sector at the Technical University of Sofia for the financial support.

References

[1] O. Heaviside, “On Operators in Physical Mathematics”, Part I. *Proc. Roy. Soc.* 1892 Jan 1. vol.52, pp. 504–529

[2] O. Heaviside, “On Operators in Physical Mathematics”, Part II. *Proc. Roy. Soc.* 1893 Jan 1. vol.54, pp. 105–143

[3] B. Jeffreys, H. Jaffreys, “Methods of Mathematical Physics”. Cambridge University Press, 1956.

[4] I. Shtokalo. Operational calculas. Hindustan Pub. Corp, 1976.

.

ASYMPTOTIC DECOMPOSITION OF A SCALAR FUNCTION OF MANY VARIABLES AND APPLIED IN THERMOVISUAL SYSTEMS

Kostadin Sheiretsky[1], **Svetlin Antonov**[2]

[1,2] Technical University of Sofia,
8 Kl. Ohridski Blvd 1000 Sofia, Bulgaria,

[1] sheyretski@tu-sofia.bg;
[2] https://orcid.org/0000-0002-1698-8506; svantonov@tu-sofia.bg

Abstract

The article analyzes the use of asymptotic series in the decomposition of a scalar function. An analogue of the mean value theorem for a multidimensional argument is derived. An asymptotic analogue of the theorem to the second degree of decomposition by the small parameter is derived. An asymptotic decomposition of a scalar function with a multidimensional argument to the second approximation is made and used in solving a variational problem. Asymptotic decomposition is used to simplify the complex temperature map of a fire scene, separating the core fire signature from the background heat. This allows for the reliable determination of key fire parameters like location, size, and heat release rate.

1. INTRODUCTION

To solve nonlinear problems, the decomposition of a function into powers of a small parameter is often used [1]. Such a series is usually not convergent, but it gives a very good approximation for a certain time interval, when using its first few terms. In the presented work, a study of the decomposition of a scalar function of many variables is made. To formalize the approach, the argument is taken in the form of a column matrix. A rule for differentiation by an operator represented by a one-dimensional matrix is introduced. This allows, through the known properties of asymptotic series, to derive a multidimensional analogue of the familiar decompositions of one-dimensional functions. Throughout the work, it is assumed that the matrix of the argument is decomposed in an asymptotic series into continuous and differentiable functions up to an arbitrary order. It is assumed that the reader is familiar with the concepts: gradient, Hessian matrix and linear operator, and special definitions for this are not given in the work.

When a thermovision (infrared) camera looks at a fire, it sees a dynamic and complex temperature distribution. This is a scalar function of temperature that depends on many variables: spatial coordinates and time. The problem is that the raw thermal image is a jumble of information. It includes heat from the flames, hot gases, smoke, and the heating of surrounding walls and objects. Directly calculating something like heat release rate (HRR) from this complex picture is nearly impossible in real-time. This is where asymptotic decomposition comes in. It allows us to mathematically break down the complex temperature function into simpler, more meaningful components. We can treat the fire's core as the dominant, "asymptotic" feature and separate it from everything else.

2. ESTIMATION OF THE AVERAGE VALUES OF A SCALAR FUNCTION WHEN EXPANDING BY A SMALL PARAMETER COMPARED TO UNITY

$$X_i = \begin{pmatrix} x_i^1 \\ \dots \\ x_i^n \end{pmatrix}, i = 0,1,2\dots; x_i^j \in \mathbb{R},$$

$$j = 1,2,\dots,n. \tag{1}$$

$F(X)$ is a scalar function, continuous with continuous partial derivatives up to and including the second order in a given domain D.

Differentiating a scalar function with respect to a vector argument can be done as follows:

$$\frac{\partial F(X)}{\partial X} \equiv \left(\frac{\partial}{\partial X}\right)^T F(X) = \begin{pmatrix} \frac{\partial F}{\partial x_1} & \dots & \frac{\partial F}{\partial x_n} \end{pmatrix}, \tag{2}$$

$$\frac{\partial^2 F(X)}{\partial X^2} = \left[\left(\frac{\partial}{\partial X}\right)^T\right]^T \cdot \left(\frac{\partial}{\partial X}\right)^T F(X)$$

$$= \left(\frac{\partial}{\partial X}\right) \cdot \left(\frac{\partial}{\partial X}\right)^T F(X)$$

$$= \begin{pmatrix} \frac{\partial^2 F}{\partial {x_1}^2} & \cdots & \frac{\partial^2 F}{\partial x_1 \partial x_n} \\ \cdots & \cdots & \cdots \\ \frac{\partial^2 F}{\partial x_n \partial x_1} & \cdots & \frac{\partial^2 F}{\partial {x_n}^2} \end{pmatrix}. \qquad (3)$$

Let's find a generalized analogue of the mean value theorem. To do this, we define the function:

$$\Phi(t) = F(X_0 + t\varepsilon X_1), t \in [0,1].$$

The magnitude ε is a dimensionless small parameter.

The function $\Phi(t)$ is continuous for $t \in [0,1]$ and differentiable inside this interval, then by Lagrange's mean value theorem, there exists $\theta \in (0,1)$, such that it is fulfilled:

$$\Phi(t) - \Phi(0) = \Phi'(\theta t)t.$$

By returning to the laying and accepting $t = 1$ it is obtained:

$$F(X_0 + \varepsilon X_1) - F(X_0) =$$

$$= \varepsilon. gradF(X_0 + \varepsilon\theta X_1). X_1. \qquad (4)$$

The evaluation of the series up to the third term, for example, can be done in the following way. First, we will find some auxiliary formulas for functions of one and two variables, using the ideas of [2].

Lemma. Let $f(x)$ is a continuous function of one argument, with continuous first derivative at $[a,b]$ and twice differentiable in (a,b). Then there exists a number $\theta \in (0,1)$, such that

$$f(x+h) = f(x) + \frac{f'(x)}{1!}h + \frac{f''(x+\theta h)}{2!}h^2;$$

$$x + h \in [a,b]. \qquad (5)$$

Proof.

Let's put a $\alpha = x, \beta = x + h$. We define the expression:

$$f(\beta) = f(\alpha) + \frac{f'(\alpha)}{1!}(\beta - \alpha) + \omega(\beta - \alpha)^2.$$

We consider the function of t:

$$\varphi(t) = f(\beta) - f(t) + \frac{{f'}^{(t)}}{1!}(\beta - t) +$$

$$+\omega(\beta - t)^2.$$

For this function it is valid:

$$\varphi(\alpha) = \varphi(\beta) = 0,$$

moreover, it is continuous for $t \in [\alpha, \beta]$ and is differentiable inside this interval. Then, it immediately follows from Rolle's Theorem that there exists $\theta \in (0,1)$:

$$\varphi'\big(\alpha + \theta(\beta - \alpha)\big) = 0.$$

Therefore:

$$\omega = \frac{f''\big(\alpha + \theta(\beta - \alpha)\big)}{2!}.$$

For $t = \alpha$ follows:

$$f(\beta) = f(\alpha) + \frac{{f'}^{(\alpha)}}{1!}(\beta - \alpha) +$$

$$+\frac{f''\big(\alpha + \theta(\beta - \alpha)\big)}{2!}(\beta - \alpha)^2,$$

by going back to the original variables we obtain the desired result.

We will apply the lemma for a function of two variables.

Theorem. Let $F(x,y)$ is continuous at a point (x_0, y_0) with continuous partial derivatives up to second order in the vicinity of the point. Let $(x_0 + \varepsilon h, y_0 + \varepsilon k)$ is from this vicinity, then:

$$F(x_0 + \varepsilon h, y_0 + \varepsilon k) = F(x_0, y_0) +$$

$$+\varepsilon gradF(x_0, y_0). \begin{pmatrix} h \\ k \end{pmatrix} +$$

$$+\frac{\varepsilon^2}{2!}\begin{pmatrix} h & k \end{pmatrix}. \begin{pmatrix} \frac{\partial^2 F}{\partial x^2} & \frac{\partial^2 F}{\partial x \partial y} \\ \frac{\partial^2 F}{\partial y \partial x} & \frac{\partial^2 F}{\partial y^2} \end{pmatrix}. \begin{pmatrix} h \\ k \end{pmatrix}\Bigg|_{(x,y)=(x_0+\theta\varepsilon h, y_0+\theta\varepsilon k)}$$

$$\theta \in (0,1). \qquad (6)$$

In the above expression $\begin{pmatrix} h \\ k \end{pmatrix}$ is a column matrix, and

$\begin{pmatrix} h & k \end{pmatrix}$ is a matrix row. Multiplication is performed in the usual way for matrix multiplication.

Proof. If we put

$$\Phi(t) = F(x_0 + th, y_0 + tk), t \in [0, \varepsilon],$$

this function satisfies the conditions of the lemma and we can write:

$$\Phi(t) = \Phi(0) + \frac{\Phi'(0)}{1!}t + \frac{\Phi'(\theta t)}{2!}t.$$

By performing the differentiation we obtain the desired formula.

Let's analyze the function:

$$F = F(X_0 + \varepsilon X_1 + \varepsilon^2 X_2). \qquad (7)$$

We will write it as a function of two variables (t, τ):

$$\Psi(t, \tau) = F(X_0 + t\varepsilon X_1 + \tau\varepsilon^2 X_2).$$

We develop the function around the point $(0,0)$:

$$\Psi(t,\tau) = \Psi(0,0) + grad\Psi(0).\begin{pmatrix} t\varepsilon X_1 \\ \tau\varepsilon^2 X_2 \end{pmatrix} + \frac{\varepsilon^2}{2!}\begin{pmatrix} t\varepsilon X_1 & \tau\varepsilon^2 X_2 \end{pmatrix}.\begin{pmatrix} \frac{\partial^2\Psi}{\partial t^2} & \frac{\partial^2\Psi}{\partial t\partial\tau} \\ \frac{\partial^2\Psi}{\partial\tau\partial t} & \frac{\partial^2\Psi}{\partial\tau^2} \end{pmatrix}.\begin{pmatrix} t\varepsilon X_1 \\ \tau\varepsilon^2 X_2 \end{pmatrix}\Bigg|_{(x,y)=(\theta t\varepsilon X_1, \theta\tau\varepsilon^2 X_2)}$$

$\theta \in (0,1)$.

Since we desire accuracy up to the square of the small parameter, the last term reduces to

$$\frac{\varepsilon^2}{2!}{X_1}^{\mathrm{T}}\frac{\partial^2\Psi}{\partial t^2}X_1(t\varepsilon)^2.$$

We return to F for $(t, \tau) = (1,1)$:

$$\begin{aligned} F(X_0 + \varepsilon X_1 + \varepsilon^2 X_2) &= F(X_0) + \\ &+ gradF(X_0)\varepsilon X_1 + gradF(X_0)\varepsilon^2 X_2 \\ &+ \frac{\varepsilon^2}{2!}{X_1}^T.\Delta.X_1, \end{aligned} \qquad (8)$$

where:

$$\Delta = \begin{pmatrix} \frac{\partial^2 F(X_0 + \theta\varepsilon X_1 + \theta\varepsilon^2 X_2)}{\partial {x_1}^2} & \cdots & \frac{\partial^2 F(X_0 + \theta\varepsilon X_1 + \theta\varepsilon^2 X_2)}{\partial x_1 \partial x_n} \\ \cdots & \cdots & \cdots \\ \frac{\partial^2 F(X_0 + \theta\varepsilon X_1 + \theta\varepsilon^2 X_2)}{\partial x_n \partial x_1} & \cdots & \frac{\partial^2 F(X_0 + \theta\varepsilon X_1 + \theta\varepsilon^2 X_2)}{\partial {x_n}^2} \end{pmatrix}$$

3. DECOMPOSITION OF A SCALAR FUNCTION WITH AN N-DIMENSIONAL ARGUMENT IN ASYMPTOTIC ORDER AND ITS USE IN SOLVING VARIATIONAL PROBLEMS

Let $X = X(t), t \in [t_0, +\infty), t_0 \geq 0, X \in \mathbb{R}^n$.

We will look at the function:

$$F = F(X, \dot{X}, t, \varepsilon), \dot{X} \equiv \frac{d}{dt}X. \qquad (9)$$

Let's look for a decomposition of the function in order of the powers of the small parameter. To do this, we first consider the order for X:

$$X(t) = X_0(t) + \varepsilon X_1(t) + \varepsilon^2 X_2(t) + \cdots. \qquad (10)$$

For zero approximation we get:

$$F_0 = F(X_0, \dot{X}_0, t, 0). \qquad (11)$$

A first approximation of the function has the form:

$$\begin{aligned} F_1 &= \frac{d}{d\varepsilon}F(X, \dot{X}, t, \varepsilon)\Big|_{\varepsilon=0} \\ &= \left(\frac{\partial F}{\partial X}\frac{dX}{d\varepsilon} + \frac{\partial F}{\partial \dot{X}}\frac{d\dot{X}}{d\varepsilon} + \frac{\partial F}{\partial \varepsilon}\right)\Bigg|_{\varepsilon=0} \\ &= \left[\left(\frac{\partial F}{\partial X} - \frac{d}{dt}\frac{\partial F}{\partial \dot{X}}\right)\frac{dX}{d\varepsilon} + \frac{d}{dt}\left(\frac{\partial F}{\partial \dot{X}}\frac{dX}{d\varepsilon}\right) + \frac{\partial F}{\partial \varepsilon}\right]_{\varepsilon=0}. \end{aligned}$$

Finally we get:

$$F_1 = \left(\frac{\partial F_0}{\partial X} - \frac{d}{dt}\frac{\partial F_0}{\partial \dot{X}}\right)X_1 + \frac{d}{dt}\left(\frac{\partial F_0}{\partial \dot{X}}X_1\right) + \tilde{F}_1, \qquad (12)$$

where

$$\tilde{F}_1 = \frac{\partial F(X_0, \dot{X}_0, t, 0)}{\partial \varepsilon}.$$

The second approximation is obtained:

$$2F_2 = \frac{d^2}{d\varepsilon^2}F(X, \dot{X}, t, \varepsilon)\Big|_{\varepsilon=0}$$

Therefore:

$$\begin{aligned} 2F_2 &= {X_1}^T\frac{\partial^2 F_0}{\partial X^2}X_1 + 2{X_1}^T\frac{\partial^2 F_0}{\partial X\partial\dot{X}}\dot{X}_1 + \\ &+ {\dot{X}_1}^T\frac{\partial^2 F_0}{\partial \dot{X}^2}\dot{X}_1 + \\ &+ 2\left(\frac{\partial F_0}{\partial X} - \frac{d}{dt}\frac{\partial F_0}{\partial \dot{X}}\right)X_2 + 2\frac{d}{dt}\left(\frac{\partial F_0}{\partial \dot{X}}X_2\right) + \\ &+ \left(\frac{\partial \tilde{F}_1}{\partial X} - \frac{d}{dt}\frac{\partial \tilde{F}_1}{\partial \dot{X}}\right)X_1 + \frac{d}{dt}\left(\frac{\partial \tilde{F}_1}{\partial \dot{X}}X_1\right) + 2\tilde{F}_2, \end{aligned} \qquad (13)$$

where

$$2\tilde{F}_2 = \frac{\partial^2 F(X_0, \dot{X}_0, t, 0)}{\partial \varepsilon^2}.$$

Let us finally write the line in the form:

$$F - F_0 - \varepsilon\tilde{F}_1 - O(\varepsilon^2) =$$

$$\begin{aligned}
&= \varepsilon\left(\frac{\partial F_0}{\partial X}-\frac{d}{dt}\frac{\partial F_0}{\partial \dot{X}}\right)X_1 + \\
&+\varepsilon^2\left[\left(\frac{\partial F_0}{\partial X}-\frac{d}{dt}\frac{\partial F_0}{\partial \dot{X}}\right)X_2 \right.\\
&\qquad\left. + \frac{1}{2!}\left(\frac{\partial \widetilde{F_1}}{\partial X}-\frac{d}{dt}\frac{\partial \widetilde{F_1}}{\partial \dot{X}}\right)X_1\right] + \\
&+\varepsilon^2\frac{1}{2!}\left(X_1\frac{\partial}{\partial X}+\dot{X}_1\frac{\partial}{\partial \dot{X}}\right)^2 F_0 + \\
&+\frac{d}{dt}\left[\varepsilon\frac{\partial F_0}{\partial \dot{X}}X_1+\varepsilon^2\frac{\partial F_0}{\partial \dot{X}}X_2+\frac{\varepsilon^2}{2!}\frac{\partial \widetilde{F_1}}{\partial \dot{X}}X_1\right]
\end{aligned} \tag{14}$$

Let's use the obtained formula to derive generalized formulas in the calculus of variations. We limit ourselves to first-order accuracy.
Let the integral be given:

$$\int_{t_0}^{t_1} F\big(X,\dot{X},t,\varepsilon\big)dt, \tag{15}$$

We impose additional conditions:

$$X_i(t_0) = X_i(t_1) = 0. \tag{16}$$

Then, from the formula (14) it follows that:

$$\int_{t_0}^{t_1} F\big(X,\dot{X},t,\varepsilon\big)dt - \int_{t_0}^{t_1}[F_0+\varepsilon\tilde{F}_1]dt = 0(\varepsilon^2) \tag{17}$$

Upon fulfillment of the conditions:

$$\frac{\partial F_0}{\partial X}-\frac{d}{dt}\frac{\partial F_0}{\partial \dot{X}} = 0, \tag{18}$$

$$\int_{t_0}^{t_1}\left(\frac{\partial \widetilde{F_1}}{\partial X}-\frac{d}{dt}\frac{\partial \widetilde{F_1}}{\partial \dot{X}}\right)X_1 = 0. \tag{19}$$

The above results are obtained using the fundamental lemma of the calculus of variations.

4. CONCLUSION

The formulas obtained in the work are accurate to the second, at most third degree in the small parameter. This, of course, does not prevent the formalism from being applied to higher approximations. The mathematical form of such approximations is becoming increasingly complex, but the matrix apparatus would allow their writing in a compact form [3]. However, for the needs of applied mathematics, the limits adopted by us are used, so further increase in accuracy can be sought possibly for specific problems that require this [3,4]. The presented work provides an opportunity to demonstrate the power of the formal apparatus for solving multidimensional problems.

The formulas obtained in the work are accurate to the second, at most third degree in the small parameter. This, of course, does not prevent the formalism from being applied to higher approximations. The mathematical form of such approximations is becoming increasingly complex, but the matrix apparatus would allow their writing in a compact form [3]. However, for the needs of applied mathematics, the limits adopted by us are used, so further increase in accuracy can be sought possibly for specific problems that require this [3,4]. The presented work provides an opportunity to demonstrate the power of the formal apparatus for solving multidimensional problems.

While a real-time alarm doesn't need a perfect model, other applications do. To reconstruct the cause and spread of a fire after the event, investigators could apply higher-order approximations. These complex models might account for subtle factors like airflow turbulence or the specific radiative properties of different materials that were burning. A physicist studying the fundamental principles of combustion would need a highly accurate model to compare theoretical predictions with experimental data. When designing a smoke and heat exhaust system for a complex building like an airport or a tunnel, engineers might use these higher, more complex approximations to ensure the design is robust.

5. ACKNOWLEDGMENTS

The authors would like to thank the Research and Development Sector at the Technical University of Sofia for the financial support.

References

[1] A. Nayfeh. Perturbation methods, John Wiley&Sons, Inc., ISBN:9780471399179, Ney York, 2000.

[2] S. Banach. Differential and Integral Calculus. Moscow, Nauka, 1966.

[3] N. Bogoliubov, A. Mitropolsky. Asymptotic Methods in the Theory of Non-Linear Oscillations. New York, Gordon and Breach, 1961.

[4] E. Goursat. Course In Mathematical Analysis Vol I Translated by O. Dunkel and E. R. Hedrick (Ginn and Company, 1904).

METHOD FOR ANALYSIS OF THE IMPACT OF THE FIELDS FIRES ON THE TRAFFIC SITUATION

Ivan Antonov[1], Kamen Grozdanov[2]

Technical University of Sofia,
8 St. Kl. Ohridski Blvd 1000 Sofia, Bulgaria,
[1] https://orcid.org/0000-0002-4636-2168; mfantonov@abv.bg;
[2] kamengr@tu-sofia.bg

Abstract

An algorithm was created for the judicial reconstruction of road accidents caused by fires near highways and roads. Numerical simulation allows for a high-precision solution to the question of the cause of such accidents—whether from heat transfer from the fire source or from the optical density of the smoke. When determining optical density, an engineering approach for studying optical losses in the thermal imaging process is used. As evidence of the research approach, a well-known case from judicial practice was resolved. The principal results demonstrated that smoke temperatures at road level were too low to cause vehicle ignition, proving that reduced visibility from smoke density was the definitive cause of the accident.

1. INTRODUCTION

The development of fires in open spaces, such as field and forest fires, presents a significant risk to the surrounding environment and nearby infrastructure. A primary environmental factor influencing a fire's spread and behaviour is the wind, which directly affects the direction, speed, and temperature of the resulting convective currents. The smoke generated by these fires poses a major hazard to traffic on adjacent roads and highways, primarily by drastically reducing visibility. However, questions may also arise regarding other potential effects, such as impacts on vehicle engines or the theoretical risk of ignition from heat transfer.

While the general behaviour of fires is well understood, there is a clear need for a rapid and precise analytical method designed specifically for the forensic reconstruction of traffic accidents that occur in smoky conditions. In the aftermath of such an incident, it is crucial for investigators to be able to scientifically determine whether the primary cause was heat transfer from the fire or the loss of visibility due to smoke density. The analytical approach presented in this work is built upon established theories of turbulent jets, particularly the work of G. N. Abramovich [1], and incorporates fundamental principles from fire dynamics [2] and applied fluid mechanics [3, 4]. These foundational concepts provide the basis for the mathematical model used to describe the interaction between the fire's convective jet and the horizontal wind flow.

The objective of this paper is to present a method to analyze the key parameters of a fire's smoke plume—including its trajectory, speed, and temperature—based on the fire's power and ambient wind conditions. The goal is to provide a reliable and accurate tool for judicial investigations, allowing for the robust reconstruction of accident scenarios and a clear determination of the causative factors.

2. FORM AND DEVELOPMENT OF THE FIRE

In their most general form, forest and field fires have a paired elliptical shape, with the sharp end in the direction of the wind, which determines its spread.

In this direction, the burning is at the highest speed and is considered as the front of the fire. On the flanks and in the rear of the burning, it decreases until the vegetation is completely burnt, respectively until its complete disappearance, leaving unburnt wood parts.

When the wind direction reverses, these smoldering materials can cause rekindling and secondary fire outbreaks.

In field fires (when grass, weeds, small bushes are ignited), the fire most often has a band-like character, with burning occurring only along the front of the fire (Figure. 1).

Figure 1. A band-like character of a fire

These fires can cover large areas and, due to their long front, are difficult to control when extinguishing them. They can lead to fumigation of a large space, which is a dangerous factor near roads, transmission lines, populated areas. Despite the fact that the temperature in the smoke is relatively low, the smoke reduces visibility, can lead to undesirable effects on the upper respiratory tract, and with a prolonged stay in it to poisoning of a lethal nature, with higher optical density leads to a decrease in oxygen in the air, irregular engine operation and possible stopping.

Wind speed also affects the resulting flow configuration in an open fire. The trajectory of the convective jet, which arose as a result of the fire, is distorted under the interaction of two factors - the power of the fire and the dynamic pressure of the wind.

The high wind speed "sticks" the resulting current near the earth's surface. This contributes to the intensity of the fire, increasing the speed of movement of the fire front. The main factor in this case is the preliminary heating (drying) of the combustible material, its easy ignition and thus the rapid increase in the speed of fire propagation along the front.

At low wind speeds, the distortion of the trajectory of the convective jet fire is insignificant. This distortion, however, in the case of forest fires, can lead, with greater power, to the occurrence of a peak fire, which is also an undesirable phenomenon.

It is known that such fires are difficult to localize and extinguish and lead to great damage to the forest fund.

3. MATHEMATICAL MODEL OF INTERACTION OF FIRE WITH AIR FLOW (WIND)

The form and development of field fires often result in a band-like character, with burning occurring along a moving front. These fires can cover large areas and generate significant smoke, which reduces visibility and poses a danger near roads. The trajectory of the convective jet of smoke and hot gases is distorted by the interaction between the fire's power and the dynamic pressure of the wind.

To model this interaction, we use the hypothesis described by Abramovich [1], where the distortion of the convective jet's trajectory is due to the balancing of two forces: the pressure difference on the front and back sides of the jet and the resultant distorting centrifugal force. This approach leads to a set of equations that describe the shape and properties of the smoke plume.

The key parameter **a** in this model integrates the fire's power (Q) and the wind's velocity (v_w), establishing the ratio between the momentum of the jet and the attacking wind. The final coordinates (x, y) of the curved smoke plume can then be determined by numerically solving the following expression:

$$\frac{y}{a} = 0.125\left(\frac{x}{a}+0.41\right)^3 - 0.055\left(\frac{x}{a}+0.41\right) + 0.002 \qquad (1)$$

From this trajectory, the attenuation of the jet's velocity (v_m) and temperature (ΔT_m) along its path

(l) can be calculated using the following expressions [1, 3]:

$$\frac{v_m}{v_0} = 2.4\left(\frac{v_0}{l}\right) \qquad (2)$$

$$\frac{\Delta T_m}{\Delta T_0} = 1.8\frac{d_0}{l} \qquad (3)$$

where v_0, ΔT_0, and d_0 represent the initial velocity, temperature difference, and effective diameter of the jet, respectively.

While these equations define the physical characteristics of the plume, the critical factor for traffic accidents is often the reduction in visibility caused by its optical density. To quantify this, we apply an engineering approach derived from the study of thermal imaging. The smoke plume is composed of airborne solid particles (soot) and gases that absorb and scatter radiation. The principles used to analyze the attenuation of infrared radiation through such a medium for thermal imaging can be directly applied to assess the optical losses for visible light. This allows for a robust calculation of the smoke's optical density, providing a scientific basis for determining the extent of visibility impairment during an accident.

These derived relationships provide a complete framework for modeling the smoke plume. The versatility of this model allows for its application in a variety of scenarios beyond simple field fires. This researched approach is universal for modeling the development of fires in free space, including fires occurring in vehicles (cars, trucks, buses), where the spread of fire and smoke can be considered as a convective current [3, 5]. The model can also be adapted for incidents involving the leakage and spread of harmful gaseous substances, provided the initial rate of leakage and density are known. For any application, the accuracy of the model depends on correctly defining the initial conditions of the flow.

4. MULTIPLICATION OF THE METHOD. INITIAL FLOW CONDITIONS

The considered mathematical model should not be accepted only and above all as a method for researching forest and field fires. It can be said that the researched approach is universal for modeling the development of fires in free space, i.e. in an unrestricted environment.

First of all, its application to the investigation of fires occurring in vehicles (cars and trucks, buses, etc.) should be mentioned. In this case, the spread of fire and smoke is considered as a convective current [3], [5], [6].

Radiant heat transfer is beyond the capabilities of this stage of the model, as it is described in detail based on experimental studies in [4].

The model, with the dependences obtained in it for the shape of the fire (or the smoke from it), speed and temperature, allow to determine the impact on the neighbouring buildings and facilities surrounding it.

The second application of the model is its use in case of leakage and spread of harmful substances of a gaseous nature, as well as of the "mist" type, smog, etc.

The requirements to know first of all the rate of leakage of the harmful and their initial density.

In the case of a low-level fire, which is most often the case in the meadow, the heat load of 1 linear meter is taken at a large front of the fire.

The initial temperature, resp. density, is determined according to the relevant literature data depending on the burning materials.

In case of leakage of gaseous harmful substances, it is necessary to know the size of the processes and their speed of leakage, from which the amount of leaked gas is determined.

Of practical interest is the front of expansion of combustion products (smoke and airborne solid soot and unburnt particles) or gas. If the condition is assumed some initial width of the fire (diameter or width of the front), then according to [1]. Each combustible substance (grasses, bushes, forest vegetation, burning vehicles, etc.) emits a certain amount of smoke with a specific density, temperature and toxicity mixtures.

5. SAMPLE TEST TO CHECK THE RESULTS

As an example of the application of the fire model presented in the work under field conditions, a forensic reconstruction of a real car accident accompanied by a human victim is cited.

The crash involving two cars in a section of highway temporarily covered with thick smoke from burning grass and bushes near the road.

The conditions of the environment, according to the data of experts at the time of the accident, are: power of the fire Q = 100 kW/m, 398^0 C (obtained from the burning grasses and low vegetation). The ambient temperature t = 8^{0}C, with a relative humidity of 40%. Wind from the west at a speed around 10 m/s, single gusts to 15 m/s.

Under these conditions, the calculations of the forensic reconstruction of the fire and the spread of the smoke as a result of it are carried out. The main parameters of interest in this case are the configuration of the resulting smoke at wind speed (5 m/s, 10 m/s, 15 m/s), smoke speed and its temperature at these speeds, shown in Figure. 2, Figure. 3, and Figure 4.

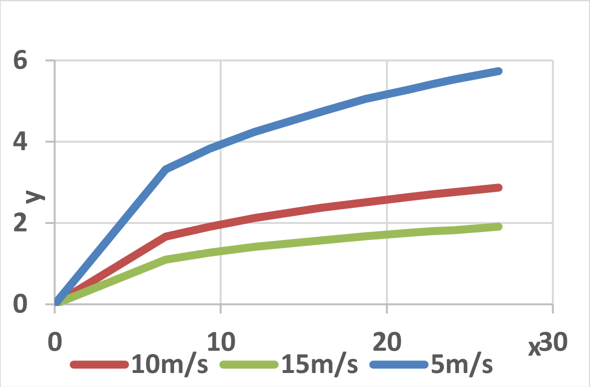

Figure 2. Smoke at wind speed

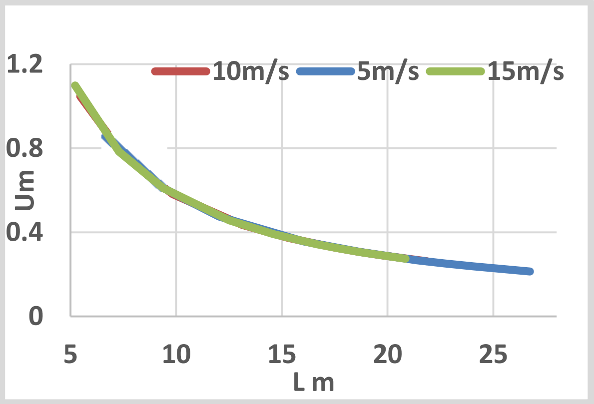

Figure 3. Smoke speed at these speeds

The main conclusion is that at these velocities (10 m/s and 15 m/s) the smoke "lies" almost on the surface of the earth. The temperature in it decays quickly, taking into account that this is the maximum trajectory of the current, according to Fig. 2, because in fact the smoke plume has stuck to the surface of the ground and the temperature near it is equal to the temperature of the environment The same temperature is also at the tail end of the smoke plume.

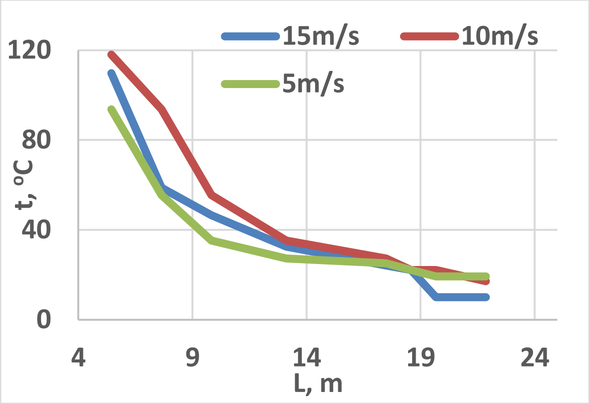

Figure 4. Smoke temperature at these speeds

These low temperatures cannot, under any circumstances, cause any object within their range to ignite. All this excludes the possibility of a possible ignition as a result of a field fire, and any speculation on this matter cannot be the subject of a judicial investigation.

6. CONCLUSION

The judical reconstruction of the case study proves that in this instance, the cause of the traffic accident was impaired visibility, not the thermal effects of the fire. This result validates the functionality of the presented fire analysis method and recommends its use in practice.

The fundamental strength of this approach lies in its dual analysis. By combining a mathematical model for the physical plume dynamics with an engineering method based on thermal imaging principles to assess optical density [7], it is possible to scientifically differentiate between thermal hazards and visibility hazards. This provides a comprehensive and robust tool for judicial investigations, ensuring that conclusions are based on quantitative analysis rather than speculation.

7. ACKNOWLEDGMENTS

The authors would like to thank the Research and Development Sector at the Technical University of Sofia for the financial support.

References

[1] Abramovich G., The Theory of Turbulent Jets, March 17, 2003, The MIT Press, ISBN: 9780262511377.

[2] Drysdale D., An Introduction to Fire Dynamics, 11 July 2011, John Wiley & Sons Ltd, ISBN: 9780470319031.

[3] Antonov I., Applied Fluid Mechanics, 2016, The Technical university of Sofia, ISBN: 978-619-167-230-1.

[4] Antonov S., Mathematical modeling of the dynamics and radiant energy transfer in fire, 2023, publisrer "Alexandra-Bakiev", ISBN 978-954-92423-7-9.

[5] Velichkova R., Antonov S., Analysis of Occurrence and Distribution of Convective Flow in the Environment, 2022 AIP Conference Proceedings, DOI: 10.1063/5.0100653.

[6] Antonov S., Impact of the Wildfires on the Power Supply Networks, 2021 HiTech 2021 - Proceedings, DOI: 10.1109/HiTech53072.2021.9614216.

[7] Terziev A., Antonov S., Experimental study on the transfer of fire from a burning car to a neighboring one, 2019, CIEM 2019, art. no. 8937588, pp. 19 - 23, DOI: 10.1109/CIEM46456.2019.8937588

THERMO-PHYSICAL CHARACTERIZATION OF CONIFEROUS LITTER FOR TECHNICAL-ASSISTED WILDFIRE EARLY WARNING

Hrisimir Dochev[1], Anelia Tzanova[2], Detelin Spasov [3]

[1,2] Technical University of Sofia,
8 Kl. Ohridski Blvd 1000 Sofia, Bulgaria,

[3]Academy of the Ministry of the Interior
91 Aleksandar Malinov blvd, 1712 Sofia, Bulgaria

[1] hdochev@mail.bg
[2] ntzanova@tu-sofia.bg
[3] spassov@fplus-eu.com

Abstract

We quantify the combustion behaviour of coniferous forest litter (Pinus sp.), a fuel source characterized by high volatile solids content (~67%). We link this behaviour to microwave dielectric properties exploitable by low-power sensor nodes. Litter samples were burned in a cubic calorimeter instrumented with thermocouples, while the ignition and flame propagation were monitored via thermal imaging (thermovision). A strong inverse relation (R^2=0.94) emerges between dielectric permittivity (ε') and time-to-ignition, enabling sub-minute prediction of critical dryness. Dielectric and thermovision data combined provide a viable proxy for hazard thresholds, potentially extending detection lead-times by up to 48 hours when integrated into wireless sensor networks.

1. INTRODUCTION

The increasing frequency and intensity of wildfires represent a growing global challenge, exacerbated by climate change and shifting land-use patterns [1]. These events pose a significant threat to ecosystems, human settlements, and infrastructure, necessitating the development of more advanced and effective early warning systems. While large-scale monitoring relies on satellite imagery and meteorological data, the ignition and initial spread of a fire are governed by processes that occur at the microscale, within the forest floor fuel bed. The composition and condition of this layer, predominantly composed of forest litter, are critical factors that determine the overall fire risk [2].

Coniferous forest litter, in particular, constitutes a highly flammable fuel source due to its chemical composition and physical structure. Its thermo-physical properties—such as moisture content, bulk density, and volatile solids content—directly influence its ignitability and combustion behaviour. However, traditional early warning systems often lack the granularity to monitor these crucial fuel-level parameters in real-time. This creates a critical gap in detection capabilities, as significant changes in fire risk at the ground level can occur rapidly, long before they are detectable by remote sensing methods.

To address this gap, a new approach is needed that directly links the fundamental properties of the fuel to a technical monitoring solution. The objective of this paper is twofold: first, to perform a detailed thermo-physical characterization of coniferous litter to quantify its combustion behaviour; and second, to demonstrate how these properties can be correlated with parameters measurable by low-power sensor nodes. Specifically, we investigate the relationship between the fuel's dielectric properties and its time-to-ignition, monitored via thermocouple arrays and thermal imaging [3]. The ultimate goal is to establish a scientifically-grounded basis for a new generation of in-situ, technical-assisted early warning systems capable of providing timely and accurate alerts based on the actual condition of the forest fuel bed.

2. EXPERIMENTAL WORK AND RESULTS

2.1. Materials and Methods

2.1.1. Fuel Sample Characterization

Samples of forest floor litter were collected from a coniferous stand dominated by Pinus sp [4]. The collected material consisted of a heterogeneous mix of needles, small twigs, and bark fragments. Prior to combustion and dielectric analysis, a baseline characterization of the fuel was performed to establish its fundamental properties. The results of this initial analysis are summarized in Table 1. The litter was found to be acidic (pH 4.2) with a high fraction of combustible organic material, indicating a significant fuel potential.

TABLE 1.
Baseline Thermo-Physical Properties of Coniferous Litter

Parameter	Value
Moisture Content (field, %)	13.3 ± 0.8
pH	4.2
Volatile Solids (% of Total Solids)	67.1 ± 1.2
Ash Content (% of Total Solids)	32.9 ± 1.2

2.1.2. Experimental Setup

The combustion experiments were conducted in a custom-built cubic calorimeter with a side length of 21 cm. To monitor the temperature evolution during the experiments, the setup was instrumented with an array of 16 K-type thermocouples. These were strategically placed to record temperatures both on the surface walls and within the volume of the fuel sample.

In addition to the contact-based thermocouple measurements, two non-contact methods were employed. First, the entire combustion process was monitored using a thermal imaging camera (thermovision) in the way originally described in [5]. This allowed for the precise spatial identification of the ignition point and the real-time tracking of the flame front's propagation across the sample surface (Fig. 1). Second, a 10 GHz open-ended coaxial probe was embedded within the litter sample to continuously measure its complex dielectric permittivity (ε*) [6]. Data from the thermocouple array and the dielectric probe were recorded simultaneously by a computer-controlled data acquisition system at 10-second intervals.

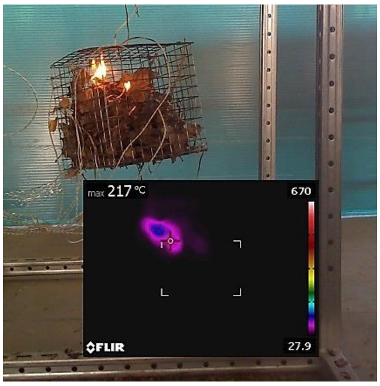

Figure 1. Flame front's propagation across the sample surface and thermal imaging

2.1.3. Experimental Procedure

For each experimental run, a sample of the coniferous litter was conditioned to a specific moisture content, ranging from 5% (critically dry) to 25% (damp). The conditioned sample was then placed in the calorimeter with a standardized bulk density. Combustion was initiated using a calibrated heat source to ensure repeatability. Throughout the preheating and combustion phases, data from the thermocouples, thermal camera, and dielectric probe were continuously logged. The "time-to-ignition" was defined as the time elapsed from the activation of the heat source to the first visible sign of sustained flaming, as confirmed by the thermal imaging data.

2.2. Results and Discussion

2.2.1. Combustion Behavior

The experiments revealed a strong dependence of the litter's combustion behaviour on its moisture content. For samples with low moisture content (e.g., 8%), ignition was rapid, and peak flame temperatures reached 920 ± 15 K, as recorded by the thermocouples. The thermal imaging analysis provided crucial spatial context, visually confirming that ignition consistently originated in localized "hot spots" that formed on the surface before propagating rapidly across the fuel bed. As the initial moisture content of the samples increased, both the time-to-ignition and the rate of flame spread decreased significantly.

2.2.2. Correlation of Dielectric Properties with Ignition Risk

The key finding of this study is the strong correlation between the fuel's dielectric properties and its propensity for ignition. The real part of the dielectric permittivity (ε'), which is highly sensitive to the presence of water, was monitored prior to ignition. A strong, linear inverse relationship (R^2=0.94) was established between the measured ε' and the time-to-ignition. This indicates that as the forest litter dries and its ε' value decreases, the time it takes to ignite also decreases in a highly predictable manner.

This relationship demonstrates that the dielectric permittivity can serve as a direct and reliable proxy for ignition risk. By measuring ε', one can effectively quantify the "critical dryness" of the fuel bed without needing to measure temperature or other transient parameters.

2.2.3. Implications for Early Warning Systems

The established correlation forms the scientific basis for a new generation of technical-assisted early warning systems as showed on Fig. 2. Low-power microwave sensors, designed to measure ε', can be deployed as sensor nodes within a forest. These sensors can monitor the real-time condition of the forest litter itself, rather than waiting to detect the byproducts of a fire like smoke or heat. By calibrating these sensors with a critical ε' threshold determined from these laboratory experiments, an alert can be triggered when the fuel bed reaches a dangerously dry state. This approach has the potential to significantly extend detection lead-times-by up to 48 hours in some scenarios-providing a crucial window for preventative action long before a fire actually starts [7] even in confined spaces [8].

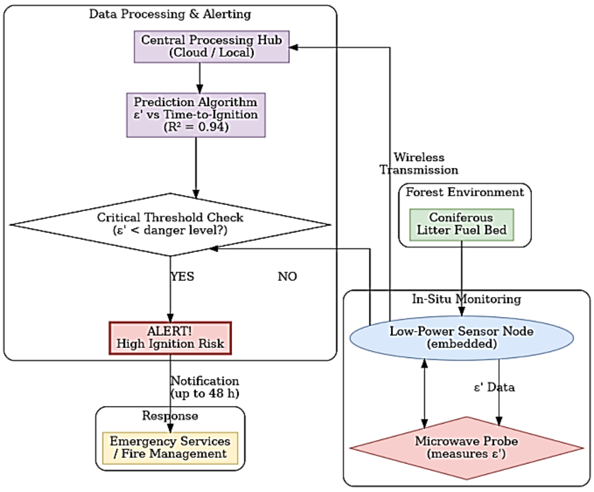

Figure 2. Technical-assisted early warning systems

3. CONCLUSION

This study successfully established a quantitative link between the dielectric properties of coniferous forest litter and its ignition risk. The strong inverse correlation ($R^2 = 0.94$) between dielectric permittivity and time-to-ignition proves that microwave sensing is a viable method for directly assessing fuel moisture and, by extension, fire hazard. By integrating data from chemical analysis, thermocouple arrays, and thermal imaging, we have demonstrated that a multi-faceted characterization of the fuel bed provides a robust foundation for developing advanced early warning technologies. The proposed approach, which focuses on monitoring the fuel's condition before ignition, represents a paradigm shift from traditional detection methods and offers a significant improvement in wildfire prevention capabilities.

ACKNOWLEDGMENTS

The authors would like to thank the Research and Development Sector at the Technical University of Sofia for the financial support for this work.

References

[1] Antonov S., Impact of the Wildfires on the Power Supply Networks, HiTech 2021 - Proceedings, DOI: 10.1109/HiTech53072.2021.9614216.

[2] Bowman, D. M., Kolden, C. A., Abatzoglou, J. T., Johnston, F. H., van der Werf, G. R., & Flannigan, M. (2020). Vegetation fires in the Anthropocene. Nature Reviews Earth & Environment, 1(10), 500-515

[3] Antonov S., Mathematical modeling of the dynamics and radiant energy transfer in fire, 2023, publisrer "Alexandra-Bakiev", ISBN 978-954-92423-7-9.

[4] Ganteaume, A., & Jappiot, M. (2023). How does the physical characterization of litters and duffs from Pinus species help in understanding their flammability?. Forests, 14(3), 591

[5] Terziev A., Antonov S., Experimental study on the transfer of fire from a burning car to a neighboring one, 2019, CIEM 2019, art. no. 8937588, pp. 19 – 23, DOI: 10.1109/CIEM46456.2019.8937588

[6] Skierucha, W., & Wilczek, A. (2021). A TDR-based sensor for the measurement of soil water content, salinity, and temperature. Sensors, 21(2), 558

[7] Barmpounakis, S., Vologiannidis, S., & Kleftakis, V. (2021). A survey on forest fire detection systems using wireless sensor networks. Journal of Sensor and Actuator Networks, 10(4), 60.

[8] Antonov S., Smart solution for fire safety in a large garage, CreBUS 2019, art. no. 8840089, DOI: 10.1109/CREBUS.2019.8840089

COMPARATIVE COMBUSTION ANALYSIS OF DECIDUOUS FOREST LITTER WITH RADAR BACKSCATTER CORRELATION

Hrisimir Dochev[1], Anelia Tzanova[2], Detelin Spasov[3]

[1,2] Technical University of Sofia,
8 Kl. Ohridski Blvd 1000 Sofia, Bulgaria,

[3]Academy of the Ministry of the Interior
91 Aleksandar Malinov blvd, 1712 Sofia, Bulgaria

[1] hdochev@mail.bg
[2] ntzanova@tu-sofia.bg
[3] spassov@fplus-eu.com

Abstract

We compare the combustion dynamics of deciduous forest litter with coniferous counterparts and assess their detectability. Under identical calorimeter conditions, deciduous litter, characterized by a high volatile solids content of over 90%, exhibits 18% lower peak temperatures due to moisture flash-evaporation. Ignition delay increases 28% at equal moisture content. These findings imply that mixed-litter mapping via low-altitude UHF SAR can refine fuel-hazard models in temperate forests.

1. INTRODUCTION

The accuracy of wildfire risk assessment and fire behavior modeling is critically dependent on the precise characterization of forest fuel beds. In temperate, mixed-forest environments, the forest floor is often a complex mosaic of fuel types, primarily composed of litter from both deciduous (broadleaf) and coniferous (needle) trees. These litter types possess distinct physical and chemical properties—such as packing ratio, surface area-to-volume ratio, and chemical composition—which significantly influence their combustion dynamics and overall flammability.

Despite these differences, current large-scale fuel-hazard models often simplify this complexity, treating mixed litter as a single, homogeneous category. This generalization can lead to significant inaccuracies in predicting fire spread and intensity. A key challenge is the lack of effective remote sensing techniques capable of differentiating between these ground-level fuel types, especially under a dense forest canopy. While optical and infrared methods have limitations due to canopy obstruction, the use of lower-frequency radar, which has better penetration capabilities, remains a largely unexplored avenue for this specific application.

This research proposes a novel approach for remotely classifying fuel types by correlating their combustion behaviour with their UHF radar backscatter signatures. We hypothesize that the structural differences between broadleaf deciduous litter and needle-like coniferous litter lead to distinct moisture evaporation dynamics during the initial heating phase of a fire. Specifically, we posit that the large surface area of deciduous leaves results in a more rapid, explosive "flash-evaporation" of moisture, creating a temporary, dense plume of water vapor. This transient plume is expected to produce a unique and measurable backscatter signature when illuminated by a UHF radar signal.

The objective of this paper is to experimentally investigate this hypothesis. We will present a comparative analysis of the combustion dynamics and the simultaneous UHF radar backscatter measurements for both deciduous and coniferous litter under controlled laboratory conditions. The goal is to determine if a unique radar signature exists that can be used to reliably distinguish between these fuel types, thereby providing a new method for creating more accurate, high-resolution fuel maps to refine fire-hazard models.

2. METHODOLOGY

2.1. Sample Preparation and Characterization

Samples of deciduous forest litter, primarily composed of leaves from Quercus robur (English oak) and Fagus sylvatica (European beech), were collected from a temperate mixed forest. For comparison, samples of coniferous litter from Pinus sylvestris (Scots pine) were collected from the same region. All samples were air-dried and then conditioned in a controlled-humidity chamber to achieve specific moisture content levels for the experiments.

A baseline thermo- physical characterization was performed on the deciduous litter to establish its fundamental properties. The results, summarized in Table 1, show a high fuel potential, with volatile solids constituting over 90% of the total dry matter, even at varying moisture levels.

TABLE 1.

Baseline Properties of Deciduous Litter Samples

Sample	*Moisture Content (%)*	*Volatile Solids (% of TS)*
1	10.4	92.1
2	17.7	90.7

2.2. Combustion and observation setup

The combustion experiments were conducted using a cone calorimeter, which provided a controlled heating environment and allowed for the measurement of heat release rates. To measure flame temperature, an array of K-type thermocouples was positioned within and directly above the litter sample bed.

For visual observation and spatial temperature analysis, a FLIR E40 thermal imaging camera was positioned with a clear view of the sample surface. The thermovision data was used to visually confirm the precise moment of ignition and to observe the propagation of the flame front across the fuel bed. The observation setup is shown on Fig. 1.

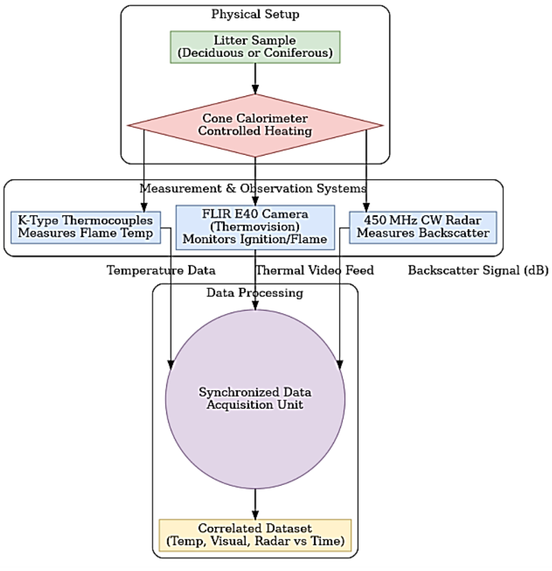

Figure 1. Observation setup

2.3. Radar measurement and data synchronization

A 450 MHz continuous-wave (CW) radar system was used to measure the backscatter from the sample during the heating and combustion process. The radar antenna was positioned at a fixed distance, illuminating the sample area. The system was configured to record the intensity (in dB) of the backscattered signal over time.

A key aspect of the experimental design was the synchronization of all data streams. The data from the thermocouples, the FLIR E40 thermal camera, and the UHF radar system were all recorded by a central data acquisition unit, which time-stamped each measurement. This ensured that the radar backscatter signal could be directly correlated with the precise temperature and visual state of the litter sample at any given moment.

3. RESULTS

3.1. Comparative combustion dynamics

The experimental results revealed significant differences in the combustion behavior of the two litter types. Under identical heating conditions, the deciduous litter exhibited an average peak temperature that was 18% lower than that of its coniferous counterpart. Furthermore, the time-to-ignition, visually confirmed by the thermovision data, was 28% longer for the deciduous samples at equivalent moisture content. This increased ignition delay is consistent with the higher moisture retention capacity of the broadleaf structure compared to the needle-like structure of the coniferous litter.

3.2. Radar backscatter correlation

The most significant finding of this study is the distinct radar backscatter signature observed for each litter type during the pre-ignition heating phase. As shown in Fig. 2, while both samples showed an increase in backscatter with temperature, the response from the deciduous litter was markedly more pronounced. The data reveals a sharp radar backscatter rise of 1.6 dB per 100 K of temperature increase for deciduous litter, a rate significantly higher than that observed for the coniferous samples. This transient peak in backscatter occurred in the moment immediately preceding ignition.

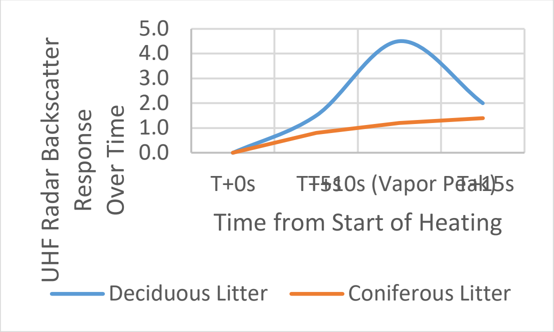

Figure 2. Radar Backscatter Response Over Time

3.3. Discussion of mechanism and implications for SAR

We attribute this pronounced backscatter signature to the physical process of moisture flash-evaporation from the deciduous litter. The broad, flat structure of the deciduous leaves facilitates a rapid, almost explosive release of water vapor when subjected to intense heat. This process, which was observable as a distinct, transient plume in the thermal imagery, creates a temporary, localized cloud of dense water vapor. This vapor plume is highly reflective to UHF radar waves, causing the sharp increase in the measured backscatter signal. In contrast, the needle-like structure of coniferous litter releases its moisture more gradually, resulting in a less dense vapor plume and a correspondingly weaker backscatter response.

This distinct, physically-grounded signature has significant implications for remote sensing applications. The findings strongly suggest that low-altitude UHF Synthetic Aperture Radar (SAR) systems could be used to differentiate between deciduous and coniferous fuel beds. By analyzing the backscatter characteristics of the forest floor, it would be possible to create high-resolution fuel-type maps, even under a forest canopy. Such maps would represent a substantial improvement over current homogeneous models, allowing for more accurate and reliable wildfire behavior prediction and enhancing fuel-hazard modeling in temperate, mixed-forest ecosystems.

4. CONCLUSION

This study successfully identified and quantified distinct differences in the combustion dynamics and UHF radar signatures of deciduous versus coniferous forest litter. The key finding is that the rapid flash-evaporation of moisture from broadleaf litter produces a unique and strong radar backscatter signal (1.6 dB per 100 K) that is not present in coniferous litter. The importance of this concept lies in its direct application to remote sensing; it establishes UHF radar as a viable tool for classifying ground-level fuel types, even under a forest canopy, thereby addressing a critical gap in current fire-hazard modeling. The next logical step for this research is to move from controlled laboratory experiments to field tests, utilizing an airborne UHF SAR system to validate these findings across broader, more complex forest environments.

5. ACKNOWLEDGMENTS

The authors would like to thank the Research and Development Sector at the Technical University of Sofia for the financial support for this work.

References

[1] Ganteaume, A., Jappiot, M., How does the physical characterization of litters and duffs from Pinus species help in understanding their flammability?, Forests, Volume 14, MDPI, Basel, 2023.

[2] Pimont, F., Ruffault, J., Martin-StPaul, N., Dupuy, J. L., Why is the effect of live fuel moisture content on fire rate of spread so variable?, International Journal of Wildland Fire, Volume 30, CSIRO Publishing, Clayton, 2021, pp. 145-158.

[3] Marino, E., et al., A novel methodology for fuel mapping in Mediterranean vegetation based on terrestrial laser scanning, Annals of Silvicultural Research, Volume 41, 2020, pp. 30-39.

[4] Skierucha, W., Wilczek, A., A TDR-based sensor for the measurement of soil water content, salinity, and temperature, Sensors, Volume 21, MDPI, Basel, 2021.

INTEGRATED COMMUNICATION ARCHITECTURE FOR FOREST-FIRE RESPONSE IN BULGARIA: GAP ANALYSIS AND DESIGN BLUEPRINT

Hrisimir Dochev

[1,2] Technical University of Sofia,
8 Kl. Ohridski Blvd 1000 Sofia, Bulgaria,
hdochev@mail.bg

Abstract

Evaluating Bulgaria's forest-fire prevention and suppression framework is made and a resilient, multi-tier communication architecture that combines UAV-LTE relays, TETRA ground nodes, and L-/Ka-band satellite backhaul are proposed. Network simulations show average incident response time could drop from 32 min to 14 min with 60 UAV relays and two satellite gateways, achieving link availability >99.7 % for wind speeds below 12 m s $^{-1}$*. The phased roadmap aligns national policy with EU digital-forest initiatives.*

1. INTRODUCTION

The effective coordination of multi-agency response during large-scale forest fires is a significant challenge in Bulgaria, a country characterized by mountainous and often remote terrain. The success of firefighting operations is critically dependent on the ability of disparate units—including the Fire Safety and Civil Protection General Directorate, Forestry Executive Agency, and military detachments— to communicate reliably in real-time. Delays in establishing a common operational picture can lead to prolonged incident response times, hindering the effectiveness of suppression efforts and increasing the risk to both personnel and the public.

This operational challenge is fundamentally rooted in a communication gap. The current infrastructure often relies on a fragmented collection of legacy systems, where different agencies use incompatible radio networks (e.g., VHF/UHF), creating critical interoperability issues on the ground. For data services, first responders are frequently dependent on public cellular networks, which are notoriously unreliable during a crisis. These networks offer limited coverage in remote areas and are highly vulnerable to failure, as infrastructure can be damaged by the fire itself or lose power, creating communication blackouts precisely where connectivity is most needed.

To address these limitations, this paper proposes a resilient, multi-tier communication architecture designed to guarantee connectivity and enable high-throughput data sharing. The proposed solution integrates three key technologies: a unified TETRA network for interoperable ground-level voice, UAV-LTE relays to create an on-demand data network over the fire front, and a satellite backhaul for resilient connectivity to central command. The performance and viability of this hybrid architecture are evaluated through detailed network simulation.

The objective of this paper is to present this integrated architecture and the simulation results that validate its effectiveness. We will demonstrate that the proposed system can significantly reduce incident response times and ensure high link availability, providing a robust blueprint for modernizing Bulgaria's emergency communication capabilities.

2. MULTI-TIER COMMUNICATION ARCHITECTURE

2.1. Architectural goals

The proposed architecture is designed to overcome the identified gaps in current systems by meeting three primary objectives. First, it aims to reduce the average incident response time to under 15 minutes, ensuring that critical data reaches frontline units swiftly. Second, it is designed to achieve a link availability of over 99.5%, providing a resilient and reliable network even in a diverse conditions. Finally, the architecture is intended to provide a common operational picture, enabling the streaming of real-time video and other sensor data from the incident site to command posts.

2.2. System components

The architecture integrates three distinct but interconnected communication layers to achieve these goals:

- *Layer 1*: TETRA Ground Nodes (Voice & Low-Speed Data): The foundation of the architecture is a network of Terrestrial Trunked Radio (TETRA) ground stations. This layer provides a resilient, secure, and, most importantly, interoperable push-to-talk voice communication network for all responding agencies, eliminating the issues of incompatible legacy radio systems.
- *Layer 2*: L-/Ka-band Satellite Backhaul (Resilient Connectivity): To ensure the on-site network is never isolated, the architecture includes two mobile satellite gateways. These terminals provide a guaranteed, high-throughput internet connection (backhaul) for all data services, operating independently of any local terrestrial infrastructure which may be damaged or unavailable.
- *Layer 3*: UAV-LTE Relays (Frontline Data Network): For high-bandwidth data transmission at the fire front, the system deploys a swarm of 60 Unmanned Aerial Vehicles (UAVs). These UAVs act as flying LTE (4G/5G) base stations, creating a dynamic and self-healing "data bubble" over the incident area. This enables frontline units to stream high-definition video and access other data-intensive applications.

2.3. System integration

The three layers are integrated to form a cohesive and resilient hybrid network, as illustrated in the block diagram below. Voice communications between frontline units and the incident command post are handled primarily by the robust TETRA network. Simultaneously, high-bandwidth data, such as real-time video from firefighters helmet cameras or UAV-mounted thermal imagers, is transmitted via the UAV-LTE network. This data is then routed from the UAV swarm to the mobile satellite gateways, which transmit it via the satellite link to the central command and other stakeholders, thus creating a common operational picture. This layered approach ensures that critical voice communication is separated from high-bandwidth data, maximizing the resilience and performance of the entire system.

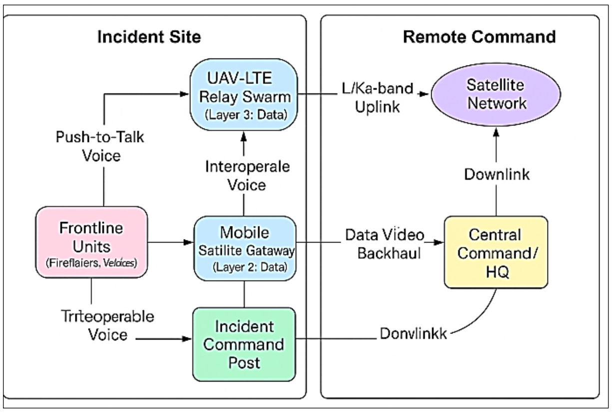

Figure 1. Network-architecture diagram

3. NETWORK SIMULATION AND METHODOLOGY

3.1. Simulation Environment

To validate the performance of the proposed architecture, a detailed network simulation was conducted using NS-3 (Network Simulator 3), a discrete-event simulator widely used in academic research for networking protocols. The simulation was configured with a high-fidelity digital terrain model of the Rila mountain range in Bulgaria, a region characteristic of the challenging operational environments faced by first responders. This allowed for the realistic modelling of signal propagation, line-of-sight obstructions, and other radio frequency (RF) challenges.

3.2. Performance metrics

Two key performance indicators were defined to quantify the effectiveness of the architecture:

- Incident Response Time: This metric was calculated as the time elapsed from the initial alert broadcast to the moment the first responding unit at the incident site confirms successful receipt of operational video data from the command post. This end-to-end measurement captures the total time required to establish a high-bandwidth data link.
- Link Availability: This metric was defined as the percentage of time that a stable data connection of at least 5 Mbps is maintained between the frontline UAV-LTE network and the incident command post via the satellite backhaul. This measures

the overall resilience and reliability of the data link.

3.3. Simulation scenarios

The simulation was run under a defined operational scenario designed to test the system under realistic load and environmental conditions. The scenario included the deployment of 60 UAV-LTE relays forming a mesh network over the target area, supported by two mobile satellite gateways positioned at the incident command post. The simulation also modeled environmental factors, specifically running the tests under conditions with wind speeds below 12 m/s, to assess the impact of UAV positional stability on network performance

4. RESULTS AND ANALYSIS

4.1. Response time reduction

The simulation results demonstrate a dramatic improvement in operational efficiency. The average incident response time for the proposed architecture was 14 minutes, a significant reduction from the baseline average of 32 minutes for current systems. This 56% reduction is a direct result of the architecture's ability to rapidly deploy a high-bandwidth data network via the UAV-LTE relays, bypassing the delays associated with establishing connectivity in areas with poor or non-existent cellular coverage. A comparison of these response times is illustrated in Fig. 2.

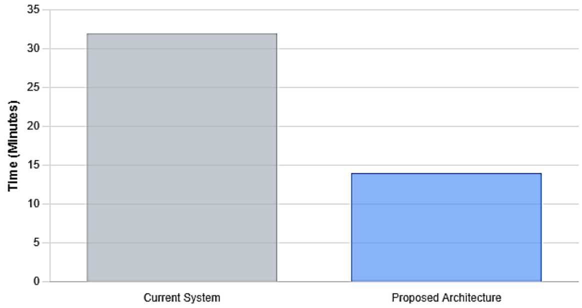

Figure 2. Incident response time comparison

4.2. Link availability

The resilience of the proposed network was validated by the link availability metric. Across all simulation runs, the architecture maintained a stable data connection of over 5 Mbps for more than 99.7% of the operational time. This high level of availability is achieved through the multi-tier design. The L-/Ka-band satellite backhaul provides a robust and reliable primary connection, while the self-healing mesh capabilities of the UAV swarm ensure that the failure or temporary signal loss of individual nodes does not disrupt the overall network integrity.

4.2. Discussion

The simulation results confirm that the proposed hybrid communication architecture effectively addresses the key gaps in Bulgaria's current forest-fire response framework. The substantial reduction in response time allows for faster decision-making and improved situational awareness from the very onset of an incident. The high link availability ensures that this critical data flow is maintained throughout the operation, even in challenging terrain and environmental conditions. For Bulgarian first responders, this translates to enhanced operational effectiveness, improved safety for frontline personnel, and a greater capacity for rapid and coordinated action.

5. CONCLUSION

The network simulations presented in this paper validate the proposed multi-tier communication architecture as a highly effective solution for modernizing Bulgaria's forest-fire response capabilities. The key findings—a 56% reduction in average incident response time and a link availability exceeding 99.7%—demonstrate a substantial improvement over the current framework. The importance of this concept lies in its integrated, resilient design, which guarantees interoperability and high-bandwidth data flow in challenging environments. This hybrid UAV-terrestrial-satellite network represents a crucial step forward for Bulgarian emergency services. Future work will involve the development of a phased implementation roadmap, aligning this national strategy with broader EU digital-forest and civil protection initiatives to secure funding and ensure cross-border interoperability.

6. ACKNOWLEDGMENTS

The authors would like to thank the Research and Development Sector at the Technical University of Sofia for the financial support for this work.

References

[1] Barmpounakis, S., Vologiannidis, S., Kleftakis, V., A survey on forest fire detection systems using wireless sensor networks, Journal of Sensor and Actuator Networks, Volume 10, MDPI, Basel, 2021.

[2] Restas, A., UAV Application for Environmental Field Monitoring, Sensors, Volume 23, MDPI, Basel, 2023

[3] Al-Hourani, A., Kandeepan, S., Lardner, S., Optimal UAV deployment for cellular service in disaster areas, IEEE Transactions on Aerospace and Electronic Systems, Volume 52, IEEE, Piscataway, 2016, pp. 20-25.

[4] Lagkas, T., Argyriou, V., Bibi, S., Sarigiannidis, P., UAV-IoT for inspection and monitoring in the agri-food industry, IEEE Transactions on Industrial Informatics, Volume 17, IEEE, Piscataway, 2021.

AUTHOR INDEX